



University of HUDDERSFIELD

University of Huddersfield Repository

Peng, Bo

Mechanisms of Railway Wheel Polygonization

Original Citation

Peng, Bo (2020) Mechanisms of Railway Wheel Polygonization. Doctoral thesis, University of Huddersfield.

This version is available at <http://eprints.hud.ac.uk/id/eprint/35359/>

The University Repository is a digital collection of the research output of the University, available on Open Access. Copyright and Moral Rights for the items on this site are retained by the individual author and/or other copyright owners. Users may access full items free of charge; copies of full text items generally can be reproduced, displayed or performed and given to third parties in any format or medium for personal research or study, educational or not-for-profit purposes without prior permission or charge, provided:

- The authors, title and full bibliographic details is credited in any copy;
- A hyperlink and/or URL is included for the original metadata page; and
- The content is not changed in any way.

For more information, including our policy and submission procedure, please contact the Repository Team at: E.mailbox@hud.ac.uk.

<http://eprints.hud.ac.uk/>

Doctoral dissertation

Mechanisms of Railway Wheel Polygonization

Bo Peng

Supervisors: Simon Iwnicki

Philip Shackleton

A thesis submitted to the University of Huddersfield in partial fulfilment of
the requirements for the degree of Doctor of Philosophy

Institute of Railway Research
School of Computing and Engineering
University of Huddersfield

February 2020

Copyright Statement

- (1) The author of this thesis (including any appendices and/or schedules to this thesis) owns any copyright in it (the “Copyright”) and s/he has given The University of Huddersfield the right to use such Copyright for any administrative, promotional, educational, and/or teaching purposes.

- (2) Copies of this thesis, either in full or in extracts, may be made only in accordance with the regulations of the University Library. Details of these regulations may be obtained from the Librarian. Details of these regulations may be obtained from the Librarian. This page must form part of any such copies made.

- (3) The ownership of any patents, designs, trademarks and any and all other intellectual property rights except for the Copyright (the “Intellectual Property Rights”) and any reproductions of copyright works, for example graphs and tables (“Reproductions”), which may be described in this thesis, may not be owned by the author and may be owned by third parties. Such Intellectual Property Rights and Reproductions cannot and must not be made available for use without permission of the owner(s) of the relevant Intellectual Property Rights and/or Reproductions.

Acknowledgements

This doctoral dissertation is fully supported by CRRC Zhuzhou Locomotive Company, which is highly appreciated.

I wish to express my most sincere thanks to my main supervisor Prof. Simon Iwnicki. I learn a lot from him; not only the professional knowledge but also his impressing merits, such as efficient time management, enthusiasm for work, and good sociability. Although as a super-busy professor, he can always reply to my E-mail or questions incredibly fast. He is also good at providing encouragement, which is appreciated. Especially I would like to thank him for offering me with many opportunities, so that I can have experience in teaching in this university, become an experienced reviewer for journal papers, and expand my academic network based on his influence in the academic community.

The same respect is also given to my co-supervisor Dr. Philip Shackleton. He is very professional in railway vehicle dynamics, and can always provide me with constructive suggestions no matter how tough the question is. I thank him for the many times I have discussed complicated technical problems with him. He can always find the most critical issues in my papers. The expertise of this dissertation is guaranteed with his contribution.

Special thanks also to David Crosbee, who not only helped me with Simpack issues, but has also introduced British culture to me with beers in the pub. He is always my resort to solve Simpack problems. I will never forget the merits he showed me as a lovely British gentleman, as well as the jokes we had in the pub.

I must thank all other staff in the Institute of Railway Research (IRR) for their valuable help, as well as the technical discussions they have had with me. The thanks should also be given to Yunshi Zhao, Matin Sichani, Dimitrios Kostovasilis, and Joao Barbosa for their help and the wonderful time we spent together. Besides, I also enjoy the time staying with other PhD students in our group.

Thanks must be mentioned for Prof. Mats Berg and Associate Prof. Carlos Casanueva Perez in KTH who helped me clarify the applicability of the KTH wear model. I also need to thank other experts whom I met in the conferences, such as Prof. Sebastian Stichel, Prof. Jens Nielsen, Prof. Roger Lewis, Prof. Zili Li, Prof. Gang Sheng, Prof. Huangyun Dai, Prof. Wanming Zhai, and more. Ideas/thoughts from the conversations with these experts can inspire me to move further with my research, which is greatly acknowledged.

I also want to thank the chief expert Guosheng Chen in CRRC Zhuzhou Locomotive Company who provided me with much technical support and guidance, Dr. Gongquan Tao who shared some experimental data with me, Dr. Dabin Cui who had many beneficial discussions with me, and Dr. Yang Song who inspired me to derive some innovative findings.

I will miss the happy time with my friends in the UK. The hot pot followed by a movie or poker game every Friday evening is a typical relaxation for me with my cute friends Yang Song, Zhiwei Wang, and Ruichen Wang.

My final thanks belong to my family, as always. Their support is my ultimate power to proceed.

Published papers

Journal papers:

(1) **Bo Peng**, Simon Iwnicki, Philip Shackleton, David Crosbee. Comparison of wear models for simulation of railway wheel polygonization. **Wear**, 2019/10/15, v: 436-437.

Contributions: Bo planned and wrote the paper. Simon and Philip provided guidance and review. David helped with Simpack modelling issues.

(2) **Bo Peng**, Simon Iwnicki, Philip Shackleton, David Crosbee, Yunshi Zhao. The influence of wheelset flexibility on polygonal wear of locomotive wheels. **Wear**, 2019/08/15, v: 432-433.

Contributions: Bo planned and wrote the paper. Simon and Philip provided guidance and review. David and Yunshi helped with simulation issues.

(3) **Bo Peng**, Simon Iwnicki, Philip Shackleton, Yang Song. General conditions for railway wheel polygonal wear to evolve. **Vehicle System Dynamics**, 2019, 1-20

Contributions: Bo planned and wrote the paper. Simon and Philip provided guidance and review. Yang helped with programming issues.

Conference papers:

(1) **Bo Peng**, Simon Iwnicki, Philip Shackleton, Yunshi Zhao, Dabin Cui. A practical method for simulating the evolution of railway wheel polygonalization. The 25th international symposium on dynamics of vehicles on roads and tracks (**IAVSD 2017**). Rockhampton, Australia, 2017. p: 753-758. (Oral presentation)

Contributions: Bo planned and wrote the paper. Simon and Philip provided guidance and review. Yunshi and Dabin helped with simulation issues.

(2) **Bo Peng**, Simon Iwnicki, Philip Shackleton, David Crosbee, Yunshi Zhao. The influence of wheelset flexibility on the development of railway wheel polygonization. The 11th International conference on contact mechanics and wear of rail/wheel systems (**CM 2018**). Delft, Netherlands, 2018. p: 775-783. (Oral presentation)

Contributions: Bo planned and wrote the paper. Simon and Philip provided guidance and review. David and Yunshi helped with simulation issues.

(3) **Bo Peng**, Simon Iwnicki, Philip Shackleton. Comparison of wear models for prediction of railway wheel polygonalization. The 26th international symposium on dynamics of vehicles on roads and tracks (**IAVSD 2019**). Gothenburg, Sweden, 2019. (Oral presentation)

Contributions: Bo planned and wrote the paper. Simon and Philip provided guidance and review.

Notation

T_x	longitudinal tangential force [N]
T_y	lateral tangential force [N]
M	spin torque [Nm]
γ_x	global longitudinal creepage global [-]
γ_y	global lateral creepage [-]
ϕ	global spin [1/m]
τ	resultant tangential stress [N/m ²]
τ_x	longitudinal tangential stress [N/m ²]
τ_y	lateral tangential stress [N/m ²]
ξ	local resultant creepage [-]
ξ_x	local longitudinal creepage [-]
ξ_y	local lateral creepage [-]
$W_{(\text{wear model})}$	wear rate [depending on the wear model]
$K_{(\text{wear model})}$	original wear coefficient [depending on the wear model]
$K_{(\text{wear model})}^*$	global equivalent wear coefficient [m/N]
$K_{(\text{wear model})}^\#$	local equivalent wear coefficient [m ³ /N]
D	wheel diameter [m]
A	contact area [m ²]
\dot{E}	stochastic energy flow density [Nm/sm ²]
$H_{(\text{wear model})}$	global wear depth [m]
$h_{(\text{wear model})}$	local wear depth [m]
a	longitudinal semi-axis [m]
b	lateral semi-axis [m]
N	normal force [N]
d	sliding distance [m]
H	hardness of material [Pa]
p_z	normal pressure [N/m ²]
P_z	mean normal pressure [N/m ²]
Δd	local sliding distance [m]
μ	friction coefficient [-]
s	local resultant sliding velocity [m/s]
V	vehicle speed [m/s]
Δx	longitudinal length of one grid element [m]
m	number of longitudinal elements [-]
ρ	material density [kg/m ³]
v_x	global longitudinal sliding velocity [m/s]
v_y	global lateral sliding velocity [m/s]
ω	angular sliding velocity [rad/s]
dt	global passing time through one contact patch [s]
Δt	local passing time through one grid element [s]
O	wheel OOR order [-]
λ	wavelength of wheel OOR [m]
r	wheel radius [m]
C	wheel circumference [m]
k	amplification coefficient for polygonal wear [-]
pm	10 ⁻¹² m

Abstract

Railway wheel polygonization is manifest as uneven wear around the wheel circumference, which has been a severe problem worldwide for decades. It induces persistent periodic oscillation at the wheel-rail interface causing forced vibration to the vehicle/track dynamic system, which can seriously threaten the comfort and safety of the railway vehicles. Full understanding of its mechanisms is necessary for effective remedies to be proposed.

A Chinese electric locomotive suffering from severe wheel polygonization is employed as the research object. Abundant experimental data had been obtained by the CRRC Zhuzhou Locomotive Company through a long-term test campaign. With these measurement data, this dissertation aims to obtain general rules that the railway wheel polygonization will follow by simulation. The research is carried out in five fundamental aspects for railway wheel polygonization: the prediction program, the wear models, the effects, the influence of wheelset flexibility, and the influence of track flexibility. The main points of each aspect are described as follows.

(1) A common workflow for prediction of railway wheel polygonization is presented. Based on this workflow, some rules for the evolution of railway wheel polygonization are proposed providing innovative perspectives to understand the basic mechanisms of railway wheel polygonization. After summarising these rules, the general conditions for railway wheel polygonal wear to evolve are established. The phase between the instantaneous wear and the excitation is the key indicator determining the wheel OOR (Out-Of-Roundness) evolution direction (to grow or to diminish). The evolution tendency curve obtained from the instantaneous wear FRF (Frequency Response Function) is shown to be a useful tool for predicting the OOR evolution, especially for predicting the OOR order that would grow predominantly at a given operating speed.

(2) A comparative study on the applicability of existing popular wear models in simulation of railway wheel polygonization is carried out. Four representative wear models, developed by BRR (British Rail Research), KTH (Royal Institute of Technology), USFD (University of Sheffield), and Professor Zobory respectively, are selected for the comparison, with consideration of global and local methods. A uniform expression of the converted wear functions is derived analytically with the equivalent wear coefficient as a useful index to identify the proportional relationship between the wear models quantitatively. Simulation results show that all the wear models investigated present a similar ability to reflect the fluctuation of the instantaneous wear under various circumstances. Additionally, it is found that the global method is not suitable for calculating the polygonal wear of railway wheels.

(3) A tracking test for an electric locomotive suffering from serious wheel polygonization is introduced. Data is used to demonstrate the evolution of the polygonal wear of wheels and the vibration of the locomotive immediately before and after wheel re-profiling. A comparison is carried out between simulation results and measurement data. Based on the simulation model, parameter analysis is implemented to identify the effect of

wheel polygonization on the dynamic performance of the vehicle quantitatively. Some general principles regarding the effect of wheel polygonization on the vehicle are derived.

(4) The influence of wheelset flexibility on wheel polygonization is investigated. Results show that the wheelset flexibility cannot dominate the railway wheel polygonization in a general sense, unless some prerequisites are fulfilled to provide a suitable environment for the wheelset flexibility to be effectively and continually excited to fluctuate the contact responses. The torsional mode of the wheelset can be effectively excited by stick-slip vibration due to saturated contact adhesion that can occur on track with small curve radii or by large traction torque. If this situation persists for a long time, the development of the wheel polygonization can be expected. The excited order will be exactly determined by the wheelset torsional modal frequency and the vehicle speed.

(5) The influence of track flexibility on wheel polygonization is investigated. The sleeper passing frequency and the P2 frequency are considered as the two dominant frequencies coming from the track flexibility. Although the sleeper passing frequency is the most dominant frequency coming from the flexible track, it will not produce visible development of wheel OOR. The P2 resonance is an important factor contributing to the development of wheel OOR. The local rail bending modes are not found to influence the wheel OOR based on the Simpack FTR method.

Keywords: railway wheel polygonization; polygonal wear; effect; mechanisms; wear models; instantaneous wear; prediction program; evolution tendency curve; wheelset flexibility; track flexibility;

Contents

Copyright Statement	I
Acknowledgements	II
Published papers	III
Notation	IV
Abstract	V
Contents	VII
Chapter 1 Introduction	1
1.1 Background	1
1.2 Introduction to wheel wear and damage	2
1.2.1 Classification of wheel wear and damage.....	2
1.2.2 Introduction to wheel polygonization	3
1.3 Wear mechanisms in wheel/rail interface	4
1.4 Research scope of this dissertation	5
1.4.1 Aim	5
1.4.2 Objectives	6
Chapter 2 Literature review	7
2.1 The mechanisms of wheel OOR	7
2.1.1 Initial OOR due to wheel re-profiling.....	7
2.1.2 Resonant vibration of the vehicle/track dynamic system.....	8
2.1.3 Cast-iron tread brake block.....	11
2.1.4 Wheelset imbalance and material inhomogeneity	11
2.1.5 Wheel flat	11
2.1.6 Other research.....	11
2.2 The effects of wheel OOR	12
2.2.1 Measurement of the effects of wheel OOR.....	12
2.2.2 Simulation of the effects of wheel OOR.....	14
2.3 Numerical prediction of wheel polygonization	15
2.4 Research gap.....	16
Chapter 3 Prediction of railway wheel polygonization	18
3.1 Introduction	18
3.2 A common workflow for prediction of railway wheel polygonization	19
3.2.1 Assumptions for calculation of polygonal wear.....	19
3.2.2 Simulation scheme.....	19
3.2.3 Wear model.....	21
3.3 Some rules for the evolution of railway wheel polygonization	22
3.3.1 The basic rule for initial OOR to evolve.....	22

3.3.2	The effect of excitation on contact parameters	24
3.3.3	The evolution tendency curve	25
3.3.4	Convergency analysis on wheel revolutions	28
3.3.5	Linearity of excitation	30
3.3.6	Contribution of newly developed OOR.....	31
3.3.7	Contribution of track excitation	33
3.4	The general conditions for OOR to evolve.....	35
3.5	Discussions.....	35
3.5.1	Assumptions	35
3.5.2	Instantaneous wear FRF	36
3.5.3	Conditions for wheel OOR to develop	36
3.6	Summary	36
Chapter 4	Wear models for railway wheel polygonization.....	38
4.1	Introduction.....	38
4.2	Wear models.....	39
4.2.1	Assumptions	39
4.2.2	Definition of wear models	40
4.2.3	Conversion of Wear models	40
4.2.4	Uniform expression of converted wear models.....	45
4.3	Comparison of wear models.....	46
4.3.1	Under harmonic excitation	48
4.3.2	Under random excitation	51
4.3.3	Evolution of polygonal wear	54
4.4	Discussion	57
4.4.1	About the sharp points.....	57
4.4.2	About the assumptions	57
4.4.3	About the local Wear Index	57
4.5	Summary	58
Chapter 5	Effects of railway wheel polygonization.....	60
5.1	Introduction.....	60
5.2	OOR data analysis.....	60
5.3	Tracking test.....	64
5.3.1	Measurement scheme	64
5.3.2	Measurement results.....	66
5.4	Simulation of wheel OOR effects	69
5.4.1	Modelling of locomotive	69
5.4.2	Comparison between simulation and measurement	71
5.4.3	Effects of wheel OOR on curve negotiation.....	72
5.4.4	Parametric analysis of the effects of wheel OOR.....	75
5.5	Summary	80

Chapter 6 Influence of wheelset flexibility on railway wheel polygonization	81
6.1 Introduction	81
6.2 Modelling of the flexible wheelset	82
6.3 Frequency response analysis	83
6.3.1 Free wheelset	84
6.3.2 On-track wheelset	86
6.4 Influence of wheelset flexibility on contact responses	88
6.4.1 Straight track	88
6.4.2 Curved track with a small radius	89
6.5 Influence of wheelset flexibility on railway wheel polygonization	91
6.5.1 Prediction of the evolution of wheel polygonization	91
6.5.2 Case studies	92
6.6 Summary	96
Chapter 7 Influence of track flexibility on railway wheel polygonization	97
7.1 Introduction	97
7.2 Methods for modelling flexible track in Simpack	98
7.2.1 Direct and indirect methods	98
7.2.2 The FTR method	99
7.3 Modelling of flexible track based on the FTR method	100
7.3.1 Preparation of the flexible rail in FE	101
7.3.2 Configuration of the FTR file	103
7.3.3 Configuration of the MBS model	104
7.4 Comparison of tracks	104
7.5 Influence of track flexibility on polygonal wear	107
7.6 Summary	110
Chapter 8 Conclusions and future work	111
8.1 Conclusions	111
8.2 Main contributions of this dissertation	112
8.3 Future work	113
References.....	115

Chapter 1 Introduction

1.1 Background

Since 1825 when the first public railway in the world was operating in England, the railway, as the optimal means for massive transportation of passengers and cargos, has been an indispensable boost for the development of economy and society worldwide. This is especially the case for China, which has the largest population and the third-largest territory in the world. Chinese railway transportation has developed remarkably in recent decades to meet the needs of the country, resulting in the largest market of railways in the world, including high-speed lines, metro lines, and heavy freight lines. With the rapid advance of science and technology, the limit of railway transportation is being broken in terms of the maximum speed and the payload capacity. The operating speed of high-speed trains has exceeded 300 km/h in Germany, France, Japan, and China, and the traction tonnage has reached 20,000 tons or more in Australia, USA, South Africa, and China. However, challenges arise at the same time as the vehicle speed or axle load increases. One of the tough challenges is railway wheel polygonization, which has become a stubborn issue in railway engineering.

The phenomena of wheel polygonization have been widely found in all kinds of rolling stock for decades [1-7], including high-speed trains [3,8-12], metro trains [13,14], and locomotives [6,15], as shown in Figure 1-1. Especially in recent years, along with the ‘great-leap-forward’ development of railway in China, the problem of railway wheel polygonization has been a critical issue to be solved urgently for newly developed high-speed trains, locomotives and metro trains.

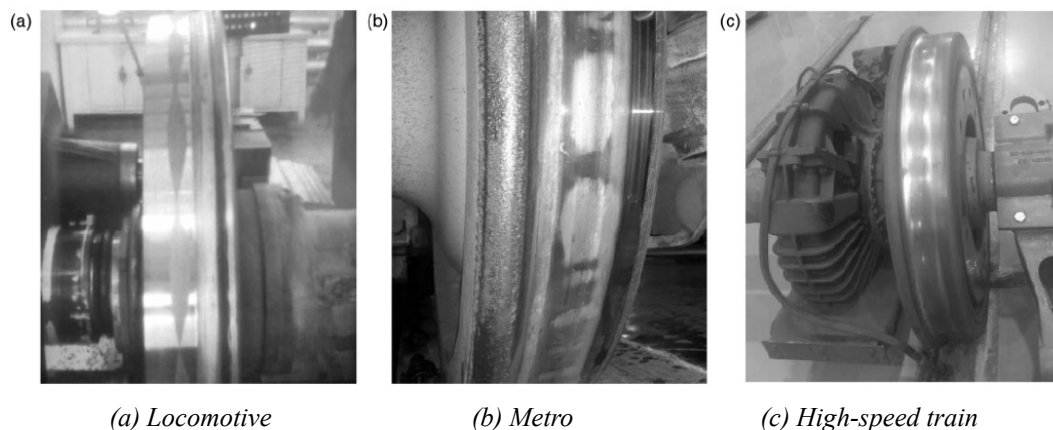


Figure 1-1 Images of railway wheel polygonization [6]

Railway wheel polygonization is manifest as uneven wear around the wheel circumference. When it is formed during vehicle running, it induces persistent periodic oscillation to the wheel-rail interface causing forced vibration to the vehicle/track dynamic system, which can seriously threaten the comfort and safety of the

railway vehicles, as well as the life cycle of the vehicle and the track [16]. The associated substantially higher maintenance costs necessary to manage OOR within acceptable levels have been the primary motivating factor for studies leading to a better understanding of the mechanisms of wheel polygonization and identifications of appropriate countermeasures to limit its growth [17]. Currently, the most common passive solution is either shortening the maintenance period for wheels, which can lead to a significant increase of maintenance costs, or changing the vehicle speed regularly, which clearly adds complexity to the operation management. To address these problems radically, the mechanisms of railway wheel polygonization have to be understood so that some effective solutions can be proposed.

1.2 Introduction to wheel wear and damage

1.2.1 Classification of wheel wear and damage

Nielsen [18] gave a broad definition of railway wheel Out-Of-Roundness (OOR) including any wheel defects, which has been widely accepted in the academic community [4,14,16,19,20]. To distinguish various terms of similar meaning more clearly, and to highlight the focus of current research, a classification of wheel wear and damage is presented in Figure 1-2.

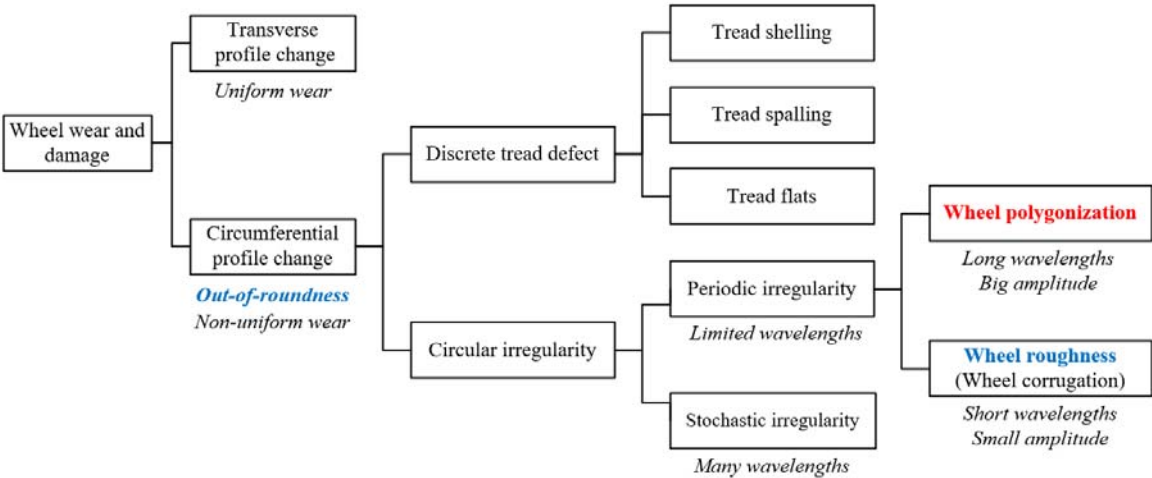


Figure 1-2 Classification of wheel wear and damage

Generally, wheel wear and damage lead to transverse wheel profile change, which is known as uniform wear [20] and circumferential wheel profile change, which is usually called Out-Of-Roundness (OOR) or non-uniform wear. The term uniform wear denotes deterioration mechanisms leading to a transverse wheel profile change, although constant around the wheel [20]. When speaking of a wheel profile change, it usually denotes the transverse wheel profile change. The circumferential profile change is mainly presented as circular irregularity of the wheel circumference, while it also covers discrete tread defects in Nielsen’s definition [18], including tread flats, tread spalling, tread shelling, and so on. The circular irregularity can be further divided into so-called periodic irregularity and stochastic irregularity, the distinction only depending on how many dominant wavelengths there are. If there are only a limited number of dominant wavelengths existing in the

circular irregularity, such as 1-4 orders in ICE high-speed trains [3], it is classified as periodic irregularity, otherwise as stochastic irregularity. Lastly, the periodic irregularity can be subdivided into wheel polygonization and wheel roughness. The distinction between the wheel polygonization and the wheel roughness is presented in Table 1-1. It should be noted that this is a rough division only aimed to differentiate these two terms.

Table 1-1 Distinction between wheel polygonization and wheel roughness

Term	Wavelength	Amplitude	Possible reason
Roughness	30-80 mm	10 μm	Tread braking
Polygonization	140 mm-one circle	>0.2 mm	Fixed-frequency mechanisms

As can be seen from Table 1-1, wheel roughness features relatively short wavelengths ranging from 30 mm to 80 mm and small amplitudes in the order of 10 μm , while wheel polygonization usually has longer wavelength varying from 140 mm to an entire circle and bigger amplitude above 0.2 mm (depending on specific situations). Under extreme circumstances, the amplitude of wheel polygonization can reach 1.4 mm [15]. In addition, wheel roughness is more often found on tread braked trains than on disc braked trains as the thermomechanical interaction between block and wheel tread can lead to hot-spotting which is not uniformly distributed over the wheel and brake block contact surfaces [19]. Comparatively, the wheel polygonization has been detected mainly on disc-braked wheels of, for example, high-speed trains [19] in Germany and electric locomotives in China [15]. The mechanisms of wheel polygonization and roughness could be very different from each other. It is generally believed that the wheel polygonization is caused by a system interaction issue with fixed-wavelength or fixed-frequency mechanisms [3,9,19,21].

The wheel polygonization highlighted with a bold red font in Figure 1-2 is the research focus in this dissertation. To avoid confusion, the terms of out-of-roundness (OOR) and wheel roughness, highlighted with a bold blue font in Figure 1-2, are both assumed to indicate the wheel polygonization as well in this dissertation, serving as alternative terms.

1.2.2 Introduction to wheel polygonization

Polygonal wheels present a periodic radial tread deviation from the mean wheel radius. The shape of the polygons can be approximated with a Fourier analysis of the measured radial tread deviation to determine the contributions of different harmonic orders. The corresponding wavelengths λ are defined by Equation (1-1):

$$\lambda = \frac{2\pi r}{O}, O = 1, 2, 3, \dots \quad (1-1)$$

where r is the wheel radius and O is the harmonic order. The case $O = 1$ indicates an eccentricity; the case $O = 2$ indicates a wheel ovality. The first three orders are illustrated in Figure 1-3.

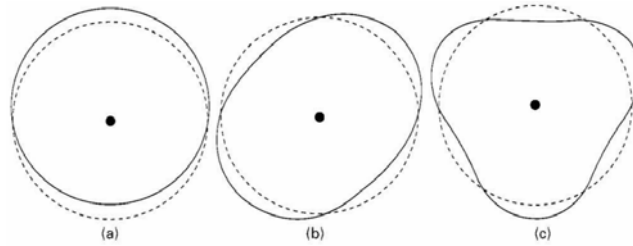


Figure 1-3 Examples of wheel polygonization in the order of 1(a), 2(b), 3(c) [19]

The wheel polygonization features a long wavelength and a big amplitude. Normally, several different polygonal orders exist simultaneously, but there is often one dominant order. Figure 1-4 shows a measured locomotive wheel OOR of dominant 18th order presented in the polar coordinate system, which is in a severe situation that can even be identified by the naked eye. A polygonal wheel leads to increased dynamic vertical wheel-rail contact force at specific excitation frequencies [19]. The excitation frequency f caused by the wheel OOR with a certain order O is determined by the train speed V and the wavelength λ according to Equation (1-2).

$$f = \frac{V}{\lambda} = \frac{V \cdot O}{2\pi r} \quad (1-2)$$

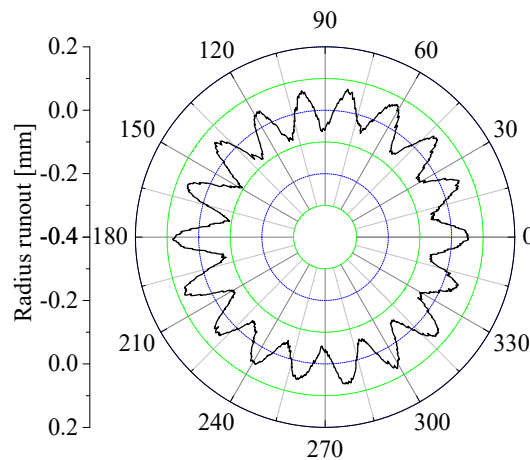


Figure 1-4 A measured wheel OOR of dominant 18th order [22]

1.3 Wear mechanisms in wheel/rail interface

Wear is the removal of material from a contacting surface, which may be in the form of debris. Various wear mechanisms could exist simultaneously in the wheel/rail surface. Some typical wear mechanisms are listed below [23]:

- Delamination wear: thin layers of material are formed and removed from the contacting surface.
- Oxidation or corrosive wear: removal of reaction products from chemical (or electrochemical) reactions between the contacting surface and the environment, e.g. rusting of rails.

- Adhesive wear: wear due to local bonding between contacting surfaces leading to material transfer or loss of material between/from the two surfaces. It can be seen as microscopic failure of asperities on the two bodies in contact.
- Abrasive wear: hard (microscopic) particles are forced against the contact surface and moved along it, e.g. wear of wheels and rails by sand in the contact patch.

Three wear regimes (mild wear, severe wear and catastrophic wear), which are characterized by wear rate and wear debris, have been identified based on previous experimental work (e.g. [24,25]). Lewis [24] carried out an elaborate research to investigate the wear rates and regimes of a railway wheel steel, as well as the wear mechanism evolution through the regimes when the severity of the contact conditions increases. Mild wear was featured by low wear rates and oxidative wear, while for the severe wear regime mild delamination of oxide layers was found as the cause of material loss. In the catastrophic regime, severe delamination and surface cracking can occur. The transition between mild and severe wear is due to the change from partial slip to full slip within the wheel-rail contact patch, whereas the transition between severe and catastrophic wear is caused by a temperature increase that leads to a decrease of the yield strength, resulting in more wear. According to the wear function developed by Lewis [24], the wear rate is proportional to the product of the creepage and the tractive force in the mild wear regime; for the severe wear regime the wear rate is stable regardless of this product; and in the catastrophic wear regime, the wear rate increases dramatically with this product.

Mild wear is more common on the wheel tread (and on the rail crown), while severe and catastrophic wear can occur during curve negotiation on both wheel tread and wheel flange. As a result, for prediction of wheel transverse profile, three wear regimes may have to be considered for specific scenarios. However, for prediction of wheel polygonization that typically exists on the wheel tread, mild wear might be the main wear mechanism of initiation.

1.4 Research scope of this dissertation

Railway wheel polygonization is related to not only the material wear itself but also the complicated interaction between the vehicle and the track. Both experiment and simulation are carried out to investigate this tough issue in this dissertation. An experimental campaign for some Chinese electric locomotives suffered from wheel polygonization was carried out by CRRC Zhuzhou Locomotive Company and Southwest Jiaotong University cooperatively since 2013. Abundant test data in terms of the circumferential shape of the polygonal wheels and the vibration responses of the vehicle had been obtained as the basis of this dissertation.

1.4.1 Aim

This dissertation aims to improve the understanding of the initiation mechanisms of railway wheel polygonization through fundamental research, by ascertaining the general rules that railway wheel polygonization will follow.

1.4.2 Objectives

In Chapter 2, a literature review is first carried out to summarize the state-of-the-art of current understandings regarding the mechanisms and effects of wheel polygonization, based on which the research gap is concluded.

In Chapter 3, a prediction program for the evolution of railway wheel polygonization is developed. Some rules for the evolution of railway wheel polygonization are proposed providing innovative perspectives to understand the basic mechanisms of railway wheel polygonization. After summarising these rules, the general conditions for railway wheel polygonal wear to evolve are established.

In Chapter 4, the applicability of existing popular wear models in simulation of railway wheel polygonization is analyzed. Four representative wear models, developed by BRR (British Rail Research), KTH (Royal Institute of Technology), USFD (University of Sheffield), and Professor Zobory respectively, are selected for a comparative study, with consideration of global and local methods.

In Chapter 5, a tracking test for an electric locomotive suffering from serious wheel polygonization is introduced. Data is used to demonstrate the evolution of the polygonal wear of wheels and the vibration of the locomotive immediately before and after wheel re-profiling. Some general principles regarding the effect of wheel polygonization on the vehicle are derived based on parameter analysis.

In Chapter 6, the influence of wheelset flexibility on wheel polygonization is investigated. After analyzing the FRF (Frequency Response Function) of the contact responses against the track irregularity for a free wheelset and an on-track wheelset, the influence of wheelset flexibility on the contact responses and the evolution of wheel polygonization is simulated for various scenarios.

In Chapter 7, the influence of track flexibility on wheel polygonization is investigated. The vehicle/flexible track MBS (Multi-Body System) model is built based on the Simpack FTR (FlexTrack Reference) method. Simulation is carried out to check how the track flexibility influence the polygonal wear of wheels, and whether the local rail bending modes can be excited to dominate the wheel polygonization.

Chapter 2 Literature review

Nielsen and Johansson [18,21] reported the state-of-the-art in research of railway wheel polygonization up to 2003, regarding the classification, root causes, consequences, and some remedies. Another review by Barke [16] in 2005 compared previous studies that used analytical and numerical models to illustrate the distribution of wheel OOR impact on track and rolling stock components. These reviews offered an overall picture of railway wheel polygonization in terms of the features, causes, impact loads, removal criteria, and solutions. However, in the recent 10 years, a lot of research has proceeded to enhance the understanding of railway wheel polygonization, with significant contributions coming from the Chinese academic community along with the ‘great-leap-forward’ development of railway in China.

This literature review is attempted to summarize the understandings of railway wheel polygonization up to date. The research on railway wheel polygonization involves two aspects: the effects and the mechanisms. The former is to identify the root cause of the wheel polygonization so that some active countermeasures can be proposed to limit or eliminate the growth of wheel OOR. The latter is to recognize the negative influence of polygonal wheels on the vehicle/track dynamic system in order to develop some maintenance strategies for the wheels, including monitoring and wheel re-profiling. These two aspects will be reviewed separately. In addition, the numerical prediction for railway wheel polygonization is briefly introduced. After summarizing the literature review, the research gap is concluded and the research scope of this dissertation is defined.

2.1 The mechanisms of wheel OOR

The investigation of wheel OOR mechanisms is a complicated issue, as several causes might exist simultaneously. In this section, the literature review is grouped by the potential causes proposed by previous researchers.

2.1.1 Initial OOR due to wheel re-profiling

Rode [26] investigated defects in wheels of the inter-city express (ICE) trains in Germany, and concluded that the fixed-clamping used in the wheel re-profiling process could result in initial OOR of the third-order.

Cui [27] investigated the effect of turning characteristics of underfloor wheel lathes on the evolution of wheel polygonization. The results showed that the higher-order polygon on the wheel surface could be effectively removed by two cuts. The eccentricity and phase angle of the friction rollers had no influence on the cutting quality of higher-order polygons, whereas they were the primary cause for the fourth-order polygons. The severity of the fourth-order polygon depended on the level and the phase of the eccentricity of the friction rollers. The space of the two rollers could also significantly affect the cutting quality.

2.1.2 Resonant vibration of the vehicle/track dynamic system

Most research stand in the perspective that the railway wheel polygonization must be a ‘fixed-frequency’ or ‘fixed-wavelength’ issue, and the root-cause must be some resonant vibration existing in the vehicle/track dynamic system. However, as for which kind of resonant vibration can cause the wheel polygonization, different explanation can be found in the literature, as grouped in the following.

2.1.2.1 Wheelset flexibility

Morys [3] investigated the origin and enlargement mechanism of wheel OOR of ICE carriages in Adams considering the flexibility of wheelset and track, a simple bogie and carbody. It indicated that the large normal force variations could accelerate the wheel vertically and excite a bending oscillation of the wheelset axle, which leads to lateral slip and lateral material excavation. It was also concluded that in the presence of specific operating conditions, only some OOR orders (order 3 in this case) enlarged rapidly, whereas others change their shape and led to higher OOR orders.

Meywerk [9] developed a flexible wheelset model running on flexible rails to demonstrate the growth of wheel OOR profiles. The results showed that the first two bending modes of the wheelset played an essential role in the growth of polygonal wheels; asymmetric OOR wheels of one wheelset were worn quicker than symmetric ones; the eigenvalues could indicate the harmonics that would grow faster than others. It was also emphasized that other reasons for wheel polygonization might exist too, e.g. excitations due to resonance of unsprung masses.

Jin [5] investigated the mechanism of the polygonal wear of a Chinese metro train by carrying out model tests of a vehicle and its parts and the tracks, the dynamic behaviour test of the vehicle in operation, and the observation test of the polygonal wear development of the wheels. The testing results indicated that the root cause was the first bending resonance of the wheelset.

Similarly, another investigation carried out in China for metro trains was done by Liu [28]. The main conclusion was that the coupling of the movement of the bending mode of the wheelset and bounce motion of the linear motor is the leading cause of the formation of polygon-shaped wheels on a metro train, which could be solved by changing the structural parameters of the wheelset.

Tao [29,30] investigated the mechanism of the polygonal wear of electric locomotive wheels through experiments conducted at field sites. The experimental results indicated that the first bending resonance of the wheelset was the root cause for the wheel polygonization of the 18th order. In addition, the second bending mode of the wheelset was suspected to drive the 24th order of wheel polygonization, which however has not been verified.

Periodic out-of-round or polygonal wheels were detected on a fleet of high adhesion locomotives operating within South Africa. The polygonal wheels increased the vertical load spectrum of the locomotive resulting in

accelerated component failures. The torsional vibration of the locomotive axle was confirmed theoretically and experimentally through various physics models and on-track measurements. Based on the results, two potential torsional vibration excitation mechanisms were identified, namely self-excited stick-slip vibration under saturated adhesion and forced excitation by the harmonics and inter-harmonics from a VFD (Variable Frequency Drive) driven AC traction motor. A proposed countermeasure that uses the control system to detect and arrest the vibration showed a reduction in torsional vibration severity. [31]

2.1.2.2 P2 resonance

Johansson [14] developed a prediction tool for wheel polygonization to determine the mechanism that explains the continued growth of the third-order wheel polygonization on wheels in the Stockholm subway. It was concluded that the main mechanisms of wheel OOR are the vertical track anti-resonance around 165 Hz and the P2 resonance. Increasing the train speed will shift the dominating wheel irregularity orders to lower ones (longer wavelengths) due to the ‘frequency-constant’ mechanism. Some differences in the results were observed for the leading and trailing wheelsets of the bogie because of the unequal phases of the initial OOR on the leading and trailing wheelsets with respect to the track configuration. [14]

Johansson [14] also stated that “The effect of wheel wear due to the dynamic wheel-rail interaction was considered to be the only active damage mechanism. In reality, there might be other simultaneous effects influencing the wheel OOR, such as plastic deformations, tread braking, traction control, and material inhomogeneity around the wheel circumference. Consequently, the presented numerical simulations do not explain the formation of the high degree of low harmonic order dominating OOR detected in the Stockholm subway.” In addition, the increase of the initial third order OOR during rolling may be caused by the braking or traction system rather than wear.

Tao [32] investigated the mechanism of polygonal wear of a metro train by site measurements and wheelset modal test. The investigation results indicated that the fixed-frequency mechanism of the wheel OOR with 5–8 harmonics was the P2 resonance. Four interesting interventions were proposed to mitigate the formation of polygonal wheel wear based on the field measurement results.

Cai [33] carried out an experimental and numerical investigation into the formation of wheel polygonization of a metro vehicle. It was suggested that the P2 resonance, which was the main contributor to the high amplitude of wheel/rail contact forces in the 50-70 Hz frequency range, was the cause for the polygonal wear. Parametric studies showed that the dominant order decreases as vehicle speeds increase, representing a frequency-constant mechanism. The wheelset flexibility, especially the bending mode, would aggravate the wheel/rail creepage and further accelerate the formation of polygonal wear. Higher rail pad stiffness would increase P2 resonance frequency and shift the dominant polygonal orders to higher ones.

2.1.2.3 Rail flexibility

Li [34] stated that the wheel polygonization might be attributed to the bending mode of rails as the frequency

of the third vertical bending mode of the local rail section between adjacent wheelsets coincides with the passing frequency of the polygonal wheels. In addition, it has been found that the vibration induced by polygonal wheelset could be transmitted to a neighboring non-polygon wear wheelset through the track.

Wu [35] carried out a study on the formation of high-order wheel polygonization for a high-speed train. The local rail bending modes were suspected as the root cause. Specifically, the bending vibration mode of the rail segment between two wheelsets, regarded as three half-wavelength bending vibration mode near 650 Hz, was identified as the primary contributor to high magnitude wheel/rail contact force in the 500–800 Hz frequency range. Simulation also indicated that the wheelset flexibility and higher rail pad stiffness accelerated the wheel wear and were more likely to contribute to the lower order wheel polygonalization. Increasing the rail pad damping could effectively reduce the rate of growth of high order wheel polygonalization.

2.1.2.4 Self-excited vibration

Chen and Zhao [36,37] proposed that the frictional self-excited vibration of a wheelset-track system caused by the saturated wheel-rail creep force was a possible mechanism for wheel polygonal wear of high-speed trains. The results showed that when wheels slip on rails in the braking process of trains, the friction-induced self-excited vibration of the wheelset-track system can quickly occur, which may induce the wheel polygonization. It was proposed that preventing the wheel from slipping on the rail was an essential precaution to suppress polygonization of wheel treads, and increasing the damping of the rail fastener was helpful to suppress the wheel polygonization.

2.1.2.5 Stick/slip vibration

Xu [38] studied the longitudinal vibration of wheel-rail contact and its implications for wheel OOR. It was stated that the longitudinal wheel vibration always exists when the traction or braking torque of the wheelset changes instantaneously and the primary frequency of longitudinal vibration is the contact patch's frequency. If the wheelset were subject to constant torque under an insufficient adhesive coefficient condition, a dramatic longitudinal stick/slip vibration would occur. The fixed excitation frequency could cause a periodic impact to wheels, resulting in the periodic wear around the wheel rim. This probably generated a particular order polygonization.

2.1.2.6 Bogie resonance

Wu [7] investigated the mechanism of high-order polygonal wear of a high-speed train through extensive field experiments. The investigation included the measurement of wheel OOR, vibration, and dynamic behaviour of train and track and numerical modal analysis of vehicle components. It indicated that the formation and development of high-order wheel polygonal wear was initiated by the excited resonance of the bogie of the train in high-speed operation. Moreover, the investigation showed that changing the running speed of the train could effectively mitigate the high-order wheel polygonal wear.

2.1.3 Cast-iron tread brake block

A study of wheel wear in intercity trains in the Netherlands suggested that interactions of the wheel with the cast-iron brake block could lead to a wheel polygonization phenomenon, characterized by a combination of the low order harmonic wear and short-pitch irregularities over the wheel circumference. It suggested that the cast-iron block brakes must be either optimized or removed to reduce the roughness level. The thermo-elastic instability of the wheel material and the material transfer during braking were reported as the primary causal factors leading to wheel OOR. The study also suggested that vehicles equipped with cast iron tread brake blocks were more likely to incur wheel polygonization compared to the wheels with disc brakes. [39]

2.1.4 Wheelset imbalance and material inhomogeneity

Meike [10] used a rotational wheelset model with 40-DOF to investigate the wheel polygonization caused by an imbalance of wheels. The model showed that the dynamic unbalance and inhomogeneity in the wheel material might also contribute to lower-order harmonics of the continuous or periodic circumferential defects. Morys [40] reported that the wheelset dynamic imbalance caused big oscillation of the wheels and small vibration of the brake disks for ICE high-speed trains, while the opposite conditions hold for static imbalances.

2.1.5 Wheel flat

Ye [41] provided an innovative hypothesis stating that wheel flats can cause or exacerbate wheel polygonization. The simulation results showed that vehicle speeds and flat lengths had a considerable influence on the polygonal wear. A field test of a Y25-tank-wagon was also conducted to verify this hypothesis. It further stated that those excitations or defects, which can cause long-term periodic wheel-rail impacts, might result in or aggravate wheel polygonization.

2.1.6 Other research

The Vancouver mass transit system in Canada has experienced severe rail and wheel corrugation problems. The development of corrugations was deemed to be due to poor alignment of wheelsets in bogies, generation of 'roll-slip' oscillations between wheel and rail, and the development of close conformity between the wheel tread and the rail. Some remedies were proposed, including reducing the tolerance of wheelset misalignment to ± 10 minutes of arc, applying a friction modifier to wheels to change the friction characteristic between the wheel tread and rail from negative to positive, re-gauging the track and grinding the rail to different profiles in each of the four equal sections of tangent track. These remedies have virtually eliminated corrugation from the system. [42]

Brommundt [12] applied a simple wheelset model (2 degrees) and developed a perturbation procedure to investigate the growing non-circularity of railway wheels. The study indicated that the developments in wheel OOR was attributed to gradual wear caused by the wheel/rail interactions. It was concluded that the increase of vehicle speed contributes to deformations dominated by the lower order harmonics.

Ma [43] proposed an idea that a polygonal wheel could be formed by vibrations acting during several revolutions of a wheel rather than just one revolution, so that low-frequency wheel vibrations and forces might also contribute to the generation of the polygonal wheel.

Zhou [44] investigated the relationship between the wheel polygonization formation mechanism and the structure of a high-speed EMU bogie. It was found that different primary suspensions and positioning structures of the bogie would have a different influence on the fixed wheelbase of the bogie. When the rolling-arm axle-box positioning structure is adopted, the wheel can move slightly and regularly in the longitudinal direction due to the up and down motions of the primary spring, thus resulting in the wheel polygonization.

Pan [45] focused on the micro-mechanism of polygonal wear of railway wheels. His study revealed that during rolling, the non-uniform force on the contact surface, arising from radial vibration from the axle, led to non-uniform plastic deformation of the outermost layer. In the regions of higher plastic deformation, cracks tended to form and expand along with the fibrous structure, and micro-spall pits deepened and became interconnected. Wave crests and troughs then formed on the surface.

2.2 The effects of wheel OOR

Wheel OOR brings about extra cyclic impact load at the rail/wheel interface every time the wheel rotates, which can have detrimental influences on track and vehicle components, contributing to increased rolling noise, risks of rail breaks, sleeper cracking, fatigue of wheels and axles, component damages, and so on [18]. The severity of wheel OOR must be kept within an acceptable limit to ensure the safety of the railway vehicles and the comfort of passengers. To make a rational decision about removing polygonal wheels from service, much research has been undertaken by field measurement or simulation.

2.2.1 Measurement of the effects of wheel OOR

The measurement of the effect of wheel OOR commonly involves the inspection of the circumferential wheel shape and the detection of vehicle/track vibration in the presence of wheel OOR. Many measurement campaigns have been carried out worldwide, covering high-speed trains, locomotives, and metro trains. Some typical test campaigns found in the literature are briefly described below.

A research program was carried out to survey the range of typical roughness appearing on the wheels of Dutch railway rolling stock and the rails of the Dutch network [39]. Over 140 wheels were selected. This survey was made to obtain a picture of the absolute roughness levels and their contribution to radiated rolling noise in order to decide how to reduce railway rolling noise.

To obtain a representative indication of OOR existing in the traffic in Sweden, an extensive measurement campaign was launched in 2002 by measuring OOR, transverse profile and surface hardness of 99 wheels on passenger trains (X2 and intercity), freight trains, commuter trains (Regina) and underground trains (C20) [13]. Both tread and disc braked wheels were measured. The only requirement used in the selection process was the

minimum travelled distance of 100,000 km.

Wu [46] reported a long-term field test programme for a Chinese high-speed train with polygonal wear. The field measurements involved monitoring of wheel profiles between successive re-profiling of the wheels to obtain the growth rate of polygonal wear in addition to the axle box acceleration. The data suggested rapid development in wheel OOR, which was characterized by polygonal wear of the 18th and 19th harmonic orders. The axle box acceleration was suggested to serve as a useful indicator for detecting wheel polygonization and thereby the criterion for wheel removal.

Shi [47] reported a two-year experiment conducted to record the wheel profiles and structural vibrations of high-speed trains. The experiments showed that the dominant wear concentrated on the nominal rolling radius, and the wear rate could increase with operating distance due to the surface softening resulting from the loss of wheel material. The increase of the equivalent conicity of the wheelset, which rises approximately linearly with the wheel wear and operating distance, could aggravate the vibration of structural components. High-frequency vibrations arising in the bogie and car body were related to the track arrangement and wheel OOR, which could cause the ride comfort to worsen significantly.

Tao [30] reported a comprehensive measurement campaign for several Chinese electric freight locomotives suffering from serious wheel OOR. This project was undertaken by CRRC Zhuzhou locomotive company in cooperation with Southwest Jiaotong University. The experimental data used in this dissertation came from this test campaign. More than 2000 wheels of seven types of locomotives widely used in China have been measured since April 2013. The typical wheel polygonization features are shown in Figure 2-1.

As can be seen from Figure 2-1, three typical polygonal wheels with 18, 19, and 24 waves were found. The figure legends indicate the measurement position from the wheel's flange side. Figure 2-1(a) shows the amplitude of the polygonal wear described in the polar coordinate system. The left, middle, and right images in the figure demonstrate the rolling circle irregularity of the worn wheels presenting 18, 19, and 24 waves, respectively. Interestingly, the waveforms of the polygonal wear are very regular. The interval of each wave is also almost similar. The different wheel tread positions present the same wear pattern. However, the irregularity depth may differ, as shown in the left and middle images of Figure 2-1(a). The polygonal wear of the left and right wheels of the same wheelset is almost the same in the polygonal order and phase. Figure 2-1(c) shows the 1/3 octave band spectrum results of the three typical polygonal wear wheels. The wheels with the 18th or 19th order OOR represent 200 mm wavelength in the 1/3 octave bands, and that of the 24th order OOR is 160 mm. [30]

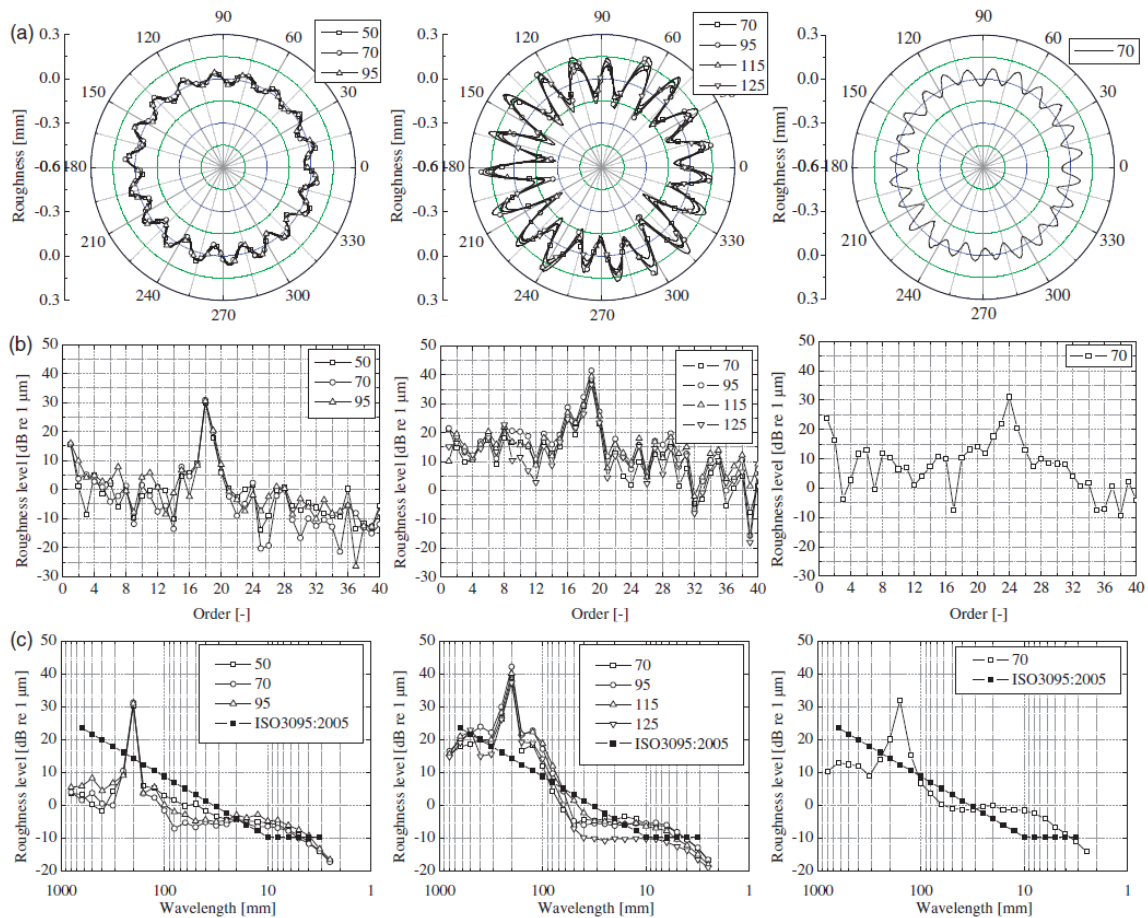


Figure 2-1 Typical polygonal wear of wheels with 18, 19, and 24 waves (from left to right). (a) Described in the polar coordinate system. (b) order levels. (c) 1/3 octave band spectrum of the measured irregularities. [30]

2.2.2 Simulation of the effects of wheel OOR

As an alternative to measurement, simulation is a convenient way to identify the effects of wheel OOR. The task for this area is to quantify the effects of wheel OOR on the vehicle/track dynamic system, based on parametric analysis in the simulation. Some commercial software has already provided the functionality of modelling polygonal wheel (e.g. Simpack [48]), so that the responses of the vehicle/track dynamic system in the presence of wheel polygonization can be easily simulated.

Xiao [49] carried out research on the influence of harmonic wheel wear on wheel-rail contact geometry of a high-speed train using Universal Mechanism (UM) software. The results showed that the harmonic order and the wave depth had a small influence on the wheelset lateral displacement and therefore the contact geometry. The wave depth was more influential than the order.

Wu [50] examined the effect of wheel polygonization on the fatigue of the wheelset-mounted gearbox housing of a high-speed train. The comparative analysis showed that the fatigue damage with a 20th order polygonal wear was 63% larger than that without the polygonal wear on the wheel.

Wang [51-53] investigated the effect of wheel OOR on the torsional vibration of the gear transmission system, the dynamic forces within the axle-box bearing, and the gearbox housing for a high-speed train, respectively. The general conclusion was that the wheel OOR could significantly influence the transmission system, including the axle-box bearing and the gearbox housing. If resonance of the component (e.g. the gearbox housing) was induced by the wheel OOR, damage could occur.

Lan [54] investigated the wear damage of wheel OOR in rail wagons under braking. This work showed that the OOR defect could dominate the normal contact force with a dynamic impact force factor of 1.48. It was suggested that the ratio of load reduction was a better indicator determining the derailment risk than the Nadal's derailment quotient in the presence of wheel OOR.

Chen [55] focused on the effect of wheel polygonal wear on high-speed vehicle-track subgrade vertical interactions. The results showed that the increased polygon order and wave depth could exacerbate the wheel-rail vertical forces, wheel unloading rates, fastener forces, and rail accelerations significantly. The lower orders of wheel polygonization mainly affected the vertical displacement and stress of the subgrade system.

Wu [17] analyzed the dynamic responses of a high-speed vehicle due to wheel OOR, as well as the influence of polygonal wear on the wheelset axle stress [56]. The results showed that high-order wheel polygonization could lead to high-frequency impact loads at the wheel/rail interface, by which some vibration modes of the wheelset and the axle box could be excited leading to high-magnitude axle box acceleration and dynamic stress in the wheelset axle.

Liu [57] investigated the vertical dynamic wheel/rail interaction resulting from a polygonal wheel at high-speeds using a vertical vehicle-track coupled dynamics model. The results showed that the dynamic wheel-rail load became more sensitive to high order harmonics with increased vehicle speeds.

Zhang [58] presented a detailed investigation conducted into the relationships between wheel polygonal wear and wheel/rail noise, and the interior noise of high-speed trains through extensive experiments and numerical simulations.

2.3 Numerical prediction of wheel polygonization

Almost all the numerical models for prediction of railway wheel polygonization followed an iterative loop program structure consisting of two main models: MBS model and wear model. A typical example of prediction program for railway wheel polygonization was given in Figure 2-2, which was developed by Johansson [14]. As can be seen, an initial OOR can be assigned as the initial state of the wheels. The MBS model is responsible for calculating the wheel/rail contact responses in the presence of wheel polygonization (initial OOR or iterative OOR). The polygonal wear is then calculated with a wear model using the contact responses as the inputs. Here the polygonal wear means the material loss against circumferential location. After an iteration, the circumferential shape of the wheels is updated by the polygonal wear. After many iterations, the long-term

evolution of the wheel polygonization is monitored. The model parameters, such as speed and track properties, could be different from one iteration to another so as to adapt the realistic operation scenarios.

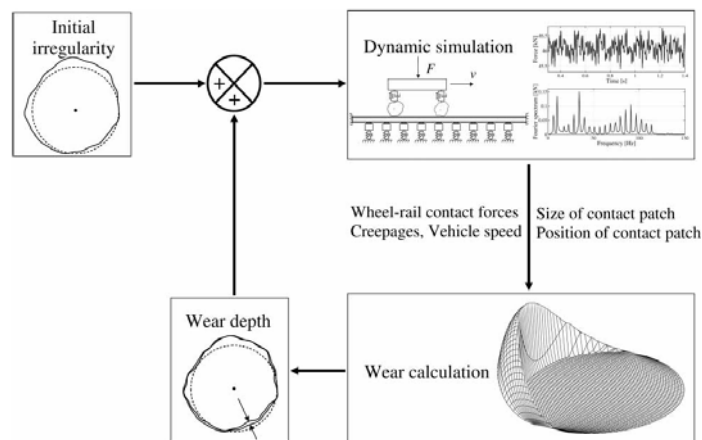


Figure 2-2 Illustration of iteration scheme for coupling of simulations of dynamic train-track interaction with calculations of wear[14]

2.4 Research gap

Currently, the understanding of the negative effect of railway wheel polygonization has been well established through experiments and simulation. The characteristic impact of wheel OOR is that it leads to persistent periodic forced vertical oscillation at the wheel-rail interface with fixed frequencies according to the dominant wavelengths of wheel OOR and the vehicle speed. This periodic forced vibration occurring at the stiff contact between the wheel tread and the railhead is transmitted to the whole vehicle/track dynamic system, introducing risks of component resonances and potential damages. Most research in this area has been to quantify the effect of wheel OOR on different parts of the vehicle/track dynamic system, based on which, the acceptable limit of wheel OOR can be recommended. This dissertation will conclude some general principles for the effect of wheel OOR on the vehicle.

On the contrary, for the mechanisms of wheel OOR evolution, the situation is relatively complicated. Researchers are continuing efforts to investigate the root causes of railway wheel polygonization from varied perspectives. Some potential influencing factors have been revealed, such as vehicle speed, P2 resonance [14,32], wheelset flexibility [3,9,28,29,31,59], local rail flexibility [35], wheelset imbalance [10], material hardness [60], self-induced vibration [36], wheel flats [41], AC motor [61], and so on. However, there has not been a universal explanation that can cover all circumstances, possibly because the railway wheel polygonization is a multi-factor problem, and for different scenarios (e.g. vehicle type, track type, speed range) the wheel polygonization may be attributed to different combinations of those potential factors, which makes the problem hard to explain.

To investigate the mechanisms of railway wheel polygonization, a prediction program is necessary. However, no existing commercial available software can fulfil this task on its own. It can only be realized either by

secondary development based on existing MBS (Multi-Body System) software or with self-developed MBS packages. No matter what the solution is, the prediction of non-uniform wheel circumferential wear (wheel OOR) is to date far less mature, compared to the wheel transverse wear prediction that has been used successfully in commercial applications. Railway wheel polygonization is related to not only the material wear itself, but also the complicated interaction between the vehicle and the track. Multiple factors, as discussed above, can contribute to the initiation of wheel OOR simultaneously, which makes this problem difficult to interpret. As a result, it is imperative to carry out fundamental research establishing the general rules that the wheel polygonization will follow.

The general rules of wheel polygonization are directly based on the prediction program itself. In other words, the prediction program for wheel OOR evolution must be logical and be able to reflect reality with sufficient accuracy. However, many fundamental issues have not been understood clearly in terms of the prediction program for wheel OOR. For example, which type of wear model is suitable for calculating polygonal wear? What kind of workflow should the prediction program adopt? What simplifications are acceptable and which are not? What is the reasonable logic that the prediction program should comply with? What are the conditions for polygonal wear to evolve? These questions will be discussed thoroughly in this dissertation.

In addition, among all the components of vehicle/track dynamic system, the wheelset [3,9,28,29,31,59] and the track [35] could be the most important components that could influence the initiation of wheel OOR, as they are the nearest components to the wheel-rail contact interface where the polygonal wear occurs. Specifically, the flexibility of the wheelset and/or track might be excited to cause periodic circumferential wear around the wheel tread. However, it is still controversial in this area that deserves more investigation. This dissertation will also dig into the influence of wheelset flexibility and track flexibility on wheel polygonization.

Chapter 3 Prediction of railway wheel polygonization

3.1 Introduction

To ensure the safety and comfort of railway rolling stock, the most common passive solution is either shortening the maintenance period for wheels, which can lead to a significant increase of maintenance costs, or changing the vehicle speed regularly, which clearly adds complexity to the operation management. To address the root cause of this problem radically, its mechanism has to be understood so that some direct and effective solutions can be proposed.

Currently, it appears that railway wheel polygonization must be a fixed-frequency issue. Specifically, there must be some structural modes of the vehicle/track dynamic system that can be excited to initiate the wheel polygonization with particular orders at particular speeds. Based on this view, researchers are continuing efforts to find the structural mode frequency that can match the dominant vibration frequency of wheels in the presence of wheel OOR, either by measurement or simulation. Some potential influencing factors have been revealed, such as vehicle speed, P2 resonance [14,32], wheelset flexibility [3,9,28,29,31,59], local rail flexibility [35], wheelset imbalance [10], material hardness [60], self-induced vibration [36], wheel flat [41], AC motor [61], and so on. However, there has not been a universal explanation that can cover all circumstances, possibly because the railway wheel polygonization is a multi-factor problem, and for different scenarios (e.g. vehicle type, track type, speed range) the wheel polygonization may be attributed to different combination of those potential factors, which makes the problem hard to explain. Consequently, it is necessary to carry out research on the fundamental evolution rules for railway wheel polygonization. As it is not easy to implement this kind of fundamental investigation through experiment due to the high testing cost and serious influence on the normal operation, simulation becomes the best alternative, but the reasonability and robustness of the prediction program need to be guaranteed.

Compared to the wheel transverse wear prediction that has been successfully applied in businesses, the prediction of railway wheel polygonization is far less mature up to now. As the characteristics of the circumferential wheel wear are substantially different from those of the transverse wheel wear, the simulation method cannot be just copied from one to another, and some adaptations have to be made, although both of them follow an iterative loop program structure. Few researchers have elaborated on the prediction program of railway wheel polygonization on itself in a comprehensive sense. Johansson [14], Morys [3], and Meinke [10] are some pioneering researchers who introduced the iterative loop program structure to the prediction of railway wheel polygonization. Fu [62] discussed some details of the numerical simulation for polygonal wear, such as simulation steps, continuity of polygonal wear, and profile updating conditions. To understand the complex phenomena of railway wheel polygonization better, the prediction program has to be logical and consistent to obtain results that can reflect the reality.

This chapter is carrying out fundamental research to investigate the general conditions for railway wheel polygonal wear to evolve. A common workflow for predicting the railway wheel polygonization is firstly introduced, including some assumptions for calculation of polygonal wear, the simulation scheme, and the wear models. Based on this workflow, several rules for the evolution of railway wheel polygonization are proposed providing innovative perspectives to understand the underlying mechanisms. By summarizing these rules, the general conditions for railway wheel OOR to evolve are established.

3.2 A common workflow for prediction of railway wheel polygonization

3.2.1 Assumptions for calculation of polygonal wear

The most realistic simulation of the wheel tread wear is in 3D and a real-time sense, which means that the 3D geometry of the wheel tread should change for every wheel revolution. However, this is either technically impossible or unbearably time-consuming with today's technology. As a result, similar to the simulation of railway wheel transverse profile wear, some assumptions have to be made to allow the simulation of the wheel circumferential wear to be feasible, which are listed below:

- The wheel transverse profile is assumed not to change, with the focus only on the change in the wheel circumferential profile. This assumption is justified by the fact that, when railway wheel polygonization occurs, the circumferential shapes measured at different wheel lateral positions are quite similar [13,30].
- The instantaneous wear is assumed to be equally distributed across the transverse section, which is implicit from the first assumption. For each contact patch in time sequence, an averaged wear depth is calculated.
- The wear is assumed to occur only in the sliding zone of the contact patch, without consideration of the plastic deformation. A typical combination of the contact model is Hertz & FASTSIM, while other types of contact model could also be applied.
- The nominal wheel radius can be assumed not to change or to reduce with wear. If the radius is reducing during the iteration, the simulation workflow will be more complicated. In this thesis, the nominal wheel radius is assumed not to change.

Under these assumptions, the mean value of the instantaneous wear depth that must be considered for wheel transverse wear estimation is no longer needed, and only the fluctuation of the instantaneous wear will determine the evolution of wheel polygonization.

3.2.2 Simulation scheme

Almost all of the existing prediction programs for wheel wear follow a closed-loop simulation scheme. Compared to the wheel transverse profile prediction, the simulation of polygonal wear has its particularities. A general loop simulation scheme for railway wheel polygonization is illustrated in Figure 3-1, which can be divided into four steps.

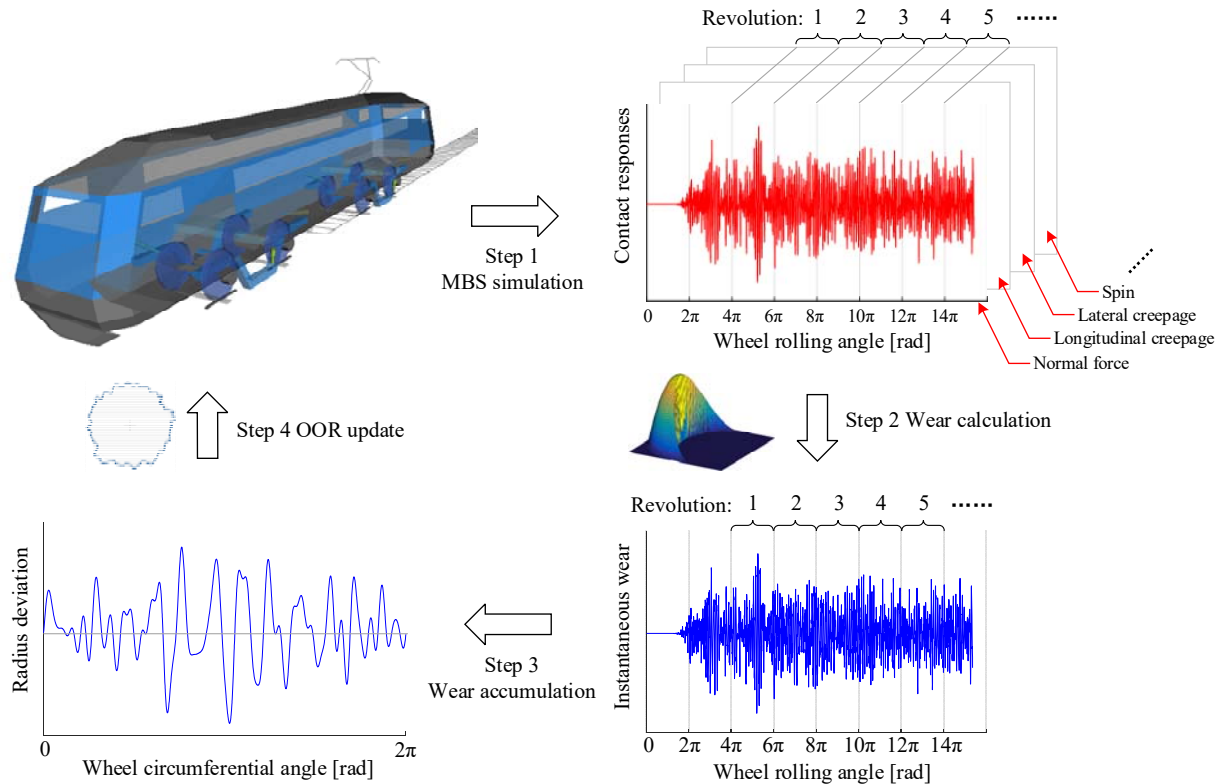


Figure 3-1 Loop simulation scheme for railway wheel polygonization

Step 1 (MBS simulation): The Multi-Body System (MBS) simulation is responsible for calculating the contact responses for the wear estimation. If the Archard wear model [63] combined with FASTSIM is used, nine contact parameters are needed: normal force, creepages (longitudinal, lateral, and spin), contact patch size (semi-axis a and b), Kalker coefficients ($C11$, $C22$, and $C23$).

Step 2 (Wear calculation): The x-coordinate of all the contact responses is replaced by the wheel rolling angles in order to facilitate the calculation of the polygonal wear for each wheel revolution, as well as the accumulation of the circumferential wear of multiple wheel revolutions. The instantaneous wear depth is calculated in real-time so that the circumferential wheel shape is allowed to evolve. Under this circumstance, the wear model used here is actually no longer a ‘long-term’ wear model, but a ‘short-term’ wear model instead.

Step 3 (Wear accumulation): The instantaneous wear depth is first interpolated, so as to be equally distributed for every circle (4096 points for one circle), and then accumulated and averaged by a number of wheel revolutions to obtain the polygonal wear around the wheel circumference for one iteration. The minimum number of wheel revolutions required for a convergent result is scenario dependent, and this will be discussed in Section 3.3.4.

Step 4 (OOR update): The circumferential wheel shape is updated for the next MBS simulation. The newly generated OOR should be smoothed, filtered to exclude high frequencies that are either not of interest or are generated by artificial spikes, and ensured to have continuity from the start to the end as the OOR is a cyclic closed curve. These three tasks can be completed simultaneously with the modified Fourier Series method (see Figure 5-3). Finally, the new OOR is scaled with an amplification coefficient to represent a much larger number of revolutions. There is not a specific criterion for the amplification coefficient, but only a

compromise between the computing accuracy and efficiency. Here this amplification coefficient should be distinguished from the wear coefficient used for calculation of instantaneous wear.

In this dissertation, Simpack is adopted for the MBS simulation (step 1), and Matlab is used to implement all other steps (from step 2 to step 4). As a large number of iterations need to be launched in order to observe the evolution of wheel polygonization, the simulation procedure is designed to be highly automate and parametric, which can also facilitate the subsequent parameter analysis. The simulation procedure is shown in Figure 3-2.

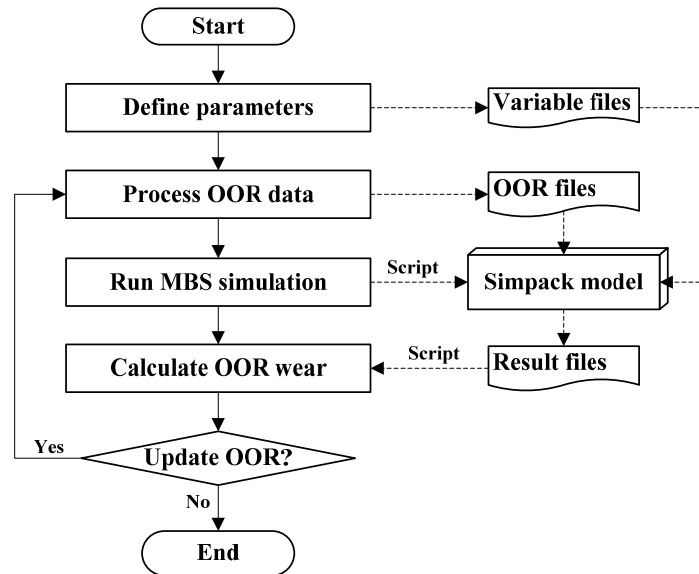


Figure 3-2 Simulation procedure

The whole looping simulation procedure is integrated and controlled in Matlab. All Simpack parameters, including configuration parameters and vehicle/track parameters, are defined and stored in variable files that serve as inputs to Simpack model. The OOR data stored in OOR files in a specified format that can be read by Simpack are processed during simulation, including spikes/pits removal, curve smoothing, and OOR profile updating. The MBS simulation is launched in Matlab via a Simpack script coded to perform equilibrium/preload and time integration consecutively. Further, the dynamic responses are outputted to result files, and the data needed are then transferred to Matlab via a script to calculate the polygonal wear.

3.2.3 Wear model

Four representative wear models, devolved by BRR, KTH, USFD, and Professor Zobory, has been found to present a similar ability to reflect the fluctuation of the instantaneous wear under various circumstances. This will be discussed in detail in Chapter 4. As a result, the selection from among these wear models does not matter significantly. The KTH wear model is employed here to calculate the instantaneous wear depth, while similar results can be obtained as well with other wear models.

3.3 Some rules for the evolution of railway wheel polygonization

It is generally believed that the railway wheel polygonization is a fixed-frequency issue. According to the simulation, this fixed frequency could come either directly from the excitation to the vehicle-track dynamic system, or from some modal resonance that can be triggered and excited effectively by excitation to fluctuate the instantaneous wear in the same modal frequency. The excitation to the vehicle/track dynamic system can either be the track excitation (rail irregularity, sleeper passing oscillation, and so on) or the wheel OOR on itself if the motor vibration and the aerodynamics are not considered. In the real case, the polygonal wear must be formed gradually under excitation of both track excitation and newly developed OOR simultaneously during the evolution, which behaves as a complicated process. To make this complex issue easier to understand, a single wheelset model is intentionally adopted to expound some basic rules and features that the instantaneous wear will follow. Simpack is used as the MBS package. A wheelset of a locomotive with 23-tonne axle load is adopted as the research object. A co-running track model with sleeper following the wheelset is used to simply represent the track flexibility. Guidance forces with linear stiffness and damping in three axes are applied at both sides of the wheelset axle, representing the dynamic coupling effect from the bogie frame. The wheel profile is JM3 [64], and the rail profile is CN60 [65]. The main parameters of the model are listed in Table 3-1.

Table 3-1 Main model parameters

Main parameters	Value	Unit
Wheelset mass	3562	kg
Radius	0.625	m
Preload on each primary suspension	105	kN
Longitudinal stiffness of primary suspension	3.6e7	N/m
Lateral stiffness of primary suspension	4.8e6	N/m
Vertical stiffness of primary suspension	2.9e6	N/m
Vertical damping of primary suspension	4e4	Nm/s
Sleeper mass	308	kg
Vertical stiffness of ballast	5.4e8	N/m
Vertical damping of ballast	1.5e5	Ns/m

3.3.1 The basic rule for initial OOR to evolve

Assuming that the wheel has an initial OOR with a single harmonic order (the wheel circumference can be exactly divided by the wavelength), and the track is perfect without any irregularities, when the wheel is running at a constant speed, there will be a cyclic excitation caused by this initial OOR with a single frequency according to Equation (3-1).

$$\text{Frequency} = \text{Speed} / \text{Wavelength} \quad (3-1)$$

All contact responses, as well as the instantaneous wear depth, will fluctuate with the same excitation frequency, but can have different phases. As a result, the updating of the circumferential wheel shape after one wheel revolution comes down to a simple mathematical problem illustrated as Equation (3-2).

$$A \cdot \sin(fx) - B \cdot \sin(fx + \phi) = \sqrt{A^2 - 2AB \cos \phi + B^2} \cdot \sin(fx + \arctan \frac{-B \sin \phi}{A - B \cos \phi}) \quad (3-2)$$

where: A is the fluctuation amplitude of initial OOR, B the fluctuation amplitude of instantaneous wear depth, f the excitation frequency, ϕ the phase of instantaneous wear depth with respect to initial OOR, and x the wheel rolling angle. Note that the mean value of OOR will always be subtracted, and the focus is only put on the fluctuation part. So the growth ratio of OOR can be expressed as (3-3):

$$\text{Growth ratio} = \frac{\sqrt{A^2 - 2AB \cos \phi + B^2}}{A} = \sqrt{(B/A)^2 - 2(B/A) \cos \phi + 1} \quad (3-3)$$

The growth ratio can be plotted as a 3D figure with B/A and ϕ as two individual variables, as shown in Figure 3-3.

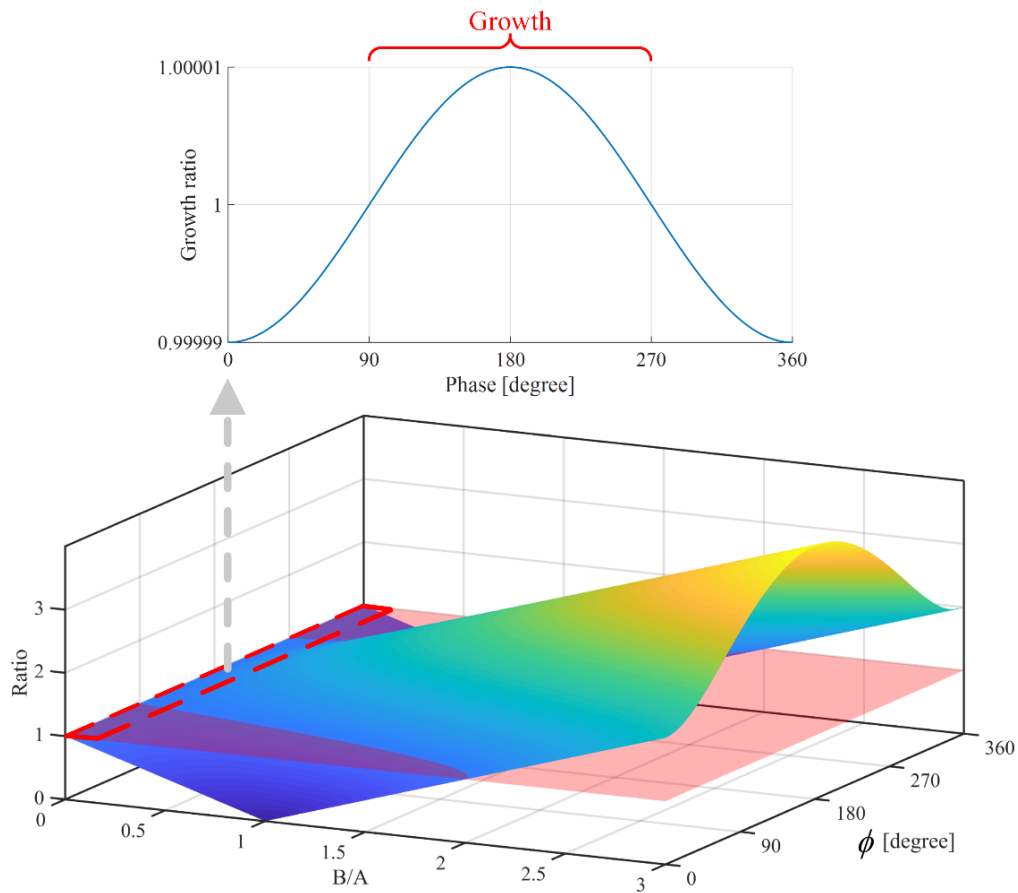


Figure 3-3 Growth ratio against B/A and ϕ

Having a look at the lower 3D sub-figure in Figure 3-3, the surface above the pink plane (ratio=1) indicates that the OOR will grow. Otherwise, the OOR will diminish. Although the growth ratio is determined by B/A and ϕ together, but in reality, B/A is extremely small for one wheel revolution, meaning that the situation can only occur in the dashed red region, where the phase ϕ is the only factor determining whether the OOR will grow or not. By zooming in this region and switching to the front view, the relationship between the phase ϕ and the growth rate of OOR can be presented in the upper sub-figure (assuming $B/A=1e-5$). If the phase

between the instantaneous wear depth and the initial OOR is within 90° to 270° range, the initial OOR will grow. At 180° degree, the growth rate reaches the maximum. Although the growth ratio is at a very low order of magnitude for one wheel revolution, the effective growth ratio will be amplified with running distance, and then the change of the circumferential wheel shape can be notable.

3.3.2 The effect of excitation on contact parameters

The excitation position of OOR and rail irregularity is illustrated in Figure 3-4, as they are applied in Simpack. The OOR changes the nominal radius of the wheel to vary the wheel profile only in the vertical direction, while the rail irregularity alters the position of the rail profile in both vertical and lateral directions. Under excitation, the position of the contact patch will be searched for every time step accordingly, and all contact parameters will be varied correspondingly. Theoretically, if a single-frequency harmonic excitation of OOR or vertical rail irregularity is applied, all contact responses will fluctuate with the same excitation frequency. But the phase of different contact parameters against the excitation can be different from each other, and the phase of contact parameters caused by OOR and vertical rail irregularity respectively is also different from each other, which presents as a very complicated phenomenon that is hard to interpret.

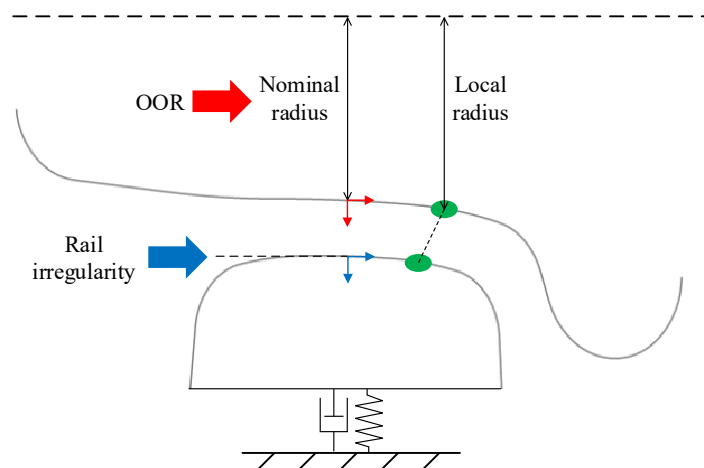


Figure 3-4 Excitation position of OOR and rail irregularity

Figure 3-5 shows an example of the phase of some contact parameters against a harmonic excitation of OOR and vertical rail irregularity, respectively. For this example, the scenario is set the same for OOR and vertical rail irregularity to facilitate the comparison between them: the wheelset speed is 120 km/h; the excitation wavelength is $1/18^{\text{th}}$ of the wheel circumference, and the excitation amplitude is 0.01 mm. The contact parameters being investigated include the nine contact responses used as inputs to the KTH wear model, as well as the instantaneous wear depth calculated by the KTH wear model.

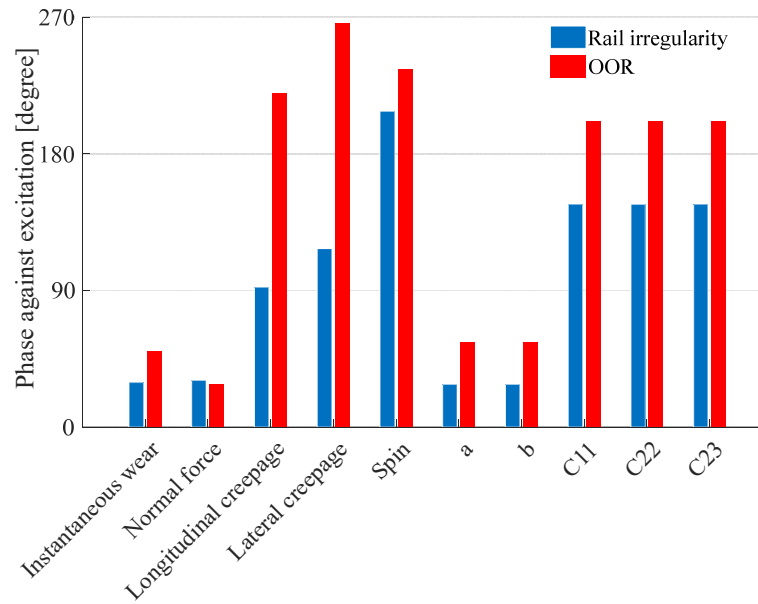


Figure 3-5 Phase of contact parameters against excitation

Two items of information can be obtained from Figure 3-5. First, the contact responses can present different phases relative to each other. More simulations show that the phase between contact responses is scenario dependent, and it may not be interpreted as a fixed-relationship. Second, the phase of contact responses caused by OOR and vertical rail irregularity respectively is also different. As a result, the phase of the instantaneous wear depth caused by OOR is different from that by vertical rail irregularity. However, in some self-developed 2D MBS packages [66], the OOR and vertical rail irregularity are both applied to the contact penetration directly as a simplification. With this simplification, the effect of OOR and vertical rail irregularity is exactly the same, and the phase between wear and excitation can be analytically derived. Actually, in a more realistic situation, the contact penetration should be a function of the excitation, but not a direct input as an excitation. This implies that the application of the excitation (OOR or rail irregularity) in the simulation has a determining influence on the results, given that the phase of instantaneous wear with respect to initial OOR is the key indicator (see Section 3.3.1).

3.3.3 The evolution tendency curve

Before introducing the ‘evolution tendency’ curve, the instantaneous wear FRF that demonstrates the response of the instantaneous wear against excitation for a wide range of frequencies has to be prepared. It can be drawn by sweeping the wheel velocity with a fixed-wavelength excitation (vertical rail irregularity or initial OOR) and then extracting the amplitude and the phase of the instantaneous wear fluctuation with respect to the excitation. It is worth noting that this fixed wavelength must be exactly divided by the wheel circumference. Otherwise, the calculated instantaneous wear is not periodic for each wheel revolution. In this case: the fixed wavelength of excitation is one-fifth of the wheel circumference; the amplitude of excitation is 10 μm , and the wheelset speed is swept to get the frequency response up to 500 Hz. The initial OOR and the vertical rail irregularity are applied as excitation respectively with the same settings to allow a comparison between them. The obtained instantaneous wear FRF is shown in Figure 3-6.

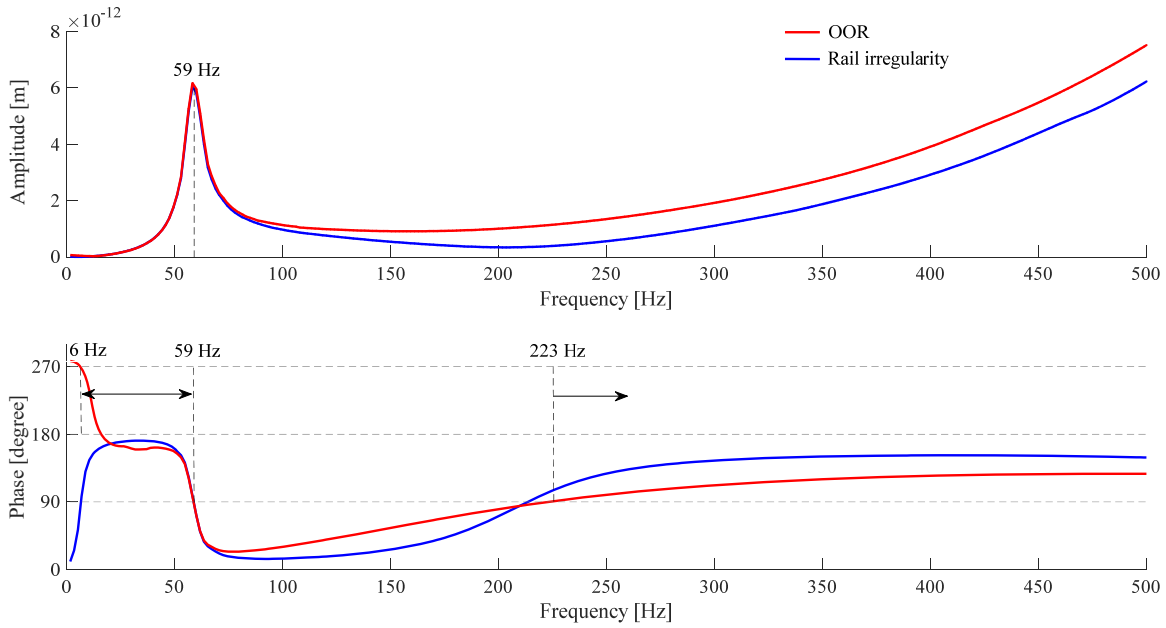


Figure 3-6 Instantaneous wear FRF

As can be seen in Figure 3-6, the amplitude spectrum of the OOR and the vertical rail irregularity are similar to each other, with their discrepancy gradually becoming bigger for higher frequencies. This implies that the OOR and the vertical rail irregularity have a similar effect in terms of the excitation amplitude, which is reasonable. However, the phase spectrums between them can be more different from each other, although the overall trend is similar. Despite this, the most important aspect is that the phase spectrum of the OOR can be used to identify the frequency range in which the initial OOR tends to grow or diminish. As has been discussed in Section 3.3.1, the initial OOR will grow when the phase between the instantaneous wear depth and the initial OOR is within 90 to 270 degree. Based on this rule, the frequency range within which the initial OOR tends to grow can be marked in Figure 3-6, and is from 6 Hz to 59 Hz and above 223 Hz, in this case. The 59 Hz peak is the resonant frequency of the vertical mode of wheelset & sleeper against the ground, which can be approximately deemed as the P2 resonance frequency. This frequency is important, as it is not only the most dominant resonant frequency in the amplitude spectrum but also the turning point at 90 degrees in the phase spectrum. This frequency can be simply estimated by Equation (3-4) with parameters listed in Table 3-1. While it is not clear what determines the 6 Hz and the 223 Hz. Note that the 6 Hz will be ignored in the following discussion.

$$f = \sqrt{(\text{sleeper vertical stiffness})/(\text{wheelset mass}+\text{sleeper mass})} = (\sqrt{5.4e8/(3562+308)})/2\pi \approx 59 \text{ Hz} \quad (3-4)$$

Given the instantaneous wear FRF, the amplitude and phase spectrum of it can be further combined to obtain an ‘evolution tendency’ curve that can indicate both the evolving direction (to grow or to diminish) and the evolution speed of the initial OOR over a range of frequencies in a single curve. Remember that in Figure 3-3 (the upper sub-figure), the growth ratio is a cosine function of the phase between the initial OOR and the instantaneous wear. By shifting this cosine function down by 1, to set 0 as the boundary line judging the evolution direction (to grow or to diminish), which becomes like $y = -\cos(x)$, and utilizing both information from the amplitude and phase spectrum of the instantaneous wear FRF, the evolution tendency curve can be

plotted using Equation (3-5), which is shown in Figure 3-7.

$$\text{Evolution tendency} = -\cos(\text{Phase}) \times \text{Amplitude} \quad (3-5)$$

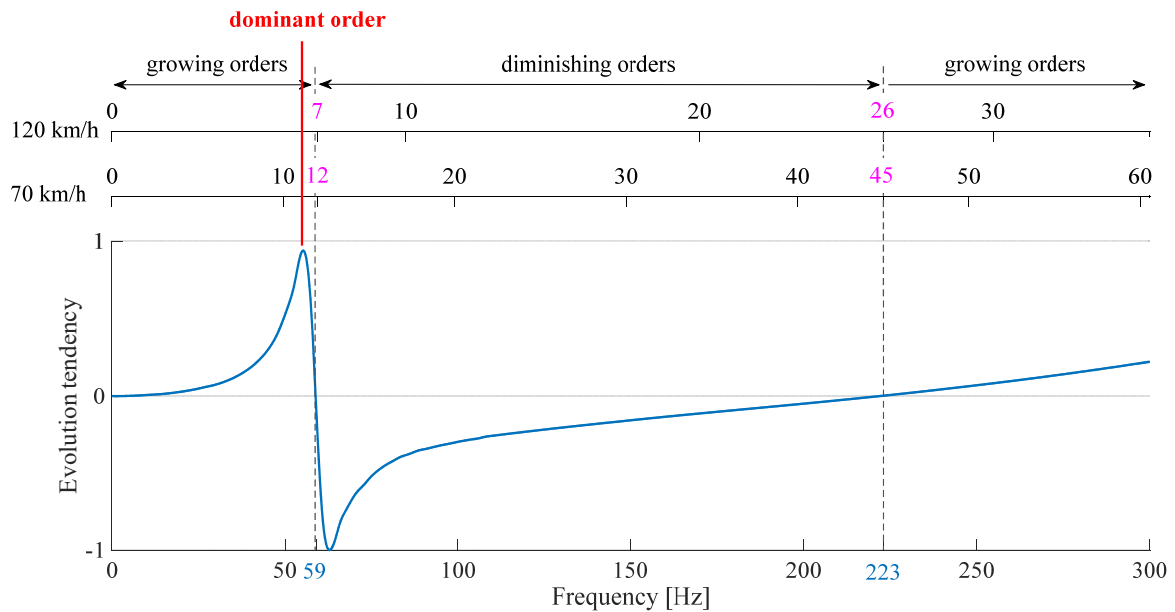


Figure 3-7 Evolution tendency curve and corresponding growing and diminishing orders at speeds of 70 km/h and 120 km/h

Note that the evolution tendency curve is normalized to be located between -1 and 1, as its specific value is meaningless and its significance only lies in the comparison between different frequencies. If the evolution tendency is above zero, the initial OOR tends to grow on its own. Otherwise, the initial OOR will diminish on its own. The higher absolute value of the evolution tendency means faster evolution speed. Based on this curve, the orders corresponding to the frequencies at speeds of 70 km/h and 120 km/h, as two examples, are plotted in the same figure according to Equation (3-1), which is shown in the upper part of Figure 3-7. To facilitate the description, the frequencies at which the evolution tendency turns its direction are called ‘boundary frequencies’; the order corresponding to the ‘boundary frequency’ is called ‘boundary order’; the orders that will grow on their own are called ‘growing orders’; and the orders that will diminish on their own are called ‘diminishing orders’. In Figure 3-7: 59 Hz and 223 Hz are two boundary frequencies, which are marked as blue numbers; the 12th and 45th orders are two boundary orders at 70 km/h, and the 7th and 26th orders are two boundary orders at 120 km/h, which are marked as pink numbers. For the speed of 70 km/h, the orders below 12 are growing orders, and those from 12 to 45 are diminishing orders, and so on. With this figure, the order that would grow the most dominantly on its own can be identified, which is the 11th order at 70 km/h and the 6th order at 120 km/h.

To verify the above rule, the OOR development in the presence of a measured initial OOR is simulated to check which order will grow or diminish as well as their evolution speed, which is shown in Figure 3-8. Here no rail irregularity is applied to avoid interference. The parameters used are as follows: the speed is 70 km/h; the number of iterations is 10; the number of wheel revolutions for each iteration is five (although one is enough);

the amplification coefficient is 1×10^6 for each iteration; the orders above 40 are filtered to exclude high-frequency components, so orders above 45 (corresponding to 223 Hz) will not be presented in the figure.

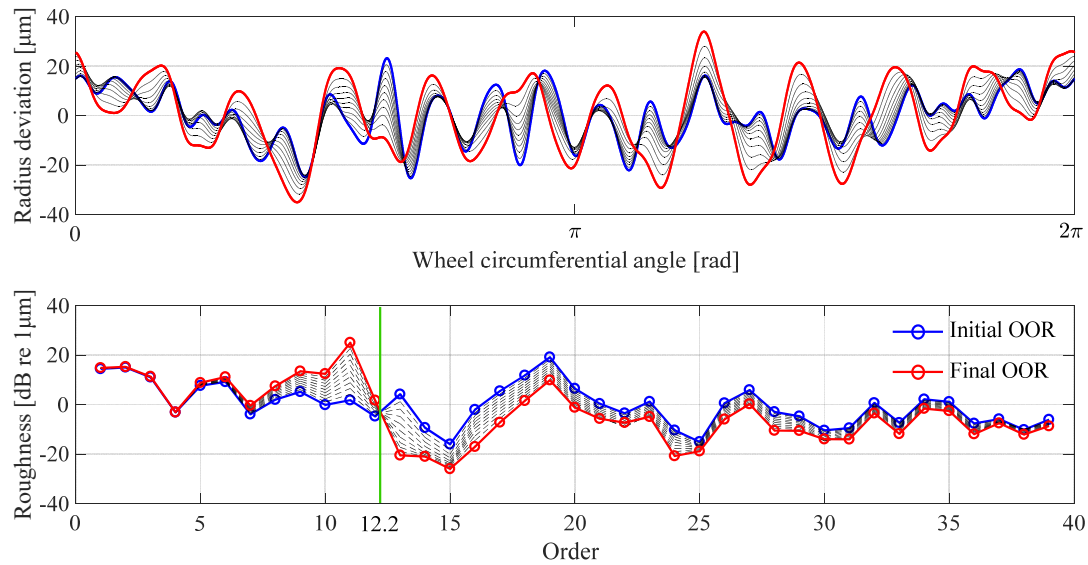


Figure 3-8 Evolution of OOR due to initial measured OOR

As can be seen from Figure 3-8, the orders of 12 and below grow while those of 13 and above diminish, with the green line denoting the transition, which corresponds well to the information in Figure 3-7. The order position at around 12.2 is corresponding to 59 Hz as the boundary in this case. It can also be found that there is a good consistency in terms of the evolution speed (either growth or diminishment) for all the orders between Figure 3-7 and Figure 3-8. Especially, although the roughness of the 11th order is rather low compared to that of other orders at the beginning, it eventually becomes the most dominant order after several evolutions just as Figure 3-7 predicts. Through this verification, it can be concluded that the evolution tendency curve is a useful tool to predict the evolution of OOR.

3.3.4 Convergency analysis on wheel revolutions

As shown in Figure 3-1, for step 3 of the simulation workflow for railway wheel polygonization, the circumferential wear depth is accumulated and averaged by a number of wheel revolutions to get the polygonal wear around the wheel circumference for one iteration. The number of wheel revolutions required for a convergent result is scenario dependent, which will be discussed for the case of harmonic excitation and random excitation respectively.

3.3.4.1 The case of harmonic excitation

For excitation of rail irregularity, the wavelength could be arbitrary in reality. If the wheel circumference can be exactly divided by the wavelength, the instantaneous wear is periodic for every wheel revolution. But if the wheel circumference cannot be exactly divided by the wavelength or the wavelength is bigger than the wheel circumference, the instantaneous wear depth will be different at any point on the wheel circumference for

consecutive wheel revolutions. Even so, for a harmonic case, the instantaneous wear will always be repeated for a running distance of some wheel revolutions theoretically, no matter what the wavelength is. The minimum number of wheel revolutions for the occurrence of repetition of instantaneous wear can be analytically identified by a uniform Equation (3-6).

$$L = \frac{n}{m}C \quad (3-6)$$

where: L is the wavelength of rail irregularity, C is the wheel circumference, and m and n are two natural numbers. By ensuring m and n are relatively prime for each other, n is the minimum number of revolutions for the occurrence of repetition of instantaneous wear. Some representative examples are presented below:

$$L = \begin{cases} (1/5)C \\ (1/5.3)C \\ (1/5.74)C \\ (2/1)C \\ (3.3/1)C \end{cases} \Rightarrow L = \begin{cases} (1/5)C \\ (10/53)C \\ (50/287)C \\ (2/1)C \\ (33/10)C \end{cases} \rightarrow n = \begin{cases} 1 \\ 10 \\ 50 \\ 2 \\ 33 \end{cases}$$

If $n=1$, one wheel revolution is enough for one iteration as the circumferential wear will be repeated for every wheel revolution. If $n \neq 1$, the minimum number of circles for one iteration should be set to the multiple of n , by which the fluctuation of the averaged instantaneous wear depth will remain at a very low level, as the instantaneous wear of each wheel revolution will be just counteracted by each other. This can be checked with Figure 3-9 as an example ($L=C/5.3$). The standard deviation is used to indicate the fluctuation of the averaged instantaneous wear depth for specified wheel revolutions (x-coordinate). As can be seen, the standard deviation of the averaged instantaneous wear depth is minimal for any wheel revolutions that are multiples of 10, which meets Equation (3-6) very well, and decreases gradually with the increase of wheel circles.

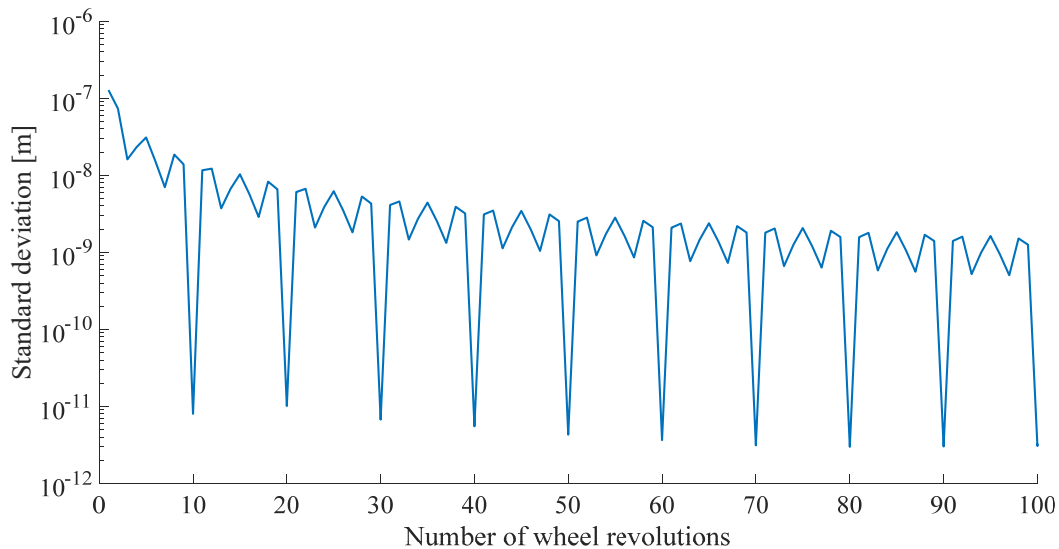


Figure 3-9 Standard deviation of averaged instantaneous wear depth for specified wheel revolutions ($L=C/5.3$)

This analysis implies that any rail irregularity with a wavelength that cannot precisely divide into the wheel circumference cannot form an OOR easily. In reality, a typical example is the sleeper passing oscillation. Although the sleeper passing vibration is a constant excitation with a fixed wavelength, which seems conform to a fixed-wavelength mechanism, however, if the sleeper distance cannot accurately divide into the wheel

circumference, it is not easy for a corresponding OOR to develop. Even the sleeper distance happens to exactly divide into the wheel circumference, but the wheel radius will always decrease gradually due to wear so that the situation of exact division cannot last for a very long time. This could be a factor as to why, in reality, the OOR corresponding to the sleeper passing frequency is usually not the most dominant one.

In addition, for the case of initial OOR as the excitation on itself, the maximum wavelength of OOR is the wheel circumference itself, and it is not likely for those wavelengths that cannot exactly divide into C to develop significantly, as the OOR wavelength must be continuous around the wheel circumference. During the iterations, the newly updated OOR will always be ensured to continue around the wheel circumference by some smoothing method, e.g. the modified Fourier filter method used in this thesis (see Figure 5-3). Obviously, the instantaneous wear depth caused by the initial OOR is strictly periodic for every wheel revolution, and only one circle is needed for this circumstance.

3.3.4.2 The case of random excitation

Under excitation due to random rail irregularity, the instantaneous wear depth is naturally random for every wheel revolution. In this case, the running distance should be long enough to get a convergent result of the averaged instantaneous wear depth for one iteration. A standard track irregularity spectrum FRA 5 (the 5th class track defined by Federal Railroad Administration of US) [67] is adopted to carry out a convergency analysis on the number of wheel revolutions under excitation of random rail irregularity, which is presented in Figure 3-10. It can be seen that the standard deviation of the averaged instantaneous wear depth becomes convergent after 1000 wheel turns. This implies that if the number of wheel revolutions is not specified to be large enough in the case of random rail irregularity, some significant errors may be introduced.

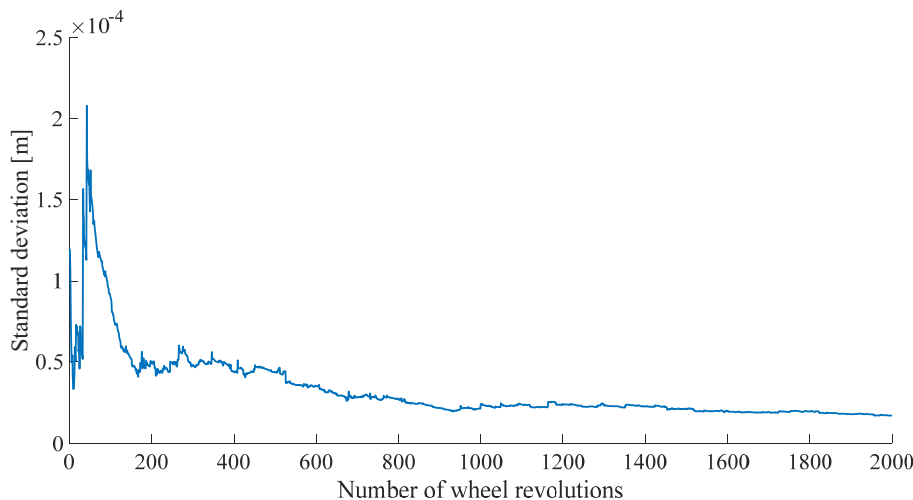


Figure 3-10 Convergency analysis on the number of wheel revolutions under excitation of random rail irregularity (FRA 5)

3.3.5 Linearity of excitation

It is found that the fluctuation of the instantaneous wear depth caused by OOR and rail irregularity

simultaneously is a simple linear sum of those caused by OOR and rail irregularity individually, even though the dynamic system contains non-linear elements. An example of a random case is presented here. The initial OOR is configured with the measured data, and white noise is applied to represent the vertical rail irregularity. The result is shown in Figure 3-11. The solid blue curve is the fluctuation of the instantaneous wear depth caused by vertical rail irregularity of white noise individually, the solid red curve is that caused by initial OOR individually, and the solid green curve is that caused by vertical rail irregularity and initial OOR simultaneously. The dashed black curve is the sum of solid blue curve and solid red curve. As can be seen, the solid green curve matches the dashed black curve perfectly. If a random case is proven, let alone a harmonic case. More simulations show that the linearity of excitation also applies for various combination of OOR and rail irregularity, which means that the overall result of the instantaneous wear depth caused by OOR and/or rail irregularity with multiple frequency components is the linear superposition of those caused by OOR and/or rail irregularity with single harmonic frequency. This characteristic is important to aid the understanding of more complex scenarios.

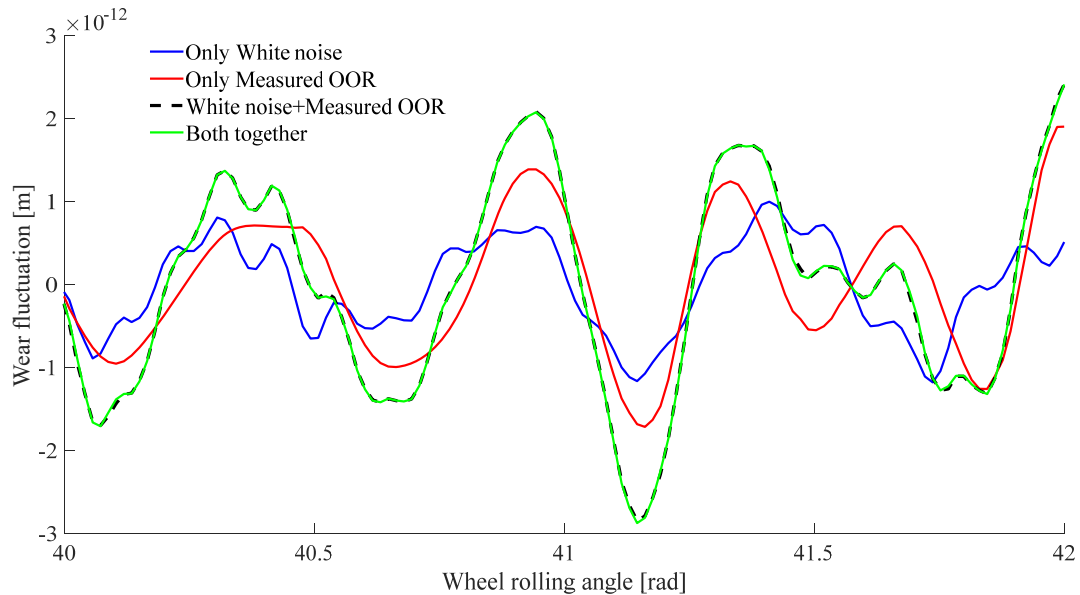


Figure 3-11 Linearity analysis for instantaneous wear fluctuation caused by vertical rail irregularity of white noise and measured OOR

3.3.6 Contribution of newly developed OOR

Considering the linearity of excitation, the iterative process for OOR evolution can be presented in Figure 3-12. In this figure: EOT is the abbreviation of Excitation Of Track, and OOR means wheel Out-Of-Roundness; W_{EOT} is the fluctuation of polygonal wear contributed by EOT individually (dashed blue arrows), W_{OOR} is the fluctuation of polygonal wear contributed by OOR individually (dashed red arrows), and W_{TOTAL} is the sum of them amplified by a large coefficient k (assuming the same value for every iteration). All the superscripts indicate the iteration step; OOR^0 is the initial OOR. For the i^{th} iteration, the OOR is updated by: $\text{OOR}^i = \text{OOR}^{i-1} - W_{\text{TOTAL}}^i$. With n iterations, the OOR evolution is obtained.

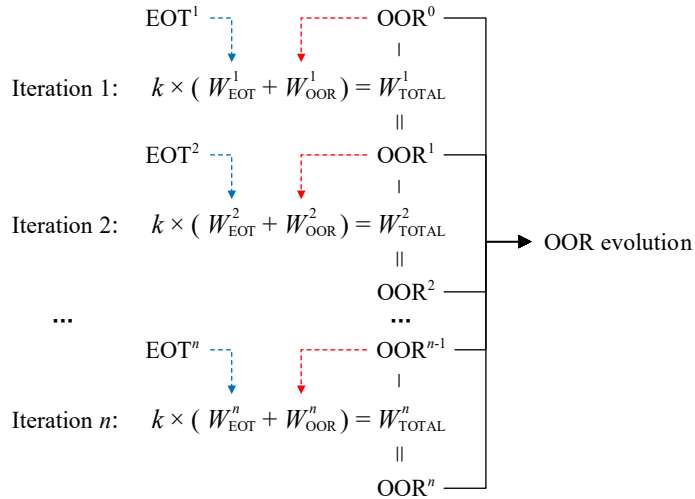


Figure 3-12 Iterative process for OOR evolution

As can be seen from Figure 3-12, the wheel OOR is gradually evolving with the contribution of both track excitation and newly developed OOR. If track excitation is the same for the whole iteration process, the W_{EOT} is actually the same for each iteration. In this case, the OOR evolution contributed by track excitation is the linear sum of each W_{EOT} , which can be simply expressed as $n \times k \times W_{EOT}$ (if k is a constant). On the contrary, the W_{OOR} will always change along with the iterations due to introduction of newly developed OOR, and the contribution of W_{OOR} to the OOR evolution could be positive or negative depending on the range of excitation frequency (see Section 3.3.3).

An example is presented in Figure 3-13 to demonstrate the negative effect of newly developed OOR on OOR growth. In this example: only vertical rail irregularity with a harmonic wavelength ($C/13$) is applied as the track excitation persisting for the whole iteration process; the fluctuation amplitude of rail irregularity is $10 \mu\text{m}$; k is 1×10^6 as a constant; the number of iterations (n) is 10, the speed is 70 km/h. In Figure 3-13, the dashed blue curve is the imaginary final OOR that would evolve to 31.15 dB caused by rail irregularity alone, without contribution from newly developed OOR; the solid red curve is the actual final OOR that evolves due to both rail irregularity and newly developed OOR, with nine dashed black curves indicating the OOR at discrete steps during iterative process. It is evident that the newly developed OOR plays a negative role in resisting the OOR growth in this case. This is because the 13th order is a diminishing order at a speed of 70 km/h, as shown in Figure 3-7.

Having a closer look at Figure 3-13, after around five iterations when the radius deviation approaches $10 \mu\text{m}$ (the amplitude of rail irregularity) corresponding to the roughness of 20 dB, the OOR growth stops for further iterations. This is because when the newly developed OOR has reached to the same roughness level of the rail irregularity, the instantaneous wear depth caused by them respectively is comparable to each other, and thus will be counteracted. This is an interesting phenomenon as it implies that the roughness level of the OOR will not exceed that of the rail irregularity for diminishing orders.

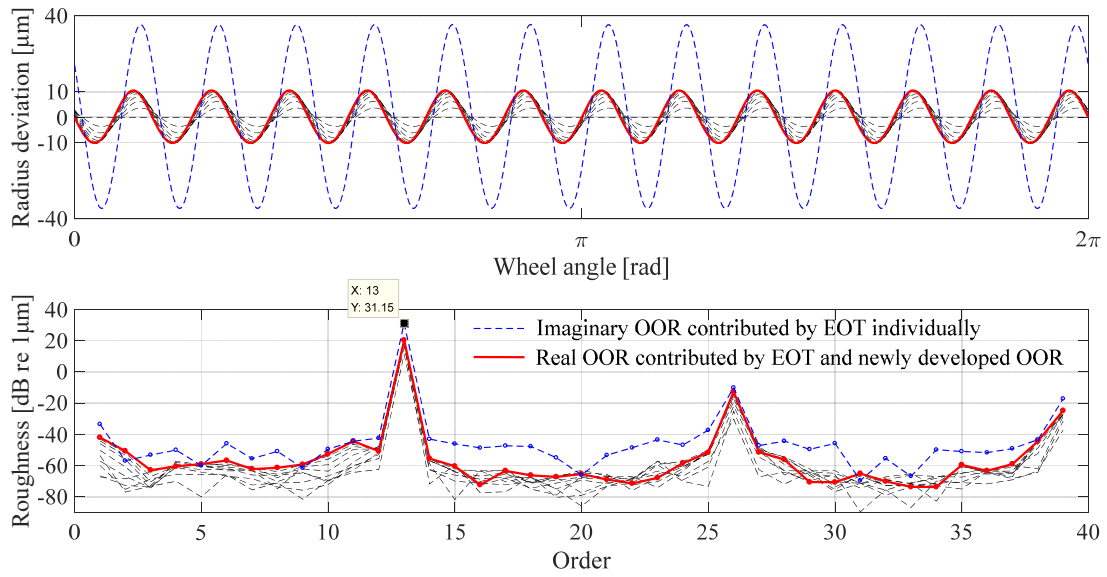


Figure 3-13 The negative effect of newly developed OOR on OOR growth (the 13th Order)

On the contrary, for growing orders, the newly developed OOR will accelerate the OOR evolution. Continuing the above case, if only changing the wavelength of vertical rail irregularity to $C/11$ that will excite a growing order of 11, the roughness of the final OOR is accelerated from 31.5 dB to 43.06 dB due to the contribution from the newly developed OOR, as shown in Figure 3-14. Given that the 11th order is the one that would grow the most dominantly on its own if the excitation frequency of rail irregularity is corresponding to the 11th order, the OOR will evolve rapidly.

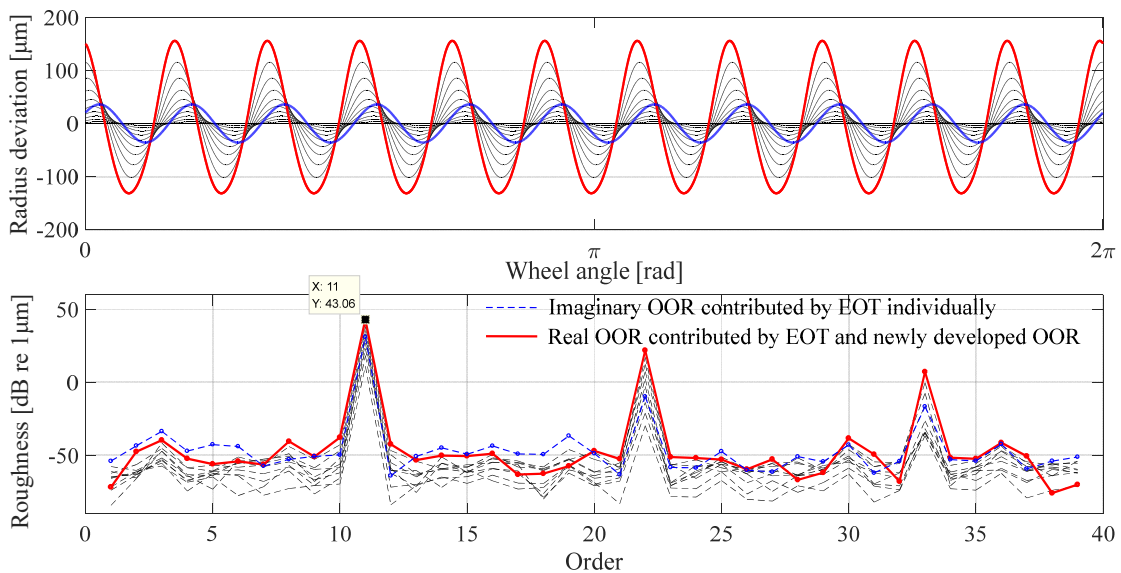


Figure 3-14 The positive effect of newly developed OOR on OOR growth (the 11th Order)

3.3.7 Contribution of track excitation

Continuing the above section, the simulation is further carried out with consideration of track excitation, including both the random track irregularity and the sleeper passing oscillation. Most parameters are kept the

same as above, with some additional modifications being added: the random track irregularity is FRA 5; the sleeper distance is 0.6 m; a same initial OOR in Figure 3-8 is introduced but multiplied by 0.01 to reduce its weight; the amplification coefficient for each iteration is decreased from 1×10^6 to 1×10^4 to avoid contact detachment during the iteration; the wheel revolutions for one iteration is 1000. The sample of the random track irregularity is set to be uncorrelated for each iteration to avoid repetitive scenarios. The OOR evolution under excitation of only vertical FRA 5 and full FRA 5 consisting of vertical, lateral, rolling, and gauge irregularities, are presented in Figure 3-15 and Figure 3-16, respectively.

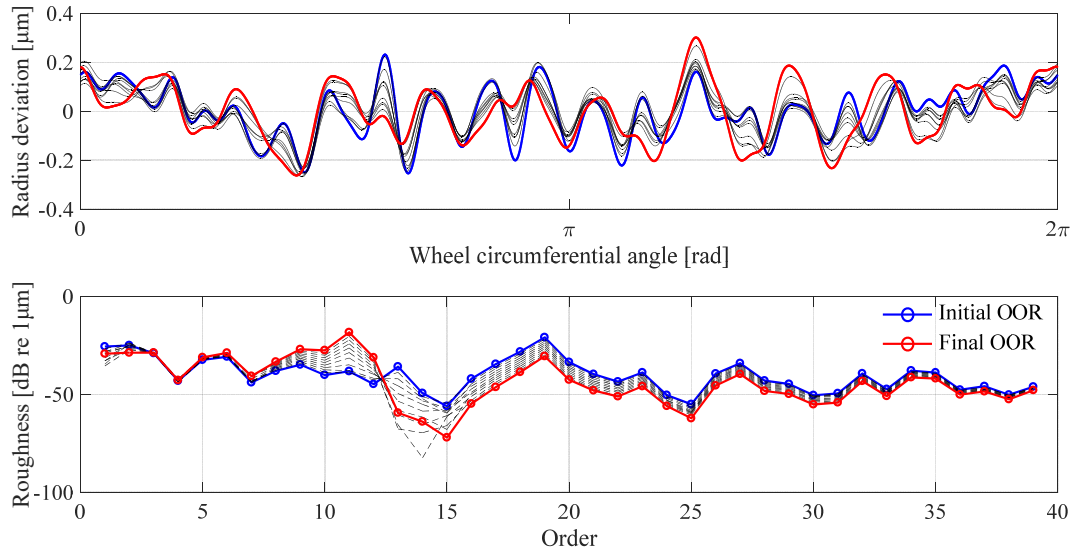


Figure 3-15 OOR evolution under excitation of **only vertical** random rail irregularity (FRA 5)

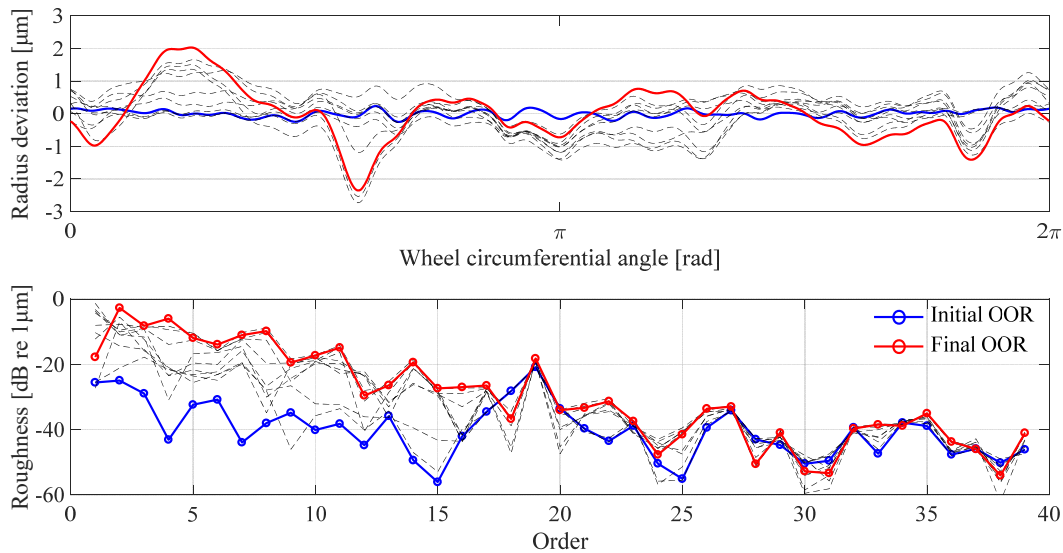


Figure 3-16 OOR evolution under excitation of **full** random rail irregularity (FRA 5)

As can be seen from Figure 3-15, if only the vertical track irregularity is applied, the evolution trend is similar to the case of only initial OOR without track excitation (see Figure 3-8), implying that the contribution of the vertical random track irregularity to the OOR evolution is negligible compared to that of initial OOR. This is

because the standard deviation of the averaged polygonal wear caused by random rail irregularity for a large number of wheel revolutions (1000 in this case) is convergent to a small amount, which has been discussed in Section 3.3.4.2. In this situation, the OOR evolution is still driven by the evolution tendency curve, with the 11th order growing the most dominantly. This is a further confirmation of the effectiveness of the evolution tendency curve. In addition, the sleeper passing frequency does not produce an obvious OOR ($3.925/0.6 \approx 6.5$) to develop because the wheel circumference cannot be exactly divided by the sleeper distance, and the number of wheel revolutions (1000) is large enough for the polygonal wear caused by sleeper passing oscillation to be counteracted among a large number of wheel revolutions, which has also been discussed in Section 3.3.4.1.

However, under the excitation of full FRA 5, the result of OOR evolution changes dramatically, as shown in Figure 3-16. As more excitation energy is contained in the full track irregularity and the main energy is located within the lower frequencies (below 20 Hz), the lower orders of OOR can develop more significantly than other orders. In this situation, the contribution of full track irregularity plays a dominant role in the OOR evolution, and the contribution of initial and newly developed OOR can be covered up. Note that the evolution tendency curve mentioned above is obtained only for the case of excitation in vertical direction (vertical rail irregularity or initial OOR), if other types of track irregularity (lateral, rolling, and gauge irregularities) are taken into consideration, the instantaneous wear FRFs for excitation of different types have to be obtained respectively so as to derive the corresponding evolution tendency curves which could be very different from each other. These evolution tendency curves should be synthetically utilized to establish a more instructive indicator to predict the OOR evolution under excitation of full random track irregularities, which however is not contradictory to the validity of evolution tendency curve for OOR prediction. This is a future work.

3.4 The general conditions for OOR to evolve

Based on the rules discussed above and previous research by the authors [68,69], the general conditions for OOR to evolve are proposed as follows:

- (1) The wheel is running at a constant speed for a long time to provide a stable environment for the OOR to develop gradually.
- (2) One or more structural modes can be significantly excited, leading to a persisting vibration with fixed frequency to the wheel/rail interface for a long time.
- (3) The energy distribution of the track excitation allows some structural modes to be excited dominantly.
- (4) The OOR order that would grow the most dominantly at a given speed can be identified by the evolution tendency curve obtained from the instantaneous wear FRF.

3.5 Discussions

3.5.1 Assumptions

In this thesis, the wheel radius is assumed not to change during the iterations. However, as the wheel radius is an important factor that can determine the number of OOR orders, the change of wheel radius should be

considered in the future. If so, the mean value of the instantaneous wear depth should be considered as it will determine the reduction speed of the wheel radius. In addition, the wheel transverse profile is also assumed not to change. Although this limitation could be broken through with the more complex program, it is believed that the change of transverse profile might have less importance on the wheel polygonization, but of course, it should be confirmed in the future.

3.5.2 Instantaneous wear FRF

The instantaneous wear FRF is a crucial indicator to identify the potential OOR orders that would develop dominantly. Especially the phase spectrum of the instantaneous wear FRF is the key indicator judging the ‘growing orders’ and ‘diminishing orders’. However, the phase between the instantaneous wear and excitation is rather hard to interpret. There are two phase-relationships: one is the phase between the excitation and the contact responses, the other is the phase between the contact responses and the instantaneous wear. Both of them present as a complicated issue, which has to be related to the modelling method. It seems that different modelling methods will directly lead to different results, which implies that at least some models may not be sufficiently realistic to predict OOR evolution faithfully. However, this does not detract from the fundamental observations made here. If the modelling method in terms of the two phase-relationships can be improved to match the reality, the evolution tendency curve obtained from the instantaneous wear FRF could be more significant as guidance.

3.5.3 Conditions for wheel OOR to develop

The possible root causes currently suspected in the academic community are pointing to the wheelset flexibility and the rail flexibility, although other component modes could also be the causes. No matter what the cause is, the common rule is that some structural mode must dominate the evolution tendency curve so that a corresponding OOR order can develop dominantly. Besides, in reality, the conditions of (2) and (3) mentioned in Section 3.4 cannot easily be confirmed as scenarios can vary significantly. For example, some structural modes can be dominantly excited in some sections of the track but not in other sections; some types of vehicle can have serious OOR issue on one track, but other types of vehicle may not. It is believed that a good match between the track and the vehicle is the best solution to avoid the OOR problem.

3.6 Summary

This chapter reports fundamental research into the general conditions for railway wheel polygonal wear to evolve. A common workflow for prediction of railway wheel polygonization is presented in terms of some assumptions, a simulation scheme, and a uniform wear model. Based on this workflow, some rules for the evolution of railway wheel polygonization are proposed providing innovative perspectives to understand the basic mechanism of OOR. After summarizing these rules, the general conditions for railway wheel polygonal wear to evolve are established. Some main points in this chapter are listed below.

- (1) The phase between the instantaneous wear and the excitation is the key indicator determining the OOR evolution direction (to grow or to diminish).
- (2) The evolution tendency curve obtained from the instantaneous wear FRF is proposed as a useful tool to predict the OOR evolution, especially for predicting the OOR order that would grow dominantly at a given speed.
- (3) If one or more structural modes can dominate the evolution tendency curve, and the energy distribution of track excitation allows this/these structural modes to be excited effectively, corresponding OOR orders can occur dominantly.

Chapter 4 Wear models for railway wheel polygonization

4.1 Introduction

The problem of railway wheel polygonization has been a critical issue affecting the regular operation of the railway network along with the increase of vehicle speed and axle load. To investigate the mechanism of this phenomenon through simulation, a prediction tool that can simulate the evolution of railway wheel polygonization is necessary. In order to achieve such a prediction tool, it is essential to adopt a wear model that should be suitable to simulate the circumferential wear of wheels. However, almost all of the existing wear models for rail/wheel application in the literature were initially designed to predict the wheel transversal profile change for a long distance of running. When focusing on the prediction of wheel polygonization, the wear models have to be converted to calculate the instantaneous wear of each contact patch for every time step in sequence, so that the circumferential wheel shape is allowed to evolve. In this sense, the converted wear model is actually no longer a “long-term” wear model, but an “instantaneous” wear model instead, although an amplification coefficient can be multiplied to the “instantaneous” wear to save computing time (see Figure 3-1). This “instantaneous” wear model should be able to distinguish the dominant frequencies of the contact responses so that a study on the fixed-frequency mechanism is possible. The fluctuation amplitude and phase of the instantaneous wear are also of interest, and these can depend on the characters of the converted “instantaneous” wear model. As a result, it is a fundamental issue to understand the applicability of existing wear models for the simulation of railway wheel polygonization.

Several wear models have been developed for wheel-rail applications [20,24,25,70-74]. The main task of establishing a wear model is to find the quantitative relationship between the contact parameters and the material loss, which can be simply illustrated as material loss=(wear coefficient) \times (wear index). The wear index (WI) is the combination of the contact parameters (e.g. $T\gamma$, $T\gamma/A$, or Nd) as variables used for the wear calculation. The wear coefficient is an indicator of the wear rate, which can only be obtained through experimentation. Some wear regimes (e.g. mild, severe, and catastrophic) can be partitioned with corresponding wear coefficients according to the level of WI. Interestingly, different wear models were developed with various WI, wear coefficients, and partition criteria of wear regimes, possibly due to different circumstances considered or different focus concentrated. Some researchers have carried out a comparative study on different wear models: Arizon [75] compared four wear functions, developed by Archard [63], Zobory [71], Pearce and Sherratt [70], and Jendel [73]/Enblom [76] respectively, by rewriting them in a common form with a wear velocity introduced as the uniform wear indicator. The quantitative relations between each wear model were obtained for mild and severe regimes, respectively. Pombo [77] compared three wear models developed by BRR, KTH, and USFD, with consideration of global and local methods. The comparison results revealed a good agreement in wear prediction obtained with the three wear models. Ding [78] carried out a comprehensive comparison on four wear models developed by Pearce [70], Zobory [71], Jendel [73] and

Braghin [79].

The above-mentioned comparative work were all standing in the perspective of wheel transversal profile prediction. Little research can be found from the perspective of wheel circumferential profile prediction. A typical study was from Johansson [80] who compared the Archard wear model and the frictional-work wear model in the calculation of the wear distribution in his PhD thesis. It turned out that both methods lead to somewhat similar wear depth. Currently, the most widely used wear models for predicting railway wheel polygonization is the Archard wear model that in its original form is feasible to calculate the instantaneous wear depth directly [14,35,69], as well as the frictional-work wear models which however need to be converted [3,22]. Among all of the existing popular wear models available for wheel-rail applications, it is imperative to have a thorough understanding of their applicability in railway wheel polygonization before they are adopted in the simulation program. This gap has not been investigated in a broad sense and is expected to be filled in this chapter.

Four representative wear models developed by BRR [70], KTH [73], USFD [24], and Professor Zobory [71] respectively, are selected to carry out a comparative study on their applicability in the simulation of railway wheel polygonization. All the wear models with consideration of global and local methods are first converted to allow the calculation of instantaneous wear according to specific assumptions. A uniform expression is analytically derived for all the converted wear functions to facilitate the comparison between each other. Several scenarios grouped by harmonic excitation and random excitation are adopted to assess the fluctuation of the instantaneous wear depth calculated by different wear models. The evolved polygonal wear around the wheel circumference is also compared among the wear models based on the prediction program in Chapter 3.

4.2 Wear models

In this section, some assumptions are first stated for the calculation of instantaneous wear depth of one contact patch. Then after briefly introducing the original definition of the wear models, the equation conversions are illustrated in details. Finally, a uniform expression of the converted wear functions is derived.

4.2.1 Assumptions

- The wheel transverse profile is assumed not to change, with the focus only on the change in the wheel circumferential profile. This assumption is justified by the fact that, when railway wheel polygonization occurs, the circumferential shapes measured at different wheel lateral positions are quite similar [13,30].
- The instantaneous wear is assumed to be equally distributed across the transverse section, which is implicit from the first assumption. For each contact patch in time sequence, an averaged wear depth is calculated.
- The wear is assumed to occur only in the sliding zone of the contact patch, without consideration of the plastic deformation. Hertz contact theory is adopted as the normal contact model and FASTSIM [81] as the tangential contact model in this chapter. Thus the contact area is an ellipse (with a: longitudinal semi-axis, and b: lateral semi-axis).

4.2.2 Definition of wear models

The original definitions of the four wear models being investigated are listed in Table 4-1. To facilitate the comparison, all the original wear functions are converted to SI units. As can be seen in Table 4-1, these wear models in their original definitions have different equation forms with different WI as the wear indicator (the variables in the equation). The partition criteria of the wear regimes are only applicable to the respective wear model on its own, and thus not comparable between different wear models. The wear coefficients are also varied due to different experimental scenarios and different materials tested.

Table 4-1 Original definition of wear models

Wear models	Wear functions	Wear regimes			Material	Remarks	
BRR	Wear rate [$\frac{m^2}{m}$]	Wear index $T\gamma$ [N]			Wheel: R8T Rail: BS11	Area loss per distance rolled	
	$0.25 \frac{T\gamma}{D} \times 10^{-12}$	$T\gamma < 100$					
	$\frac{25}{D} \times 10^{-12}$	$100 \leq T\gamma \leq 200$					
	$\frac{1.19T\gamma - 154}{D} \times 10^{-12}$	$T\gamma > 200$					
KTH	Wear volume [m^3]	p_z [Pa]	s [m/s]	K_{KTH} [-]	Wheel: R7 Rail: UIC 900A UIC 1100	Volume of worn material	
	$K_{KTH} \frac{Nd}{H}$	$p_z < 0.8H$	$s < 0.2$ or $s > 0.7$				$(1 \sim 10) \times 10^{-4}$
		$p_z < 0.8H$	$0.2 \leq s \leq 0.7$				$(30 \sim 40) \times 10^{-4}$
		$p_z > 0.8H$	any s				$(300 \sim 400) \times 10^{-4}$
USFD	Wear rate [$\frac{kg}{m \cdot m^2}$]	Wear index $\frac{T\gamma}{A}$ [N/m ²]			Wheel: R8T Rail: UIC 900A	Mass loss per running distance per contact area	
	$5.3 \frac{T\gamma}{A} \times 10^{-9}$	$\frac{T\gamma}{A} < 10.4 \times 10^6$					
	55.0×10^{-9}	$10.4 \times 10^6 \leq \frac{T\gamma}{A} \leq 77.2 \times 10^6$					
	$61.9 \frac{T\gamma}{A} \times 10^{-9}$	$\frac{T\gamma}{A} > 77.2 \times 10^6$					
Zobory	Wear rate [$\frac{kg}{s \cdot m^2}$]	\dot{E} [N · m/s · m ²]		K_{Zobory} [$\frac{kg}{N \cdot m}$]	Rail: BS 11	Stochastic energy flow density	
	$K_{Zobory} \dot{E}$	$\dot{E} < 4 \times 10^{-6}$		around 7×10^{-10}			
		$\dot{E} > 4 \times 10^{-6}$		around 21×10^{-10}			

4.2.3 Conversion of Wear models

There are two methods to apply a wear model, namely global method and local method. The difference between them can be seen in Figure 4-1. For the global method, the “global contact parameters” highlighted in red are used to calculate the wear. For the local method, the contact patch is discretised into elements to calculate the wear distribution with the “local contact parameters” highlighted in blue.

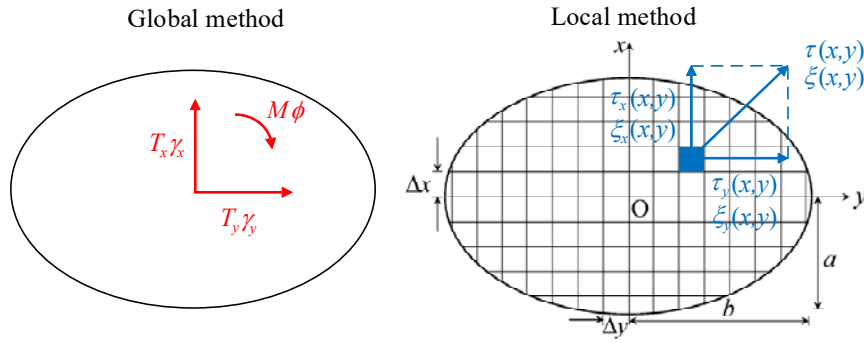


Figure 4-1 Global method and local method

We can define $T\gamma$ as:

$$T\gamma = |T_x\gamma_x| + |T_y\gamma_y| + |M\phi| \quad (4-1)$$

and locally:

$$\tau(x, y)\xi(x, y) = \sqrt{\tau_x^2(x, y) + \tau_y^2(x, y)} \cdot \sqrt{\xi_x^2(x, y) + \xi_y^2(x, y)} \quad (4-2)$$

where T_x , T_y , and M are the global longitudinal tangential force, the global lateral tangential force, and the global spin torque respectively; γ_x , γ_y , and ϕ are the global longitudinal creepage, the global lateral creepage, and the global spin respectively; $\tau(x, y)$ and $\xi(x, y)$ are the local tangential stress distribution and the local creepage respectively, with (x, y) indicating the local coordinates in the contact grid, and with subscript x and y indicating the direction components. $T\gamma$ is the WI for global methods, and $\tau(x, y)\xi(x, y)$ for local methods.

Without losing generality, the wear models can be represented as:

$$W_{BRR} = K_{BRR} \cdot \frac{T\gamma}{D} \left[\frac{m^2}{m} \right] \quad (4-3)$$

$$W_{USFD} = K_{USFD} \cdot \frac{T\gamma}{A} \left[\frac{kg}{m \cdot m^2} \right] \quad (4-4)$$

$$W_{Zobory} = K_{Zobory} \cdot \dot{E} \left[\frac{kg}{s \cdot m^2} \right] \quad (4-5)$$

where: W is the wear rate and K the wear coefficient, both with a subscript indicating the wear model.

Note that the KTH wear model is not defined as a wear rate, but a specific value of worn volume for given sliding distance and normal force. Obviously, it can be directly used to calculate the instantaneous wear. For those wear models defined as a wear rate, a “running distance” over one contact patch must be correctly multiplied to the wear rate to obtain the instantaneous wear. The obtained wear could be in the form of area, volume, or mass, depending on the definition of the wear models. By averaging the instantaneous wear of one contact patch, a single-value wear depth is obtained. For the global method, the averaging method is different depending on the wear models’ definition. For the local method, the wear distribution of one contact patch is averaged by accumulating the wear distribution longitudinally and then averaging laterally.

4.2.3.1 BRR model

The BRR wear model can only be used globally. According to the definition of the BRR wear model, to calculate the instantaneous wear for one contact patch, the “running distance” should be one wheel revolution which is associated with the wheel diameter D . The calculated BRR wear is an area loss across the wheel transverse profile. Then the area loss is divided by $2b$ to obtain the averaged wear depth. The conversion is given in Equation (4-6). As can be seen, the wheel diameter is actually counteracted.

$$H_{BRR} = W_{BRR} \cdot (\pi D) \cdot \frac{1}{2b} = K_{BRR} \frac{T\gamma}{D} \cdot (\pi D) \cdot \frac{1}{2b} = \frac{\pi K_{BRR}}{2b} \cdot T\gamma \quad (4-6)$$

where H represents the global wear depth with a subscript indicating the wear model. If assuming $K_{BRR}^* = \frac{\pi K_{BRR}}{2b}$, where K^* represents the global equivalent wear coefficient with a subscript indicating the wear model, Equation (4-6) becomes:

$$H_{BRR} = K_{BRR}^* \cdot T\gamma \quad (4-7)$$

4.2.3.2 KTH model

The KTH wear model was initially developed only for the local method [73] based on the Archard wear model [63] and FASTSIM [81]. The basic equation is as below:

$$V_{wear} = K_{KTH} \frac{Nd}{H} \quad (4-8)$$

where: V_{wear} is the worn volume, N the normal force, d the sliding distance, and H the material hardness. The corresponding form for calculating the wear distribution can be written as:

$$h_{KTH}(x, y) = K_{KTH} \frac{p_z(x, y) \cdot \Delta d(x, y)}{H} \quad (4-9)$$

where: $h(x, y)$ is the local wear depth distribution with a subscript indicating the wear model, $p_z(x, y)$ the normal pressure distribution, and $\Delta d(x, y)$ the local sliding distance distribution. Note that the wear only occurs in the sliding zone where the traction bound is saturated and therefore the tangential stress is exactly the product of the normal pressure and the friction coefficient μ : $\tau(x, y) = \mu p_z(x, y)$ where $(x, y) \in$ sliding zone, as shown in Figure 4-2.

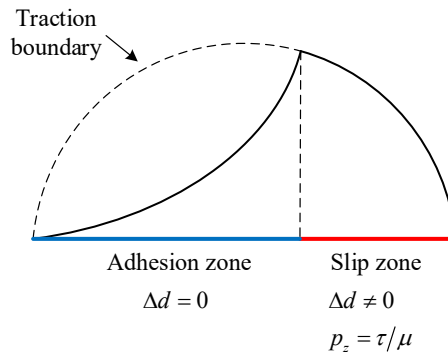


Figure 4-2 Adhesion zone and slip zone

Together with $\Delta d(x, y) = 0$ where $(x, y) \notin \text{sliding zone}$, $p_z(x, y) \cdot \Delta d(x, y)$ can be decomposed into:

$$p_z(x, y) \cdot \Delta d(x, y) = \begin{cases} \frac{\tau(x, y)}{\mu} \Delta d(x, y) & (x, y) \in \text{sliding zone} \\ 0 & (x, y) \notin \text{sliding zone} \end{cases} \quad (4-10)$$

Actually, as $\Delta d(x, y)$ can determine the sliding/adhesion zone on its own, Equation (4-10) can be recombined to a concise expression as below:

$$p_z(x, y) \cdot \Delta d(x, y) = \frac{\tau(x, y)}{\mu} \Delta d(x, y) \quad (4-11)$$

In addition, $\Delta d(x, y)$ can be further transformed through the following equation:

$$\Delta d(x, y) = s(x, y) \cdot \Delta t = V \cdot \xi(x, y) \cdot \frac{\Delta x}{V} = \xi(x, y) \cdot \Delta x \quad (4-12)$$

Where: $s(x, y)$ is the resultant sliding velocity in grid element, Δt the time passing through one grid element, Δx the longitudinal length of one grid element, and V the vehicle speed. Here $\Delta t \approx \Delta x/V$ is assumed. By substituting Equation (4-11) and (4-12) to Equation (4-10), it becomes:

$$h_{KTH}(x, y) = \frac{K_{KTH} \cdot \Delta x}{m\mu H} \cdot \tau(x, y) \xi(x, y) \quad (4-13)$$

Given $\Delta x = 2a/m$, where m is the number of longitudinal elements, Equation (4-13) becomes:

$$h_{KTH}(x, y) = \frac{2a \cdot K_{KTH}}{m\mu H} \cdot \tau(x, y) \xi(x, y) \quad (4-14)$$

If assuming $K_{KTH}^\# = \frac{2aK_{KTH}}{m\mu H}$, where $K^\#$ represents the local equivalent wear coefficient with a subscript

indicating the wear model, Equation (4-14) becomes:

$$h_{KTH}(x, y) = K_{KTH}^\# \cdot \tau(x, y) \xi(x, y) \quad (4-15)$$

The KTH wear model is based on the Archard wear model. If the Archard wear model is used globally, the critical problem is that there is no way for the spin to be accounted for in the calculation of global sliding distance. Therefore, it is only feasible for cases of small spin, which will definitely limit the application of Archard wear model in the global method. As a result, this method is not included in this chapter.

4.2.3.3 USFD model

The USFD wear model can be used both globally and locally. For the global method, the “running distance” over one contact patch should be the longitudinal contact patch length ($2a$). Correspondingly for the local method, the “running distance” over one grid element is the longitudinal element length (Δx). It is worth mentioning that the “running distance” here is different from that of the BRR wear model, which is the wheel perimeter. This is due to the different definition of these two wear functions. The calculated USFD wear is in the form of mass loss. The mass loss can be further divided by the density of the wheel material to obtain the averaged wear depth of the contact patch.

The WI of the USFD wear model is $T\gamma/A$ for the global method, and $\tau(x, y)\xi(x, y)$ for the local method. The derivation of the WI for the local method can refer to [79]. The wear rate in the global and local methods

is rewritten as below, respectively:

$$W_{USFD} = K_{USFD} \frac{T\gamma}{A} \quad (4-16)$$

$$W_{USFD}(x, y) = K_{USFD} \cdot \tau(x, y)\xi(x, y) \quad (4-17)$$

The conversion of the USFD wear model with global and local methods are given below, respectively:

$$H_{USFD} = W_{USFD} \cdot \frac{2a}{\rho} = K_{USFD} \frac{T\gamma}{\pi ab} \cdot \frac{2a}{\rho} = \frac{2K_{USFD}}{\pi b\rho} \cdot T\gamma \quad (4-18)$$

$$h_{USFD}(x, y) = W_{USFD}(x, y) \cdot \frac{\Delta x}{\rho} = K_{USFD} \cdot \tau(x, y)\xi(x, y) \cdot \frac{\Delta x}{\rho} = \frac{K_{USFD} \cdot \Delta x}{\rho} \cdot \tau(x, y)\xi(x, y) \quad (4-19)$$

Given $\Delta x = 2a/m$, Equation (4-19) becomes:

$$h_{USFD}(x, y) = \frac{2aK_{USFD}}{m\rho} \cdot \tau(x, y)\xi(x, y) \quad (4-20)$$

If assuming $K_{USFD}^* = \frac{2K_{USFD}}{\pi b\rho}$ and $K_{USFD}^\# = \frac{2aK_{USFD}}{m\rho}$, Equation (4-18) and Equation (4-20) become:

$$H_{USFD} = K_{USFD}^* \cdot T\gamma \quad (4-21)$$

$$h_{USFD}(x, y) = K_{USFD}^\# \cdot \tau(x, y)\xi(x, y) \quad (4-22)$$

4.2.3.4 Zobory model

The Zobory wear model was proposed for the local method. Professor Zobory introduced \dot{E} (stochastic energy flow density) as the WI, which is expressed as below:

$$\dot{E}(x, y) = \tau(x, y)s(x, y) \quad (4-23)$$

To save the calculation time, Professor Zobory also proposed a simplified method, which is presented below:

$$\dot{E} = \frac{|T_x v_x| + |T_y v_y| + |M\omega|}{A} \cdot \frac{p_z(x, y)}{P_z} \quad (4-24)$$

where: v_x , v_y , and ω are the global longitudinal sliding velocity, the global lateral sliding velocity, and the global angular sliding velocity, respectively; P_z is the mean normal pressure.

The simplification is to assume that the wear is distributed proportionally to the normal pressure by introducing the term $p_z(x, y)/P_z$ to Equation (4-24). However, based on the assumption of this paper, the wear distribution will eventually be averaged to get a single-value wear depth. Under this circumstance, the term $p_z(x, y)/P_z$ is actually not useful for the final result and can be just excluded from the equation. Thus a global approach based on the simplified method above can be proposed by rewriting Equation (4-24) as below:

$$\dot{E} = \frac{|T_x v_x| + |T_y v_y| + |M\omega|}{A} \quad (4-25)$$

To convert the Zobory wear model to calculate the instantaneous wear, a “running time” instead of a “running distance” is to be multiplied to the wear rate, because the WI of the Zobory wear model (\dot{E}) is a velocity-related term. The “running time” passing through one contact patch should be $dt = 2a/V$ for the global method

and $\Delta t = \Delta x/V$ for the local method, respectively. The calculated wear is in the form of mass loss. The averaged wear depth of one contact patch is then obtained with the mass loss divided by the wheel material density.

The wear rate of the Zobory wear model in global and local methods are derived as below respectively:

$$W_{Zobory} = K_{Zobory} \cdot \dot{E} = K_{Zobory} \frac{|T_x v_x| + |T_y v_y| + |M\omega|}{A} = K_{Zobory} \cdot V \cdot \frac{|T_x \gamma_x| + |T_y \gamma_y| + |M\phi|}{A} = K_{Zobory} \frac{V \cdot T\gamma}{A} \quad (4-26)$$

$$W_{Zobory}(x, y) = K_{Zobory} \cdot \dot{E}(x, y) = K_{Zobory} \cdot \tau(x, y) s(x, y) = K_{Zobory} \cdot V \cdot \tau(x, y) \xi(x, y) \quad (4-27)$$

The conversions of Zobory wear model for global and local methods are given below, respectively.

$$H_{Zobory} = W_{Zobory} \cdot \frac{dt}{\rho} = K_{Zobory} \frac{V \cdot T\gamma}{\pi ab} \cdot \frac{2a}{V} \cdot \frac{1}{\rho} = \frac{2K_{Zobory}}{\pi b \rho} \cdot T\gamma \quad (4-28)$$

$$h_{Zobory}(x, y) = W_{Zobory}(x, y) \cdot \frac{\Delta t}{\rho} = K_{Zobory} \cdot V \cdot \tau(x, y) \xi(x, y) \cdot \frac{\Delta x}{V} \cdot \frac{1}{\rho} = K_{Zobory} \cdot \tau(x, y) \xi(x, y) \cdot \frac{\Delta x}{\rho} \quad (4-29)$$

Given $\Delta x = 2a/m$, Equation (4-29) becomes:

$$h_{Zobory}(x, y) = \frac{2aK_{Zobory}}{m\rho} \cdot \tau(x, y) \xi(x, y) \quad (4-30)$$

If assuming $K_{Zobory}^* = \frac{2K_{Zobory}}{\pi b \rho}$ and $K_{Zobory}^\# = \frac{2aK_{Zobory}}{m\rho}$, Equation (4-28) and Equation (4-30) become:

$$H_{Zobory} = K_{Zobory}^* \cdot T\gamma \quad (4-31)$$

$$h_{Zobory}(x, y) = K_{Zobory}^\# \cdot \tau(x, y) \xi(x, y) \quad (4-32)$$

As can be seen from the above derivation, the vehicle speed in the original WI is effectively counteracted. By comparing Equation (4-28) with Equation (4-18), and Equation (4-30) with Equation (4-20) respectively, it can be found that the converted equations of the Zobory wear model and the USFD wear model share an identical form, with the only difference being the original wear coefficient of each model. Consequently, it is believed that the USFD wear model and the Zobory wear model possess the same nature despite the different original WI used.

4.2.4 Uniform expression of converted wear models

As a summary, all the converted equations grouped by global and local methods are listed in Table 4-2. It is interesting to see that, although the wear models in comparison are varied in their original expressions, all of them can be analytically transformed to a uniform expression. The uniform expression is $H = K^* \cdot T\gamma$ for the global method and $h(x, y) = K^\# \cdot \tau(x, y) \xi(x, y)$ for the local method. The uniform WI (variable part) is $T\gamma$ for the global method and $\tau(x, y) \xi(x, y)$ for the local method. An equivalent coefficient is derived for every wear model to represent the constant part in the uniform expression, which is denoted by K^* for global methods and $K^\#$ for local methods, with subscripts indicating the wear models. The unit of the equivalent coefficient is also uniform, which is m/N for K^* and m^3/N for $K^\#$. It has to be mentioned that, although a and b are actually variables in time history, the contribution of their variation to the variation of wear depth is

negligible compared with $T\gamma$ or $\tau(x, y)\xi(x, y)$, so that a and b are also deemed as constants to be included in the formula of equivalent coefficients, which makes the uniform expression more concise.

Table 4-2. The uniform expression of wear models converted for calculation of instantaneous wear depth

Global methods	Uniform expression	$H = K^* \cdot T\gamma$	Equivalent Coefficient K^* [m/N]
	BRR	$H_{BRR} = K_{BRR}^* \cdot T\gamma$	$K_{BRR}^* = \pi K_{BRR} / 2b$
	USFD	$H_{USFD} = K_{USFD}^* \cdot T\gamma$	$K_{USFD}^* = 2K_{USFD} / \pi b \rho$
	Zobory	$H_{Zobory} = K_{Zobory}^* \cdot T\gamma$	$K_{Zobory}^* = 2K_{Zobory} / \pi b \rho$
Local methods	Uniform expression	$h(x, y) = K^\# \cdot \tau(x, y)\xi(x, y)$	Equivalent Coefficient $K^\#$ [m ³ /N]
	KTH	$h_{KTH}(x, y) = K_{KTH}^\# \cdot \tau(x, y)\xi(x, y)$	$K_{KTH}^\# = 2aK_{KTH} / m\mu H$
	USFD	$h_{USFD}(x, y) = K_{USFD}^\# \cdot \tau(x, y)\xi(x, y)$	$K_{USFD}^\# = 2aK_{USFD} / m\rho$
	Zobory	$h_{Zobory}(x, y) = K_{Zobory}^\# \cdot \tau(x, y)\xi(x, y)$	$K_{Zobory}^\# = 2aK_{Zobory} / m\rho$
	<i>Handling wear distribution: Accumulate longitudinally and then average laterally</i>		

4.3 Comparison of wear models

The significance of Table 4-2 lies in that it allows a quantitative comparison among the wear models in the same group (either global methods or local methods). The proportional relation between each wear model can be obtained by simply comparing the equivalent coefficients (constant part) between each wear model, as the WI (variable part) is the same for all the wear models in the same group (global or local). Given a specific case and the original wear coefficients, the equivalent coefficients can be calculated to identify the ratio between each wear model. An example is presented in Table 4-3.

As can be seen from Table 4-3, the ratio of the wear depths between each wear model is precisely the same as that of the equivalent coefficients (see red and blue parts respectively). As a result, the equivalent coefficient can be employed as a useful index to quantitatively compare the wear models between each other. But the quantitative comparison is basically limited in the same group (either global or local). As for the comparison of the same wear model between global and local methods, it is unlikely to obtain a quantitative relationship due to the complexity of the contact models. The discrepancy between global and local methods for the same wear model could depend on many parameters and is complicated to explain. In spite of this, it is found that the wear depth calculated by the global method is larger than that by the local method, and their ratio is convergent with the increase of grid density. A convergence analysis of the grid density on the discrepancy of instantaneous wear depth between global and local methods is presented in Figure 4-3, with the parameters listed in Table 4-3. Here the USFD wear model is used as an example, the discrepancy between the instantaneous wear depth calculated by global and local methods is represented with their ratio, ρ , and the number of elements is the same for both longitudinal and lateral directions. As can be seen from Figure 4-3, the number

of elements should be big enough to get a convergent discrepancy between global and local methods for the same wear model. Considering the compromise of computing time, a minimum value of 50 for the number of elements is suggested.

Table 4-3 An example of calculating the converted equivalent coefficients and the instantaneous wear depths

	Parameters		Value		Parameters		Value	
	Inputs	N		122	[kN]	K_{BRR}		0.25×10^{-12}
γ_x			1.5×10^{-3}	[-]	K_{KTH}		5×10^{-4}	[-]
γ_y			0.5×10^{-3}	[-]	K_{USFD}		5.30×10^{-9}	[kg/Nm]
ϕ			0.08	[1/m]	K_{Zobory}		7×10^{-10}	[kg/Nm]
a			0.0086	[m]	V		50	[km/h]
b			0.0066	[m]	μ		0.3	[-]
ρ			7850	[kg/m ³]	H		2.94	[Gpa]
				m		51	[-]	
	Global equivalent coefficients [m/N]				Local equivalent coefficients [m ³ /N]			
Equivalent coefficients	K^*	K_{BRR}^*	K_{USFD}^*	K_{Zobory}^*	$K^\#$	$K_{KTH}^\#$	$K_{USFD}^\#$	$K_{Zobory}^\#$
	Value	6.0e-11	6.5e-11	8.6e-12	Value	1.9e-16	2.3e-16	3.0e-17
	Ratio	6.9	7.6	1.0 (ref)	Ratio	6.4	7.6	1.0 (ref)
	Global methods				Local methods			
Wear depth	Model	BRR	USFD	Zobory	Model	KTH	USFD	Zobory
	Value [m]	2.4e-9	2.6e-9	3.4e-10	Value [m]	1.6e-9	1.9e-9	2.5e-10
	Ratio [-]	6.9	7.6	1.0 (ref)	Ratio [-]	6.4	7.6	1.0 (ref)

* The Zobory wear model is the reference for the ratio calculation

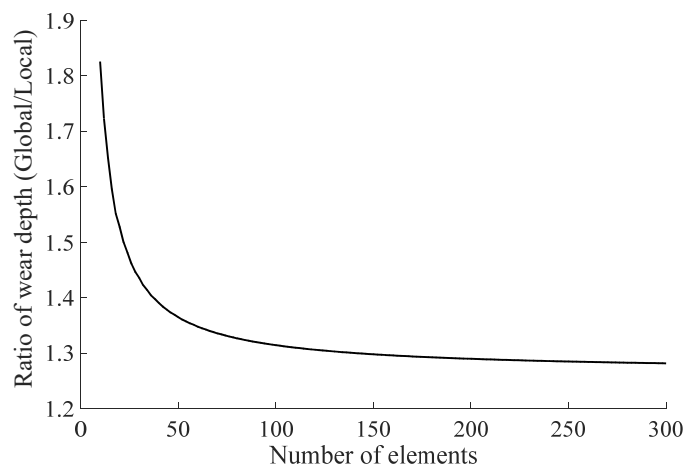


Figure 4-3 A convergence analysis of the number of elements on the ratio of wear depth (Global/Local): the USFD wear model is used in this analysis as an example

Based on the above knowledge, further comparative studies can be carried out to look at how these converted “instantaneous” wear models reflect the fluctuation of the circumferential instantaneous wear under different circumstances, and whether they behave in the same way or not. A high-axle load locomotive is used as the research object for the subsequent comparative studies. This locomotive is configured with 2 bogies, each of which consists of 2 wheelsets. The instantaneous wear depth is only calculated for the left wheel of the first wheelset. The track flexibility is simplified by positioning a sleeper underneath every wheelset. Only tangent track on which the wheel tread wear mainly occurs is taken into consideration, as the wheel polygonization is merely formed in the wheel tread without contribution from the wheel flange wear occurring on curves. Typical original wear coefficients listed in Table 4-3 for a mild wear regime occurring on a tangent track are thus adopted. The vehicle speed is set to be 70 km/h for all scenarios. The maximum frequency of interest is 300 Hz for a low-speed locomotive. Several scenarios grouped by harmonic excitation and random excitation are adopted to observe the response feature of the wear models under different types of excitation. For every scenario, a comprehensive comparison among the wear models is implemented by inspecting the fluctuation of the instantaneous wear depths in 3 aspects: fluctuation frequency, fluctuation amplitude, and fluctuation phase.

4.3.1 Under harmonic excitation

To obtain a basic understanding, two simple harmonic cases are first studied: under excitation of vertical sinusoidal track irregularity and sinusoidal initial wheel out-of-roundness (OOR), respectively. To facilitate the comparison, these two types of sinusoidal excitations are configured with the same parameters: wavelength of 1/10 wheel circumference (0.3925 m) and amplitude of 0.1 mm. Therefore, the only excitation frequency is around 50 Hz at a speed of 70 km/h. This frequency is expected to be distinguished by the wear models. The simulation results are shown in Figure 4-4 and Figure 4-5, respectively, with 3 sub-graphs showing the time history, the frequency spectrum, and the zoomed details demonstrating the fluctuation amplitude and phase.

4.3.1.1 Vertical sinusoidal track irregularity

As can be seen from Figure 4-4 (a), the time history of the instantaneous wear depths calculated by different wear models is presented in a comparable sense. The difference in the mean value of the instantaneous wear depth between each wear model is mainly determined by the original wear coefficients of each wear model, which has been discussed previously. A more interesting aspect here is the fluctuation of the instantaneous wear depth. It can be seen from Figure 4-4 (b) that, all the wear models can correctly reflect the excitation frequency that is 50 Hz in this case. Figure 4-4 (c) further shows the amplitude and phase of the fluctuation of the instantaneous wear depths with the mean values subtracted. To make the wear fluctuation phase observable, the abscissa is zoomed in one period of fluctuations with the wheel circumferential angle as the x-coordinate. To compare the wear fluctuation amplitude conveniently, the y-coordinate is replaced by the normalized amplitudes of the wear fluctuations, where the Local Zobory wear model with the smallest wear fluctuation is the reference and has a normalized fluctuation amplitude of 1. As can be seen in Figure 4-4 (c), the wear fluctuation phase is the same for the same group (either global or local wear models), only with a tiny difference between global and local groups. The ratio of the wear fluctuation amplitude among all the wear models is

almost the same as that of the mean value. This can be checked in Table 4-4.

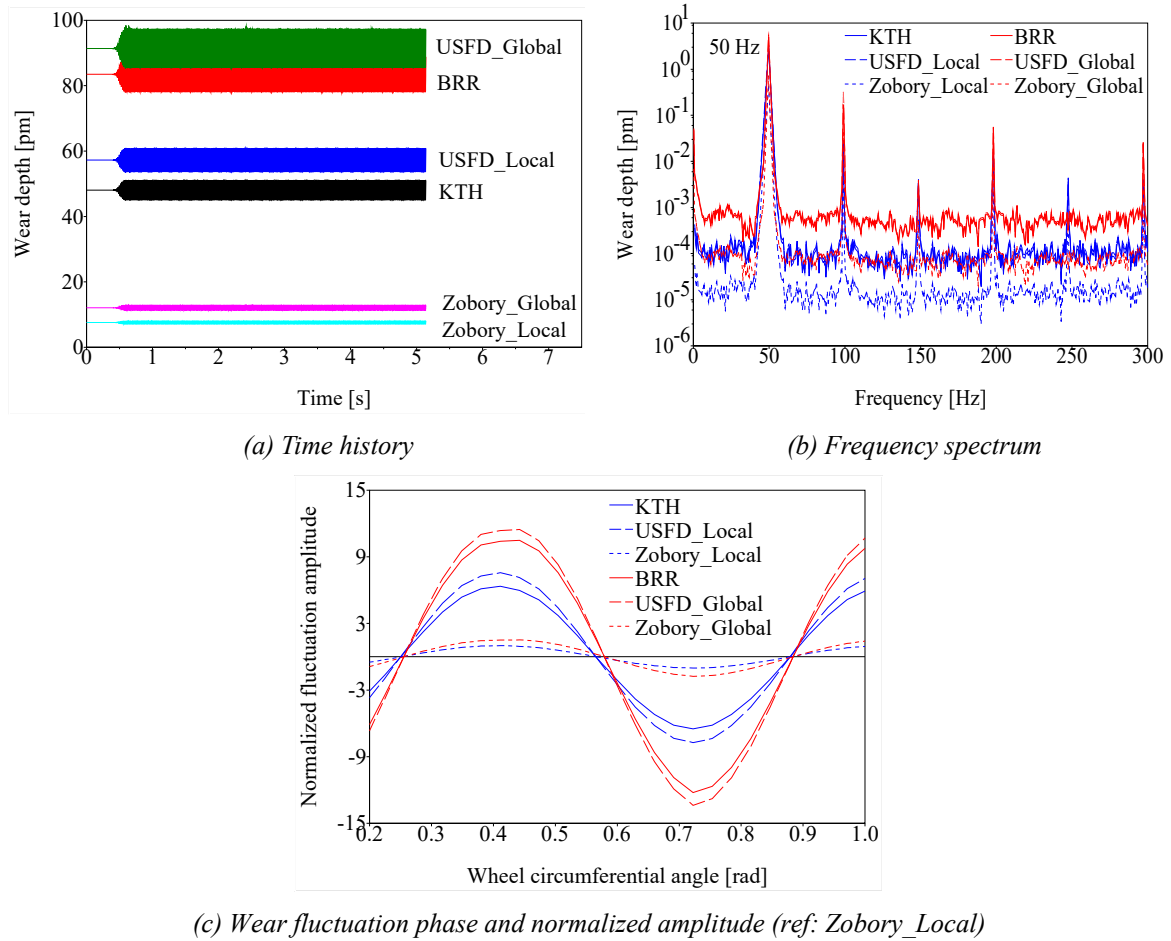


Figure 4-4 Comparison of instantaneous wear depths among the wear models under excitation of a sinusoidal vertical track irregularity: (a) Time history, (b) Frequency spectrum, (c) Wear fluctuation phase and normalized amplitude (ref: Zobory_Local)

Table 4-4 A comparison between the ratio of the mean value and the ratio of fluctuation amplitude

	Model	BRR	USFD Global	Zobory Global	KTH	USFD Local	Zobory Local
Ratio	Mean value	11.04	12.10	1.60	6.36	7.58	1.00
	Fluctuation	10.60	11.61	1.53	6.36	7.58	1.00

* The Local Zobory wear model is the reference for the ratio calculation

4.3.1.2 Sinusoidal initial OOR

Figure 4-5 shows the results excited by a sinusoidal initial OOR. The primary feature is similar compared to the case of track irregularity. The excitation frequency can also be reflected correctly by all the wear models. But the multiple frequency components are more notable due to the cyclic revolution of the wheels, as shown in Figure 4-5 (b). However, some sharp points are found in the curves of all global methods in Figure 4-5 (c), which is unreasonable. This can be explained by the following.

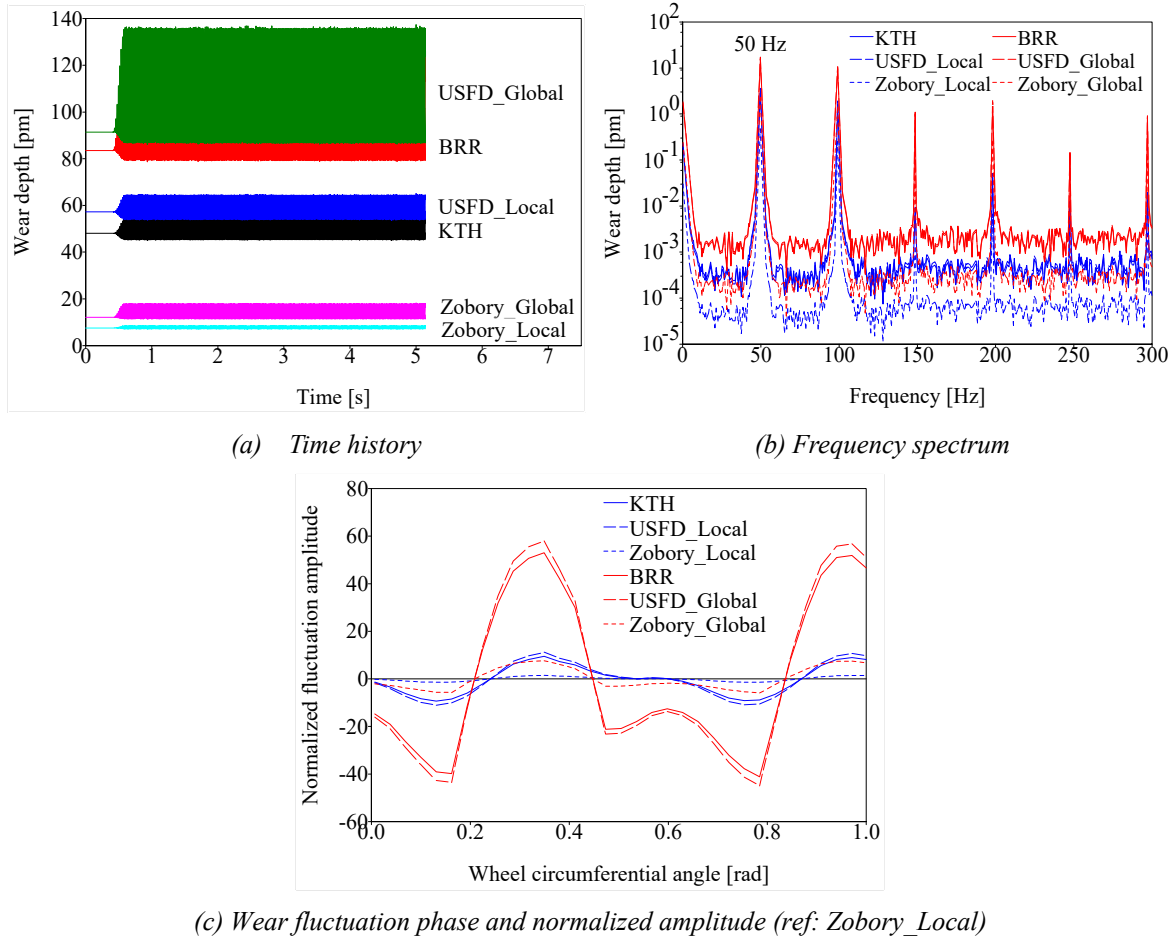


Figure 4-5 Comparison of instantaneous wear depths among the wear models under excitation of a sinusoidal initial OOR: (a) Time history, (b) Frequency spectrum, (c) Wear fluctuation phase and normalized amplitude (ref: Zobory_Local)

The global WI is $T\gamma$ consisting of three components representing the wear works in three coordinates, which is rewritten as below. Note that an absolute operation is required for each component as negative frictional work is meaningless.

$$T\gamma = |T_x\gamma_x| + |T_y\gamma_y| + |M\phi| \quad (4-33)$$

Under excitation with a single frequency, all the contact responses must share the same frequency component. If viewing every contact response as a sinusoidal curve mathematically, each component $T\gamma$ comes down to a product of two sinusoidal curves with the same frequency. Note that any single sinusoidal curves can be expressed as a universal formula below:

$$F(t) = \bar{M} + \tilde{A} \cdot \sin(ft + \theta) \quad (4-34)$$

where \bar{M} is the mean value, \tilde{A} is the amplitude of variation, f is the frequency, θ is the phase shift.

The product of two sinusoidal curves with the same frequency can be derived as follows:

$$\begin{aligned}
F_1(t)F_2(t) &= \left[\bar{M}_1 + \tilde{A}_1 \cdot \sin(ft + \theta_1) \right] \left[\bar{M}_2 + \tilde{A}_2 \cdot \sin(ft + \theta_2) \right] \\
&= \bar{M}_1 \bar{M}_2 + \tilde{A}_1 \tilde{A}_2 \cos(\theta_1 - \theta_2) \\
&\quad + \sqrt{(\bar{M}_1 \tilde{A}_2 \cos \theta_2 + \bar{M}_2 \tilde{A}_1 \cos \theta_1)^2 + (\bar{M}_1 \tilde{A}_2 \sin \theta_2 + \bar{M}_2 \tilde{A}_1 \sin \theta_1)^2} \cdot \sin(ft + \arctan \frac{\bar{M}_1 \tilde{A}_2 \sin \theta_2 + \bar{M}_2 \tilde{A}_1 \sin \theta_1}{\bar{M}_1 \tilde{A}_2 \cos \theta_2 + \bar{M}_2 \tilde{A}_1 \cos \theta_1}) \\
&\quad - \frac{\tilde{A}_1 \tilde{A}_2}{2} \cos(2ft + \theta_1 + \theta_2)
\end{aligned} \tag{4-35}$$

In Equation (4-35), there are three individual parts: mean value, sinusoidal fluctuation (f), and sinusoidal fluctuation ($2f$). Obviously, if $F_1(t)F_2(t)$ is constantly positive, an absolute operation will have no effect on the result. But if $F_1(t)F_2(t)$ is not constantly positive, which must be attributable to the fluctuation parts, some sharp points will be produced by the absolute operation. However, whether these sharp points could be notable in the final result of T_γ depends on the combination of the contact parameters in specific cases, which is a complicated mathematical issue. The mean value of the contact responses, the fluctuation amplitude, and the phase between contact parameters can all influence the results. Figure 4-6 shows the phase relations of contact responses excited by track irregularity and initial OOR, respectively, which presents a significant difference between each other. This could be one of the reasons why the sharp points appear obviously in the curves of global methods for the case of initial OOR, while not for the case of track irregularity. Unfortunately, it is not clear as for why and how the phase relation of the contact responses are formed under different scenarios.

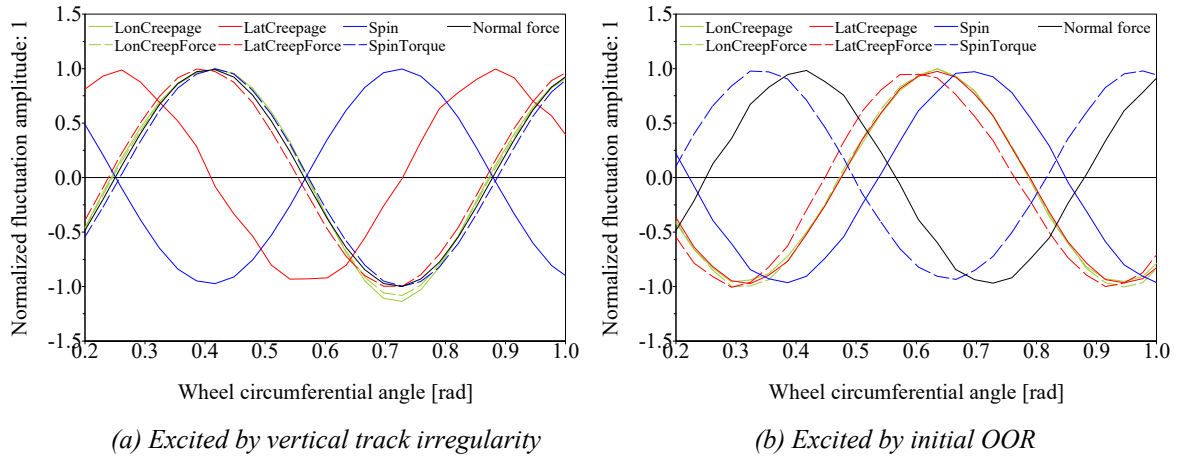


Figure 4-6 Phase difference between contact responses: (a) Excited by vertical track irregularity, (b) Excited by initial OOR. The fluctuation amplitude of all curves is normalized to 1 to facilitate the comparison of phase between curves.

4.3.2 Under random excitation

Based on the understanding obtained from the case of harmonic excitation, two scenarios of random excitations are further investigated: standard track irregularity and measured polygonal wear.

4.3.2.1 Standard track irregularity

An essential aspect in the prediction of railway wheel polygonization is to identify the predominant resonant frequencies of the instantaneous wear in the vehicle/track dynamic system. A standard track irregularity

spectrum FRA 6 (the 6th class track defined by Federal Railroad Administration of US) [67] is adopted to investigate the responses of wear models under excitation of realistic random track irregularities. In reality, the main energy of the random track irregularity is normally distributed in long wavelengths corresponding to low time frequencies (below 12 Hz at a speed of 70 km/h in this case). The simulation results are presented in Figure 4-7.

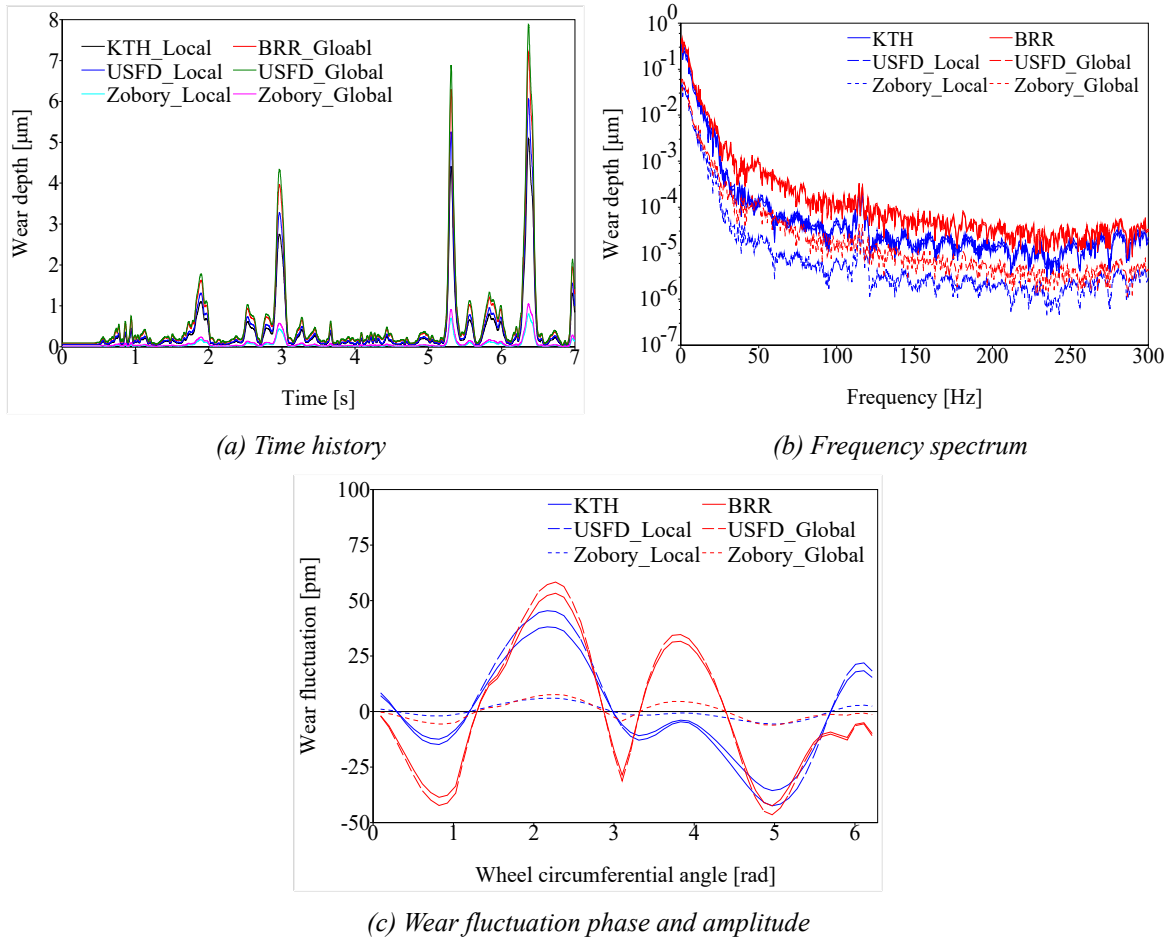


Figure 4-7 Comparison of instantaneous wear depths among the wear models under excitation of random track irregularity (FRA 6): (a) Time history, (b) Frequency spectrum, (c) Wear fluctuation phase and amplitude

As can be seen from Figure 4-7 (a) and (b), the calculated instantaneous wear depths are still comparable between each wear model. The energy concentrated upon the lower frequencies is correctly reflected by all the wear models. Note that the wear excited by a random track irregularity spectrum is much larger than other cases. Although some abrupt wear depths can be found in the time history, it will not produce unrealistic results for the final polygonal wear, because for a random case, a long enough sample must be adopted and then averaged for many revolutions, so that the abrupt peaks will be eliminated. When looking at Figure 4-7 (c), some sharp points are still present in the curves of global methods.

4.3.2.2 Measured polygonal wear

In reality, the railway wheel polygonization is gradually formed not only by the track excitation, but also due to the polygonal wear itself. The measured polygonal wear is adopted to investigate the responses of the wear

models under the excitation of realistic initial polygonal wear. Figure 4-8 shows the measured polygonal wear of eight wheels of the locomotive, with the average value indicated by a red line. More details with respect to the statistical measurement can be found in [30]. These measured polygonal wear are assigned to each wheel, respectively. The simulation results are shown in Figure 4-9. A dominant feature in Figure 4-9 (b) is the notable multiple frequency components. The interval of these multiple frequency components is exactly the rolling frequency of the wheels, which is around 5 Hz in this case. This is due to the cyclic excitation by the polygonal wear itself. Despite this, all wear models present similar features of the instantaneous wear depths only except that some sharp points persist in the curves of global methods.

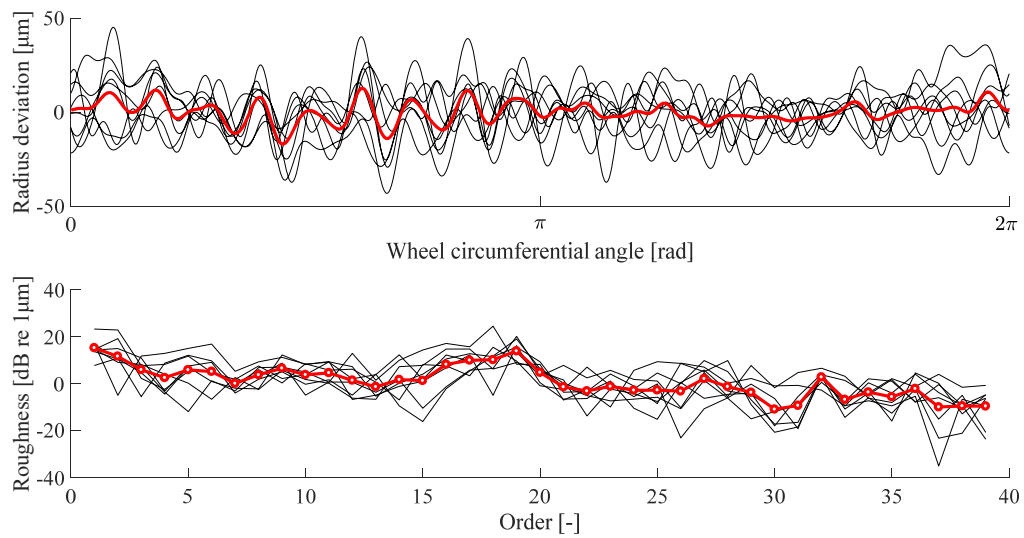
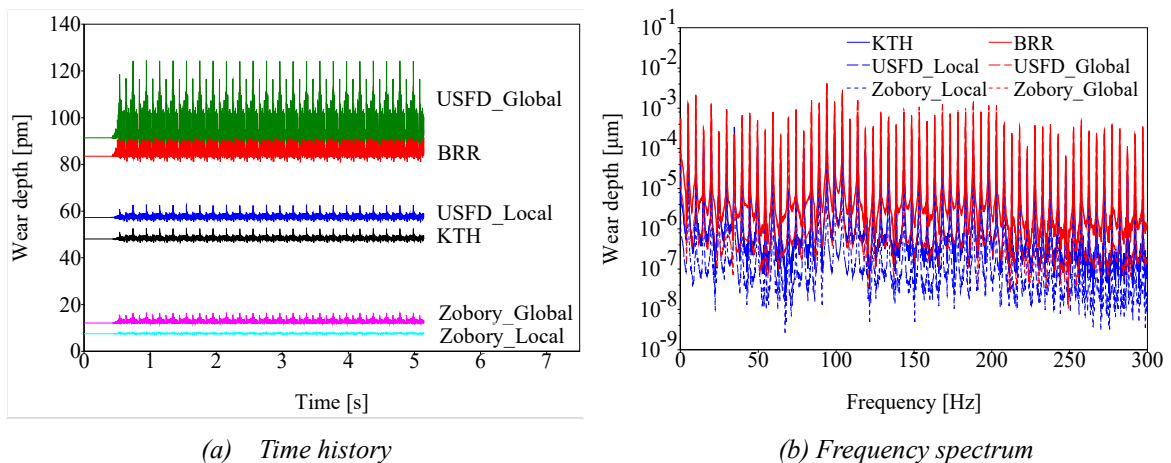
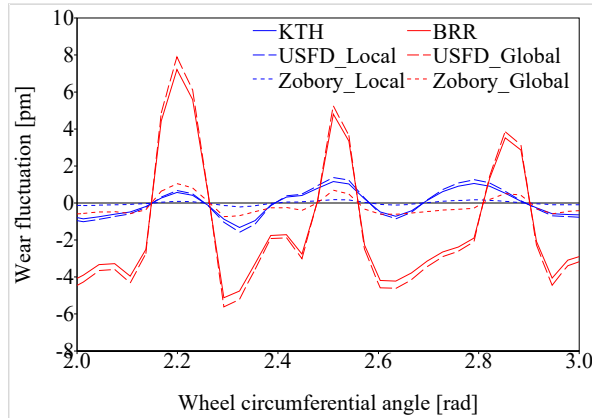


Figure 4-8 Measured polygonal wear of a locomotive, with black lines indicating eight wheels and the red line indicating the averaged value



(a) Time history

(b) Frequency spectrum



(c) Wear fluctuation phase and normalized amplitude (ref: Zobory_Local)

Figure 4-9 Comparison of instantaneous wear depths among the wear models under excitation of Measured initial wheel polygonization: (a) Time history, (b) Frequency spectrum, (c) Wear fluctuation phase and normalized amplitude (ref: Zobory_Local)

4.3.3 Evolution of polygonal wear

The prediction program in Chapter 3 is applied to predict the wheel polygonization in order to evaluate the evolved polygonal wear around the wheel circumference under two circumstances: sinusoidal excitation and white noise, with a concentration on the comparison between each wear model. For consistency, all the model parameters, as well as the original wear coefficients, are set the same as in the above sections. The number of iterations is set to 10 with an amplification coefficient of $1e6$ for each iteration. So the corresponding total running distance is 39,250 km. The final evolution of the polygonal wear using different wear models is presented in Figure 4-10 and Figure 4-11 for two scenarios, respectively.

4.3.3.1 Under the excitation of sinusoidal vertical track irregularity

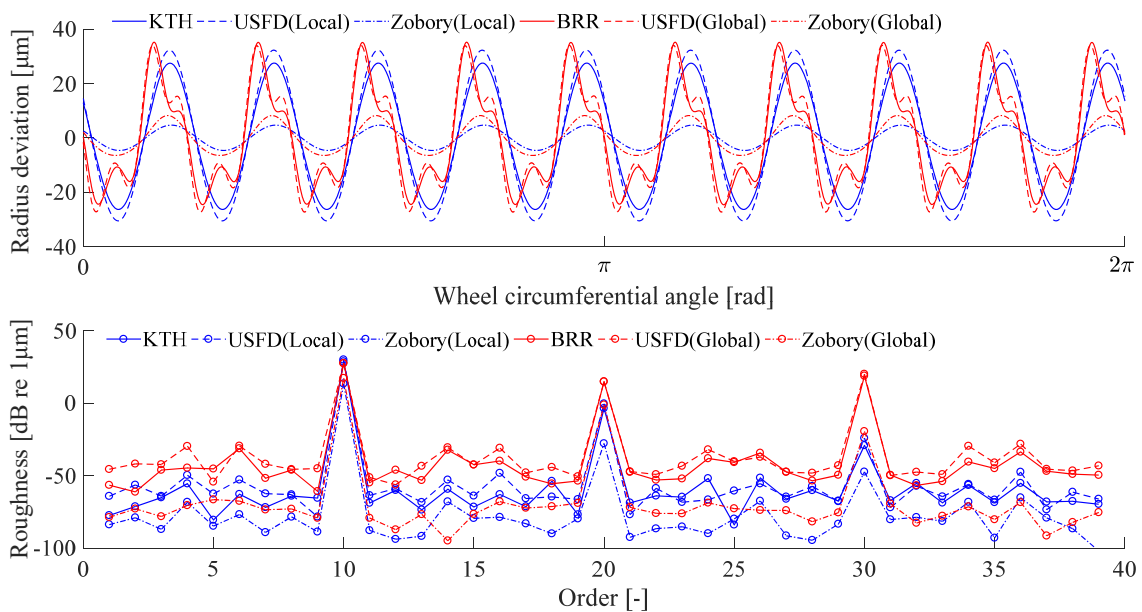


Figure 4-10 Evolution of polygonal wear under excitation of sinusoidal vertical track irregularity

As can be seen from Figure 4-10, all the wear models exhibit the dominantly developed order of 10, which corresponds to the excitation frequency of 50 Hz at a speed of 70 km/h. The growth rate of the wheel roughness depends on the original wear coefficients used in each wear model. With a close look at the local wear models (blue curves), the evolved radius deviations are exactly in phase, and there is a good consistency of trend that the multiple frequency components are gradually attenuated. However, in terms of global methods (red curves), the situation is relatively complicated. Note that the excitation of vertical sinusoidal track irregularity itself will not produce distinct sharp points in the global instantaneous wear (see Figure 4-4 (c)), but the newly developed polygonal wear during iterations will (see Figure 4-5 (c)). Meanwhile, the evolution program will have to smooth the polygonal wear curves between iterations to guarantee a stable successive simulation. When the newly developed polygonal wear becomes large enough, some sharp points will be generated but will be smoothed as well. If the evolved radius deviation is big (BRR and USFD (Global)), the smoothing effect for those sharp points can be traced easily, while if not (Zobory (Global)), the smoothing effect cannot be observed easily. In addition, for the largely evolved radius deviation (BRR and USFD (Global)), the multiple frequency components are not gradually attenuated due to the smoothing effect.

In addition, another aspect of interest is the proportional relationship of the evolved wheel roughness between each wear model. The ratio of the final wheel roughness of the 10th order between each wear model is compared with that of the mean value of the instantaneous wear depth for the first run, which is listed in Table 4-5. As can be seen from Table 4-5, the proportional relationship persists through the iterations for all wear models except BRR and USFD (Global). The change of BRR and USFD (Global) in the proportional relationship is due to the smoothing effect for those sharp points. The slight change of the local wear models in the proportional relationship is attributable to the iterations in which newly evolved polygonal wear are always introduced for the next run. Remember that the ratio of the mean value of the instantaneous wear depth between each wear model is determined by the equivalent coefficients (see Section 4.3.1.1). This is to say the equivalent coefficients can also be employed to estimate the proportional relationship of the final evolved wheel roughness among the wear models.

Table 4-5 A comparison between the ratio of the mean value and the ratio of fluctuation amplitude

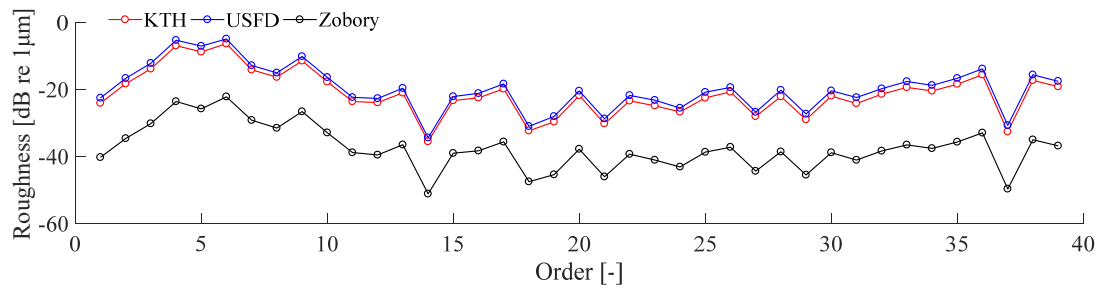
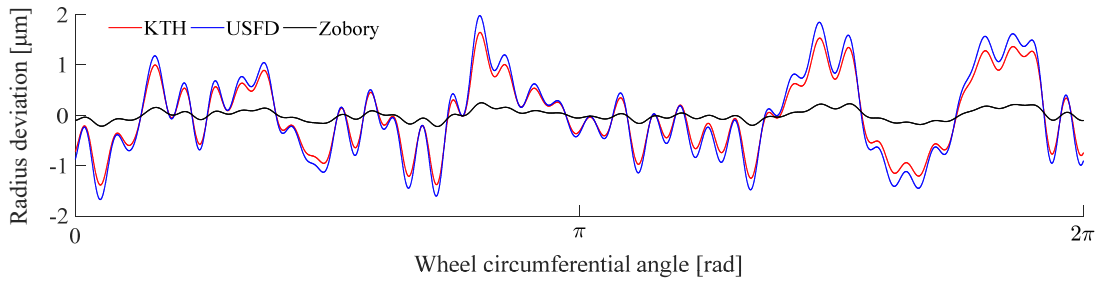
	Model	BRR	USFD Global	Zobory Global	KTH	USFD Local	Zobory Local
Ratio	Mean value (first run)	11.04	12.10	1.60	6.36	7.58	1.00
	Wheel roughness (final result)	5.00	5.10	1.56	5.79	6.75	1.00

** The Local Zobory wear model is the reference for the ratio calculation*

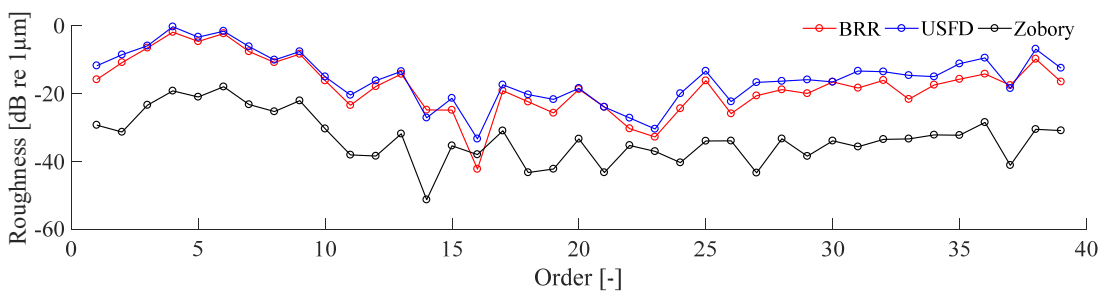
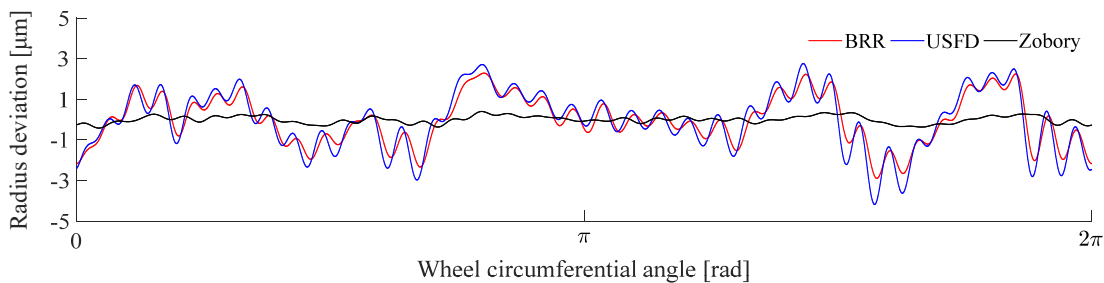
4.3.3.2 Under the excitation of equal-energy-distributed white noise

Under the excitation of the equal-energy-distributed white noise, the evolved wheel roughness with global methods and local methods are displayed separately in Figure 4-11 to facilitate the observation. More details about the equal-energy-distributed white noise will be elaborated in Section 6.5.2. First of all, the 6th order should develop dominantly according to the main resonant frequency of around 30 Hz at a speed of 70 km/h in this case. This is distinguished by all the wear models successfully. Having a close look at Figure 4-11 (a),

all local wear models present an excellent consistency in simulating the polygonal wear around the wheel circumference after a long-distance of running under excitation of white noise. However, on the contrary, the global methods do not show perfect consistency between each other, as shown in Figure 4-11 (b). This is also due to the smoothing effect on the curves with sharp points, by which some artificial errors may have been introduced.



(a) Local methods



(b) Global methods

Figure 4-11 Evolution of polygonal wear under excitation of equal-energy-distributed white noise: (a) Local methods; (b) Global methods

4.4 Discussion

4.4.1 About the sharp points

As can be seen in Section 4.3, some sharp points are always notable in the instantaneous wear depth calculated by global methods for most scenarios. It is due to the absolute operation for the global WI $T\gamma$, which has been explained in Section 4.3.1.2. This situation will not happen for local methods that avoid absolute operation. Although the square operation for the local WI $\tau(x,y)\xi(x,y)$ (see Equation (4-2)) might produce sharp points for one element wear, the average of the meshed wear distribution is always able to smooth some potential sharp points. In addition, although the sharp points generated by global methods are possible to be smoothed with some smoothing methods, it takes the risk of causing artificial errors in the results. Therefore, it is naturally believed that the global method is not suitable for calculating the instantaneous wear, although it could reduce some computing time, and the local method is recommended.

4.4.2 About the assumptions

When studying wear in the transverse wheel profile, the circumferential wheel profile was always assumed unaltered [71,75,77,79,82-87]. Similarly, the transverse wheel profile is assumed not changed in this dissertation to concentrate on the wheel polygonization, which is also supported by the statistical measurement [13,30]. Based on this assumption, the instantaneous wear of one contact patch is further assumed to be equally distributed in the wheel transversal profile. That is to say, the instantaneous wear is averaged to get the final wear depth. However, an alternative way of handling the wear distribution is adopting the maximum wear value of the transversal wear curve as the final result, for example, see Johansson [14]. A comparative study has been conducted here to check the difference between these two methods (“average method” and “maximum method”). It turns out that the shape of the calculated circumferential wear is rather similar for most scenarios, but with a difference being the fluctuation amplitude which is the critical parameter for the growth rate. Despite this, it is believed that the “average method” is preferable to the “maximum method” as the “average method” conforms to the assumption better. Moreover, the uniform expression for local wear models can only be analytically derived based on the “average method”.

In addition, the contact model is assumed to use Hertz theory for normal contact and FASTSIM for tangential contact. This is the most common combination adopted for wheel/rail contact calculation. If other contact models are used, the conversion of the wear models might have to be adjusted accordingly. However, it is still believed that the uniform wear functions together with the equivalent coefficients derived in this chapter can reflect the essential nature and the proportional relationship among the wear models in a general sense.

4.4.3 About the local Wear Index

The local Wear Index (WI) $\tau(x,y)\xi(x,y)$ of one grid element is defined as the product of the resultant tangential stress and the resultant local creepage. From a mathematical point of view, this is a product of two

vectors that have the same direction. However, two different methods are available in the academic community, which are listed below:

$$\text{Method 1: } \tau(x, y)\xi(x, y) = \sqrt{\tau_x^2(x, y) + \tau_y^2(x, y)} \cdot \sqrt{\xi_x^2(x, y) + \xi_y^2(x, y)} \quad (4-36)$$

$$\text{Method 2: } \tau(x, y)\xi(x, y) = \tau_x(x, y)\xi_x(x, y) + \tau_y(x, y)\xi_y(x, y) \quad (4-37)$$

In the original paper written by Professor Zobory [71], although the expression of $\tau(x, y)\xi(x, y)$ is given by Method 2, the calculation of it is actually according to Method 1, which can be checked in the Equation (20) in reference [71]. In addition, the Archard wear model upon which the KTH wear model is based essentially uses Method 1 to calculate its original global WI Nd which can also be converted to $\tau(x, y)\xi(x, y)$ (see Section 4.2.3.2). As the local WI $\tau(x, y)\xi(x, y)$ represents the frictional work that is not a vector but a scalar, it is believed that Method 1 is the preferable one. Obviously, the result calculated by Method 2 will be slightly smaller than that by Method 1. In addition, as $\tau(x, y)$ and $\xi(x, y)$ share the same direction, an absolute operation in Method 2 is actually not necessary.

4.5 Summary

To sum up, this chapter has obtained an improved understanding of the applicability of the existing popular wear models for simulation of railway wheel polygonization by carrying out a comprehensive comparative study between four representative wear models developed by BRR, KTH, USFD, and Professor Zobory respectively. Although the wear models investigated in this chapter are different from each other in their original definition, they actually share the same nature in calculating the instantaneous wear depth, as all of them can be analytically converted into a uniform expression with a uniform Wear Index (WI), although the WI is different in the form for global and local methods. The derived equivalent wear coefficient is a useful index to quantitatively identify the proportional relationship among the wear models in many aspects: the mean value of the instantaneous wear depth, the fluctuation amplitude of the instantaneous wear depth, and the roughness level of the evolved polygonal wear.

Several scenarios grouped by harmonic excitation and random excitation are adopted to assess the fluctuation of the instantaneous wear depth calculated by different wear models. The evolved polygonal wear around the wheel circumference is also compared among the wear models based on a developed prediction program. Simulation results show that all the wear models being investigated in this chapter present a similar ability to reflect the fluctuation of the instantaneous wear under various circumstances. Precisely, all wear models can correctly reflect the frequency characteristics of the excitation in a general sense, and the fluctuation phase of the instantaneous wear is obtained with almost the same result among the wear models. There is a perfect consistency of trend for all local wear models to simulate the evolved polygonal wear. The mean value and the fluctuation amplitude of the instantaneous wear, as well as the roughness level of the evolved polygonal wear, are all determined by the original wear coefficients used. Besides, it is believed that the global method is not suitable for calculating the polygonal wear of railway wheels as some sharp points are easily generated in the time history of instantaneous wear depth due to the absolute operation for the global WI, and thus the local method is recommended.

As all the wear models in the comparison share the same converted expression, the selection from among these wear models does not matter significantly, but the wear coefficient adopted is the key to obtain a meaningful result for a real case. The wear coefficient suitable for predicting the wheel circumferential profile change, which could be very different from the case of transverse profile prediction, may have to be calibrated either by fundamental experiments of wheel polygonal wear in a laboratory or by tracking measurement of wheel circumferential profile on site. In addition, if plastic deformation, which is generally neglected in wheel polygonal wear study, were found essential to form the polygonal shape of the wheels, a plastic wear model may have to be introduced. Despite the success achieved in the transverse wheel profile prediction using existing wear models, a robust prediction of railway wheel polygonization with current wear models is still on the way.

Chapter 5 Effects of railway wheel polygonization

5.1 Introduction

Railway wheel polygonization has been recognized as a harmful driver of the abnormal vibration of the vehicle-track dynamic system [16,18]. It introduces periodic vibration to the wheel-rail interface, causing forced oscillation to the vehicle components and track foundation. If the wheel polygonization has reached a high-level, the dynamic performance of the vehicle-track system can be severely damaged, so that the wheel re-profiling must be implemented to eliminate the wheel OOR. The associated substantially higher maintenance costs have been a primary motivation for studies leading to a better understanding of wheel polygonization effects and identifications of appropriate countermeasures to limit the growth of wheel OOR.

Some Chinese electric locomotives running on freight lines suffered from wheel polygonization. To quantify the effect, a tracking test on an electric locomotive was carried out by CRRC Zhuzhou Locomotive Company and Southwest Jiaotong University cooperatively since 2014. In this chapter, this tracking test is introduced after illustrating the method of OOR data analysis as fundamental knowledge. Afterwards, a comparison is carried out between the simulation and the measurement. Based on the simulation model, parameter analysis is performed to identify the effect of wheel polygonization on the dynamic performance of the vehicle quantitatively. Finally, some general rules in terms of the effect of railway wheel polygonization on the vehicle are derived.

5.2 OOR data analysis

The first standard specifically for the measurement of wheel roughness was introduced in May 2019 when BS EN 15610:2019 (Railway applications-Acoustics-Rail and wheel roughness measurement related to noise generation) [88] was published. According to this new standard, before calculating the wavelength spectrum, the original measurement data of wheel roughness shall be processed in three stages, namely spike removal, curvature processing, and endpoint detrending. They are briefly interpreted as follows:

(1) Spike removal: to remove narrow upward spikes that are regarded as being associated with the presence of small particles of foreign matter on the wheel surface and are therefore not representative of the real surface geometry. The spike is identified by the criteria $d^2r/dx^2 > -10^7 \mu\text{m}/\text{m}^2$ and a change of sign for dr/dx , where x is the distance around the wheel circumference and $r(x)$ is the roughness. Note that only the spikes are required to be removed according to the standard, while pits that cannot be the result of small particles should not be modified. The difference between spikes and pits can be checked with Figure 5-1, where 1 is a spike, and 2 is a pit. Should the pits be removed as well, the criterion can be changed to $|d^2r/dx^2| > 10^7 \mu\text{m}/\text{m}^2$.

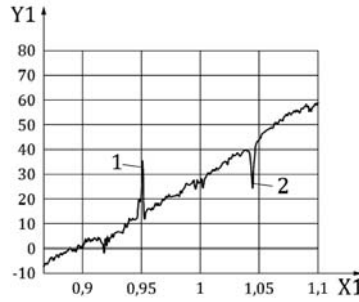


Figure 5-1 Spike removal: 1 spike, 2 pit [88]

(2) Curvature processing: to take account of the effect of the small radius of the sensor tip compared to that of the wheel. For each roughness data point x_i from the $r(x)$ roughness function, a circular curve $C_i(x)$ with a radius equal to that of the measured wheel, R , is defined passing through the data point $r(x_i)$, with its centre located at x_i above the $r(x)$ function. The corrected roughness at the roughness data point x_i is taken as $r'(x_i)$ according to Equation (5-1).

$$r'(x_i) = \max \left[\left(R + r(x) \cos\left(\frac{x - x_i}{R}\right) \right) - R \right] \quad (5-1)$$

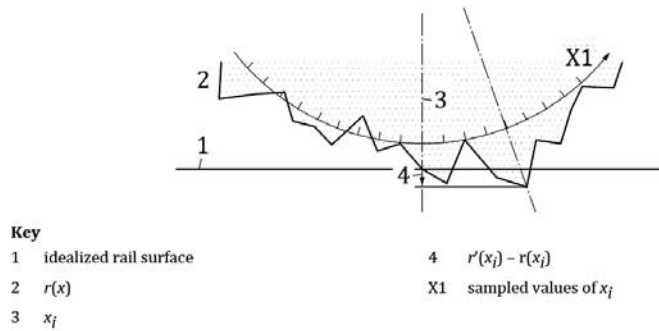


Figure 5-2 Curvature processing principle [88]

(3) Endpoint detrending: a straight line through the first and the last record is subtracted from the measurement data to ensure continuity through the end measurement points.

The aim of the above three steps is to eliminate some artificial errors during the measurement by ‘smoothing’ the roughness curve and ensuring the overlap of the start point over the endpoint. Note that EN 15610:2019 is standing in the perspective of noise-related issues. However, from the point of wheel OOR prediction that involves iterative processes in the simulation, the OOR curve processed according to EN 15610:2019 is not always sufficiently ‘smooth’, even when the pits in addition to the spikes are removed as well. Moreover, the OOR profile, as a closed curve, should be continuous at the endpoints not only in geometrical sense but also in differentiable sense to avoid unrealistic periodic shocks at the endpoints during wheel rolling. In addition, higher frequencies that are either not of interest or artificial should be filtered. As a result, the wheel OOR curve should be further processed in terms of the smoothness and the continuity in addition to EN 15610:2019. Traditional curve smoothing methods cannot ensure a closed curve to be continuous and differentiable at the endpoints. A modified Fourier filter method is developed to do the further processing for wheel OOR curve. The method can be divided into the following steps:

- Step 1: Replicate the OOR data three times in x-coordinate (the wheel circumferential angle).
 Step 2: Apply the Fourier transform to the whole curve.
 Step 3: Specify the upper frequency to be filtered.
 Step 4: Apply the inverse Fourier transform.
 Step 5: Take the middle part of the entire curve.

This method is simple, but efficient. It can ensure that the OOR curve is continuous and differentiable at the ends when the OOR curve is replicated cyclically in the x-coordinate. Moreover, the OOR curve can be smoothed and filtered to exclude high frequencies at the same time. An example is presented in Figure 5-3. To facilitate the comparison, the blue curve is shifted down by 50 μm , and the red curve is shifted down by 100 μm . As can be seen in Figure 5-3, the OOR curve is not sufficiently smooth after applying EN 15610:2019 (blue curve), but can be well smoothed after applying the modified Fourier filter method (red curve). Most importantly, the endpoints of the OOR curve become continuous and differentiable, as the dashed red circles show.

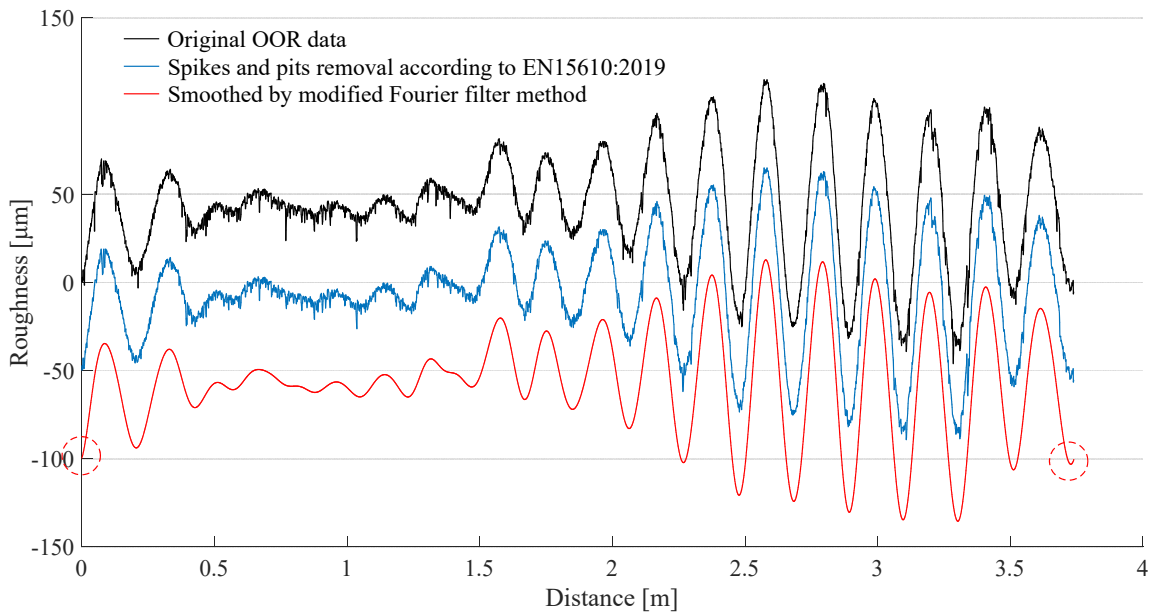


Figure 5-3 Comparison of wheel OOR curve smoothing

After processing the original OOR data, the OOR profile shall be represented graphically in one-third octave bands, with the roughness level as a function of wavelength. The one-third octave band spectrum is synthesized from a corresponding narrowband spectrum. The level in one-third octave band k shall be calculated using Equation (5-2).

$$L_k = 10 \log_{10} \left[\frac{\gamma_1}{\gamma} S_1 + \sum_{j=2}^{n_k-1} S_j + \frac{\gamma_{n_k}}{\gamma} S_{n_k} \right] \quad (5-2)$$

where γ_1 and γ_{n_k} are the portions of the narrow bands to be taken into account at the one-third octave band boundaries, n_k is the number of the narrow frequency bands having an energy contribution within the 1/3 octave band of index k , S_j is the auto spectrum in the narrow band of index j ($j=1 \sim n_k$), γ is the narrow bandwidth

obtained from the DFT analysis.

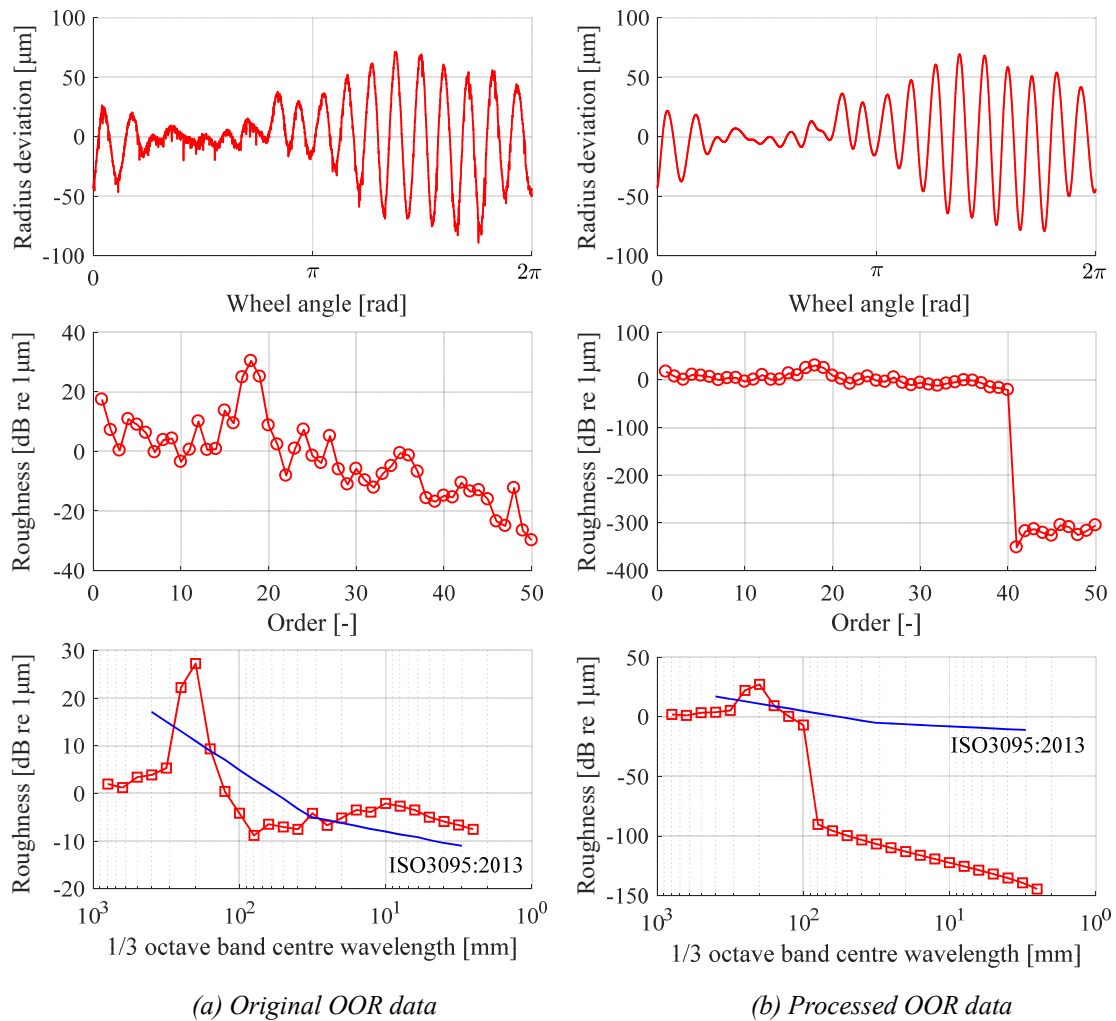


Figure 5-4 OOR presentation in the form of radius deviation, order spectrum, and 1/3 octave band spectrum. (a) The original OOR data, (b) The OOR data processed by the modified Fourier filter method with the maximum order of 40

The one-third octave band spectrum analysis is necessary for rail roughness assessment as there is a limit spectrum specified in ISO 3095 [89]. However, there is no such a limit spectrum for wheel roughness, so usually, the limit curve for rail roughness in the one-third octave band spectrum is used as an alternative reference for wheel roughness assessment. Another form to demonstrate the OOR roughness is the order spectrum with which the wheel roughness level against the orders (the number of edges of the wheel ‘polygon’) can be observed directly. The roughness level in the order spectrum is calculated according to Equation (5-3).

$$L_i = 20 \log_{10}(r_i) \quad (5-3)$$

where L_i is the acoustic roughness level in [dB re 1 μm] for the i^{th} order, and r_i is the magnitude of the frequency spectrum in μm for the i^{th} order. The maximum wavelength of the OOR data is the wheel circumference corresponding to the 1st order. However, the minimum wavelength corresponding to the highest order is specified according to the maximum frequency considered in the simulation, which is scenario dependent. The relationship between the OOR order, the OOR wavelength, and the corresponding excitation frequency at a

given speed is shown in Equation (5-4).

$$f = \frac{V}{\lambda} = \frac{V}{C/O} = \frac{V \cdot O}{C} \quad (5-4)$$

where: V is the wheel running speed, O the OOR order, C the wheel circumference, λ the OOR wavelength, and f the excitation frequency of OOR. Generally, the maximum order considered corresponds to the maximum frequency of interest. For instance, for a high axle-load locomotive whose maximum operating speed is 120 km/h and whose wheel circumference is 3.925 m, the maximum order is 40 roughly corresponding to 300 Hz at 120 km/h, and the minimum wavelength is therefore around 100 mm. As an example, the OOR data in the form of radius deviation, order spectrum, and 1/3 octave band spectrum are presented in Figure 5-4, with a comparison between OOR data before and after processing. As can be seen in Figure 5-4, the orders above 40 and the wavelength below 100 mm are filtered with the modified Fourier filter method. The blue line in the 1/3 octave band spectrum is the limit spectrum for rail roughness specified in ISO 3095:2013, only serving as an alternative reference here as there has not been a specific spectrum limit for wheel roughness. Note that the spectrum limit in ISO 3095:2013 is slightly lower than that in ISO 3095:2005.

5.3 Tracking test

5.3.1 Measurement scheme

A long-term tracking test for an electric locomotive was undertaken by the CRRC Zhuzhou Locomotive Company in cooperation with Southwest Jiaotong University, aiming to investigate the influence of wheel OOR on the vehicle. This tracking test involves the measurement of wheel OOR profiles and the vibration of vehicle components immediately before and after the wheel re-profiling. The measurements were undertaken four times, as shown in Table 5-1.

Table 5-1 Tracking test of wheel OOR profile and vibration test

Tracking test	Measurement date (y-m-d)	Running distance	Vibration test
1	2014-12-14	104,800 km before re-profiling	Yes
2	2014-12-18	0 km after re-profiling	Yes
3	2015-02-09	27,400 km after re-profiling	No
4	2015-03-28	49,800 km after re-profiling	No

The OOR profiles of all wheels of two electric locomotives were measured four times during the tracking test. The two locomotives operated coupled together throughout the test and were therefore subject to identical track and operating conditions. The wheel IDs are illustrated in Figure 5-5. The OOR profile was measured using a Müller-BBM, as shown in Figure 5-6. The probe was mainly positioned at the tap circle location that is 70mm from the wheel's flange back, and other lateral positions, such as 50 mm, 95 mm, 115 mm, and 125 mm were measured as well. The measured circumferential wear patterns are somewhat similar at different lateral positions in terms of the wavelength distribution, but some slight differences can be found in the roughness amplitude.

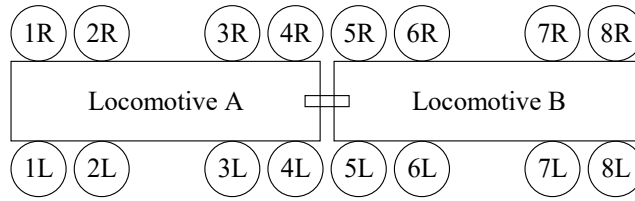


Figure 5-5 Illustration of wheel ID



Figure 5-6 Measurement of OOR profile

A schematic of the vibration test on the locomotive is shown in Figure 5-7. The sensors mounted are shown in Figure 5-8. The main concern is the abnormal vibrations of the axle box, the bogie frame, and the driver cab in the presence of wheel polygonization. In addition, some components such as the traction rod and the step under the driver cab are also included in the investigation scope, as they had been found to fracture during the operation.

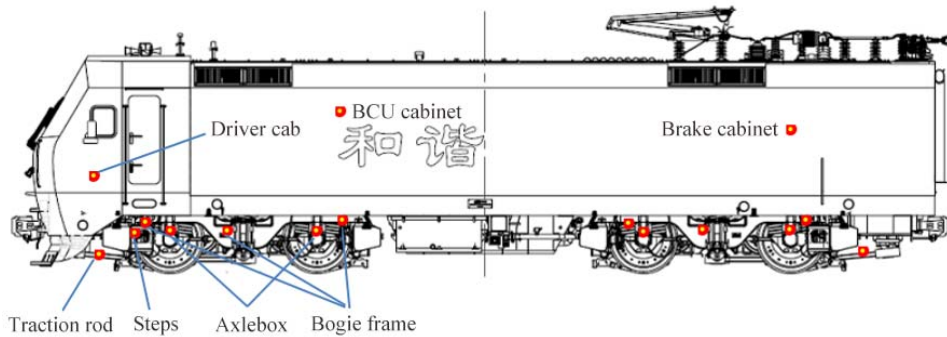


Figure 5-7 Scheme of vibration test



(a) Axle box

(b) Bogie frame

(c) Seat bottom in driver cab

(d) GPS velocity sensor

Figure 5-8 Sensor positions

5.3.2 Measurement results

5.3.2.1 Wheel OOR evolution

The wheel OOR evolution in the order spectrum and the 1/3 octave band spectrum are presented in Figure 5-9, and Figure 5-10 respectively, where the 16 grey lines in each sub-graph stand for the OOR data of each measured wheel, and the red line with circles is the averaged order spectrum of the 16 wheels.

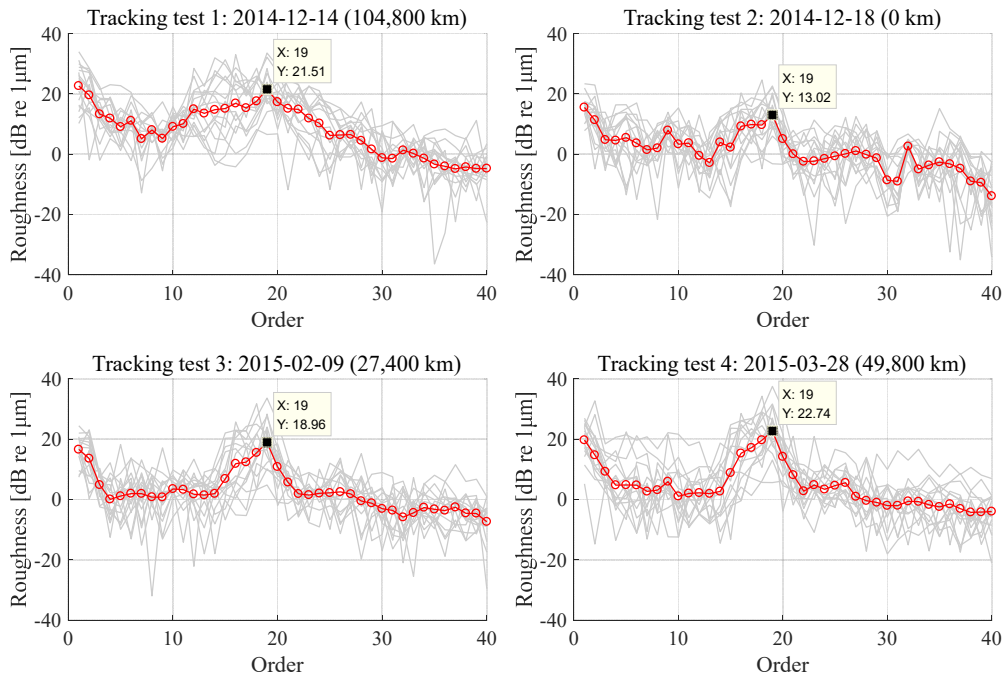


Figure 5-9 Evolution of the order spectrum of wheel OOR

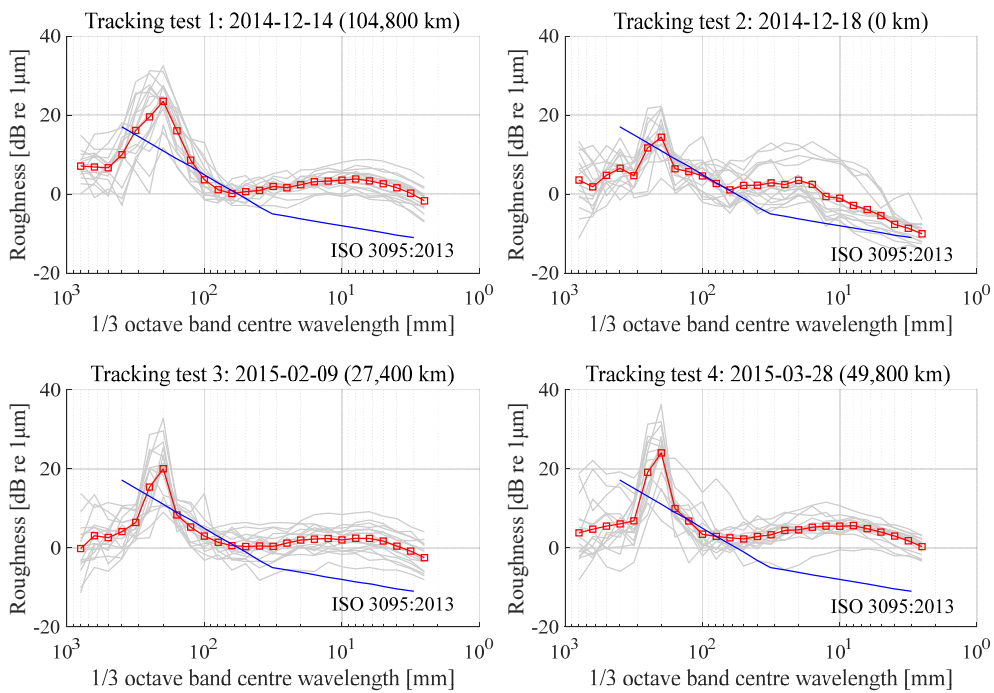


Figure 5-10 Evolution of the 1/3 octave band spectrum of wheel OOR

The blue line in the 1/3 octave band spectrum is the limit spectrum for rail roughness specified in ISO 3095:2013. The maximum order presented in the order spectrum is 40. The 1/3 octave band spectrum is not filtered to show the original OOR measured. Note that the roughness level for the short wavelengths is generally above the reference limit due to the inclusion of spikes that have not been filtered out. However, as mentioned above, specifying the lower limit of the short wavelength is scenario dependent, which can have an influence on the simulation results.

Overall, the range of orders that developed significantly during the tracking test is from 15 to 22, roughly corresponding to the range of wavelength from 180 to 260 mm, as can be seen from Figure 5-9 and Figure 5-10. Typically, the 19th order is the most dominant order developed, roughly corresponding to the wavelength of 200 mm. After running 104,800 km before the re-profiling, the roughness level of the 19th order had exceeded 20 dB, as shown in tracking test 1. At this point, due to the excessive vibration caused by the wheel OOR, all the wheels were re-profiled. However, it transpired that the underfloor wheel lathe used was not competent to eliminate the OOR roughness effectively. As shown in tracking test 2, the dominant order of 19 still existed stubbornly, with its roughness level only being reduced to about 12 dB by re-profiling.

With this rather big initial OOR, the polygonal wear then developed rapidly. The roughness level of the 19th order reached 18.96 dB after only 27,400 km (see tracking test 3), and 22.74 dB after only 49,800 km (see tracking test 4). The running distance of 49,800 km in tracking test 4 is less than half of 104,800 km in tracking test 1, but the roughness level of the 19th order in tracking test 4 (22.74 dB) is even higher than that in tracking test 1 (21.51 dB). This indicates that bad initial OOR is a crucial contributor to accelerate wheel OOR development. Thus, the underfloor wheel lathe has to be improved to guarantee better initial wheel OOR.

The change of wheel radius run-out during the tracking test is shown in Figure 5-11, where the 16 wheels are presented separately. The wheel radius run-out is the difference between the maximum wheel radius and the minimum wheel radius. According to EN 15313:2010 (Rail application: In-service wheelset operation requirements. In-service and off-vehicle wheelset maintenance) [90], the limit values for wheel circularity defects (e.g. polygonization, flats, cavity, etc.) shall be fixed on the basis of service experience.

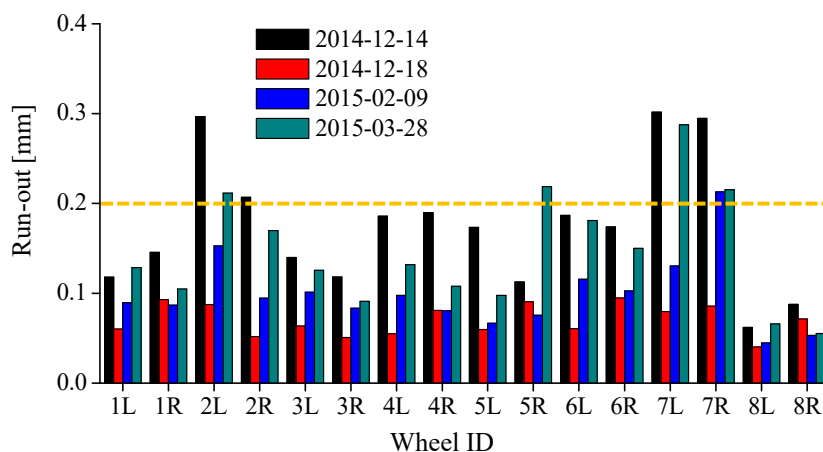
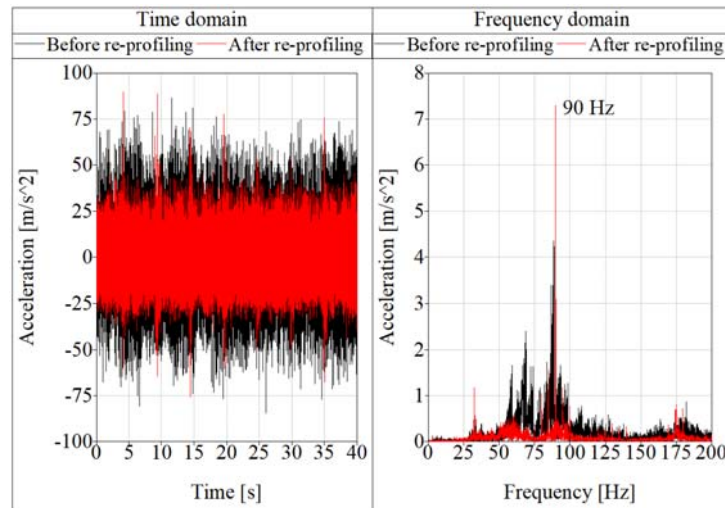


Figure 5-11 Tracking of the wheel radius run-out

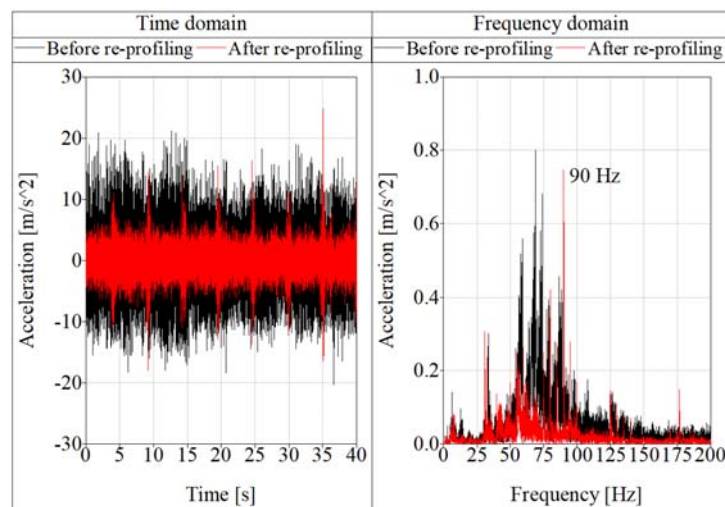
The dashed yellow line is the run-out limit (0.2 mm) specified by the local locomotive depot based on their practical experiences. As can be seen in Figure 5-11, the most severe wheelsets, whose wheel run-out exceeds the limit (0.2 mm), are the 2nd and 7th wheelsets. Interestingly, these two wheelsets are symmetrical with respect to the centre of the two-coupled locomotives (see Figure 5-5). When the wheel run-out exceeds the limit (0.2 mm), the wheels must be re-profiled.

5.3.2.2 Vibration test

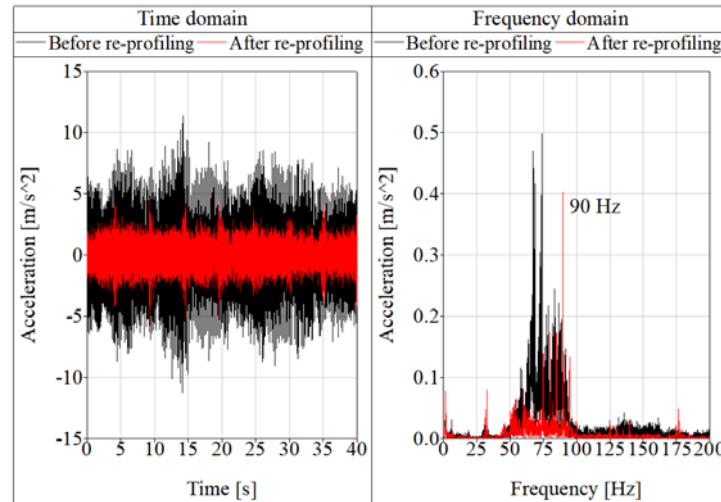
The vertical acceleration of axle box, bogie frame, and driver cab, before and after wheel re-profiling are presented in Figure 5-12. The vehicle was running on a straight track at a speed of around 70 km/h. The test sections of the track before and after wheel re-profiling are similar compared to each other in terms of the track irregularities and track stiffness. The sampling frequency is 5000 Hz. The testing time is 40 s.



(a) Axle Box



(b) Bogie frame



(c) Driver cab

Figure 5-12 Measured vertical acceleration of (a) Axle box, (b) Bogie frame, and (c) Driver cab, before and after wheel re-profiling

As can be seen from Figure 5-12, the main energy of vibration in the axle box, the bogie frame, and the driver cab were all distributed from 60 to 100 Hz in the frequency spectrum. At 70 km/h, this frequency band was exactly corresponding to the dominant OOR orders ranging from 12 to 20. This indicates that, if the wheel OOR is bad enough, it can dominate the vibration of the whole vehicle despite the isolation of two suspensions. The vibration of each component was reduced through wheel re-profiling, but the improvement was not significant due to limitations of the underfloor wheel lathe that cannot effectively eliminate the initial OOR. Indeed, the vibration at around 90 Hz was even more significant after wheel re-profiling than before. This is because the most dominant order of 19 corresponding to 90 Hz at 70 km/h could not be filtered out by the underfloor wheel lathe, and it even became more predominant after wheel re-profiling, as can be seen by comparing tracking test 3 to tracking test 2 in Figure 5-9.

5.4 Simulation of wheel OOR effects

5.4.1 Modelling of locomotive

The tested locomotive was modelled in Simpack, as shown in Figure 5-13, to simulate the wheel OOR effect on vehicle vibration in the case of tracking test 1 (before re-profiling).

- Vehicle model: This locomotive consists of two bogies with two wheelsets for each bogie. Each wheelset is connected to a motor to provide traction power. The bogie has two layers of suspension. Two driver cabs are located on both ends of the car body. The nominal wheel radius is 0.625 m. The non-linearity of the suspension dampers are considered in the model. The wheel OOR measured from tracking test 1 (before re-profiling) are assigned to each wheel.

- Track model: A co-running sleeper beneath each wheelset is built to represent the track flexibility. The sleeper passing frequency is defined in the ballast force element to take the sleeper passing oscillation into consideration.
- Wheel-rail contact: The wheel profile is JM3 [64], which is a typical wheel profile for Chinese locomotives. The rail profile used in the simulation is CN60 [65]. Hertz theory is adopted for the normal contact modelling. FASTSIM [81] is applied for the tangential contact force calculation.

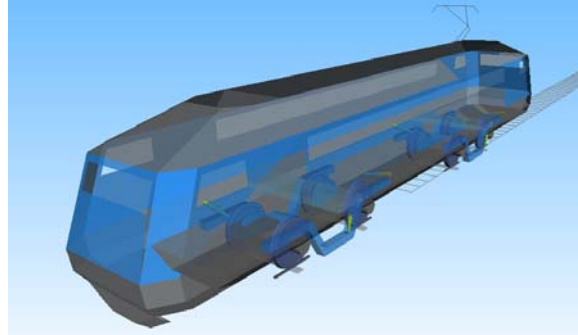
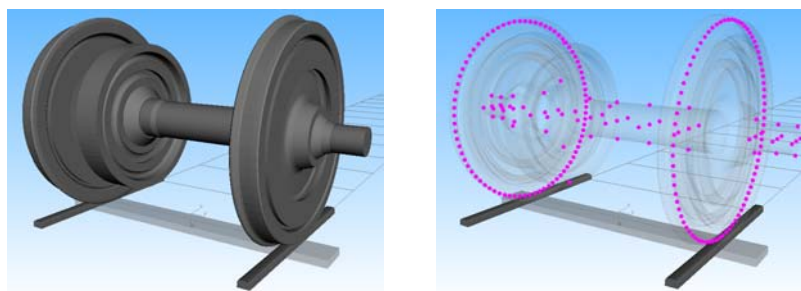


Figure 5-13 The tested locomotive built in Simpack

All vehicle components are modelled as rigid bodies except the wheelset. The wheelset with a big gear attached is modelled as a flexible body, which is shown in Figure 5-14 regarding the geometry, the master nodes specified, and the initial imbalance. Note that this initial imbalance is unavoidable, but can only be minimised by refining the FE mesh. If the geometry of the wheelset is asymmetric (e.g. the big gear is included in this case), there will be an initial imbalance of gravity centre in the y position, as indicated by a red rectangle in Figure 5-14 (c). This initial imbalance could induce a small periodic rolling vibration in the simulation but within an acceptable scope. The issues regarding the modelling of wheelset flexibility as well as the influence of wheelset flexibility on the wheel OOR evolution will be elaborated individually in Chapter 6.



(a) Geometry

(b) Master nodes

Mass:	3113.91476985705		
Center of Gravity			
Position:	x	y	z
	2.529858936143387e-12	-0.08185269740076126	1.466043963768766e-10
Relative to:	Body Reference Frame		
Inertia			
	x	y	z
Moments of inertia:	1591.692475808823	-2.044103922913972e-07	-1.157343014745568e-07
	syn	487.2414800665574	2.352104049176894e-07
	syn	syn	1591.692457518934
Relative to:	Center of Gravity		

(c) Initial imbalance

Figure 5-14 Flexible wheelset

5.4.2 Comparison between simulation and measurement

The locomotive built with real parameters was verified according to a previous dynamic report [91] in terms of the running stability, the riding comfort, the curve negotiation performance, and so on.

Unfortunately, the track property and the actual track irregularity were not measured for this tracking test. Consequently, in the simulation, the track irregularity can only be estimated by adopting an alternative track irregularity spectrum, which can lead to some inconformity between simulation and measurement. A Chinese track irregularity spectrum for the mainline is applied here. The vertical track irregularity is shown in Figure 5-15. The main track properties are estimated as vertical stiffness 3×10^8 N/m, lateral stiffness 8×10^8 N/m, vertical damping 1.5×10^5 Ns/m, lateral damping 2×10^3 Ns/m. The comparison was conducted between simulation and measurement for 26 channels of 3-axis vibration acceleration of axle box, bogie frame and driver cab. Some are similar, while some are not. Here only the vertical acceleration of the axle box above wheel 2L and bogie frame above wheel 2R is presented in Figure 5-16 as two typical examples.

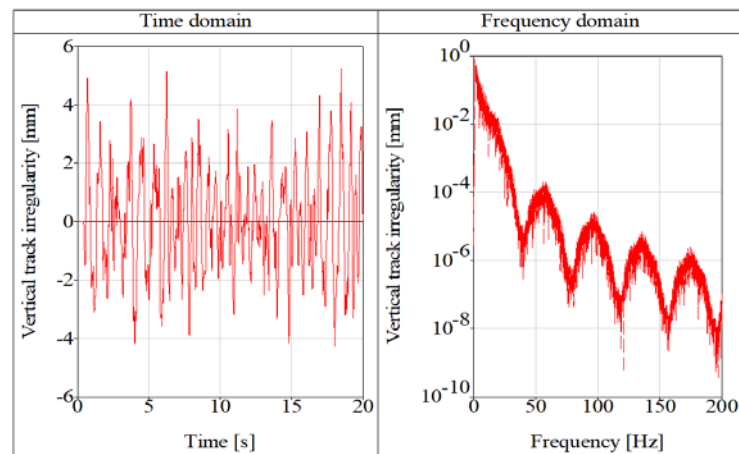
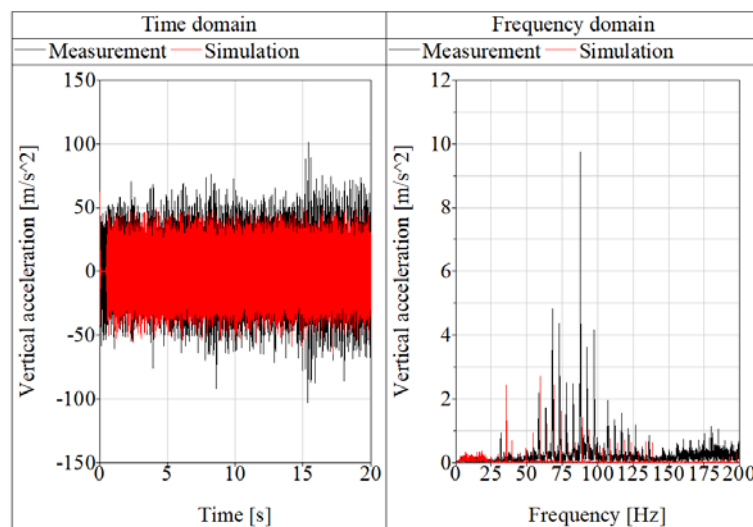
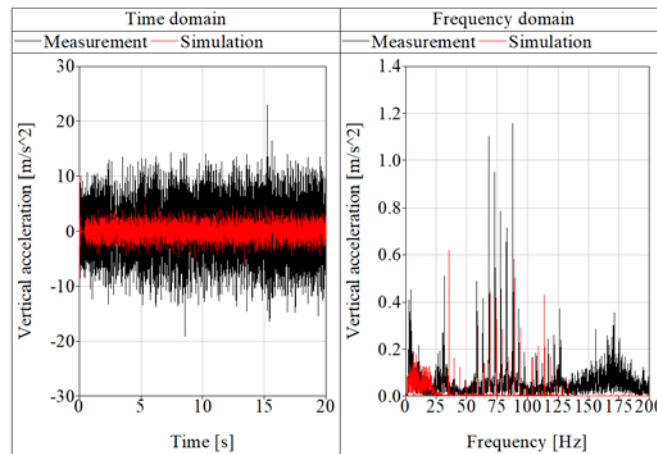


Figure 5-15 Vertical track irregularity



(a) Axle box



(b) Bogie frame

Figure 5-16 Comparison between simulation and measurement: (a) Axle box, (b) Bogie frame

If only checking the time domain, it can be found that the axle box acceleration in the simulation is rather similar to the measurement, with around 5% discrepancy in terms of the maximum amplitude. However, for the bogie frame, the simulation is much smaller than the measurement. Note that only the flexibility of the wheelset is considered in the vehicle modelling with all other components being modelled as rigid bodies. This could underestimate the effect of OOR on the vibration of bogie as well as the car body. When checking the frequency domain, it can be seen that the resonant vibration caused by the wheel OOR can be reflected by the simulation in the frequency range from 60 to 100 Hz, but the simulation is smaller than the measurement. This could be attributed to the non-conformity of the track properties or track irregularity.

5.4.3 Effects of wheel OOR on curve negotiation

The simulation is conducted for the locomotive with and without wheel OOR negotiating on a curve to check the influence of wheel OOR on curve negotiation. A rigorous scenario is simulated with a curve of radius 300 m and severe wheel run-out of 0.2 mm (the limit specified by the local locomotive depot for wheel re-profiling). The configuration of the curve is given in Table 5-2. There is no existing standard for assessing the effect of railway wheel OOR on the dynamic performance of the vehicle-track system. Usually, the limits of some dynamic indices specified in existing standards are employed as the reference to judge the impact of wheel OOR. Here UIC 518:2009 [92] is adopted as the referencing standard for the sum of guiding forces, the derailment coefficient, the acceleration of carbody, and the vertical wheel-rail force. EN 14363:2016 [93] is adopted as the referencing standard regarding the ratio of load reduction $\Delta Q/Q$, where ΔQ is the load reduction and Q is the static wheel-rail vertical force. The comparative simulation results are shown from Figure 5-17 to Figure 5-21. In all the figures, the red curves are the results with wheel OOR, the black curves are the results without wheel OOR, and the blue lines are the referring limits specified in UIC 518:2009 or EN 14363:2016. By comparing the difference between the red curve and the black curve, the effect of wheel OOR on curve negotiation can be identified in terms of these dynamic indices. Note that some indices (sum of guiding forces, derailment coefficient, and rate of load reduction) should be processed by sliding mean over 2 m according to the corresponding standards. However, the difference may not be observed after this processing. To illustrate the difference between with and without OOR, the original data without processing are also presented.

Table 5-2 Configuration of the curve

Curve radius	Transition	Curve length	Superelevation	Speed	Track irregularity
300 m	80 m	200 m	125 mm	70 km/h	FRA 5

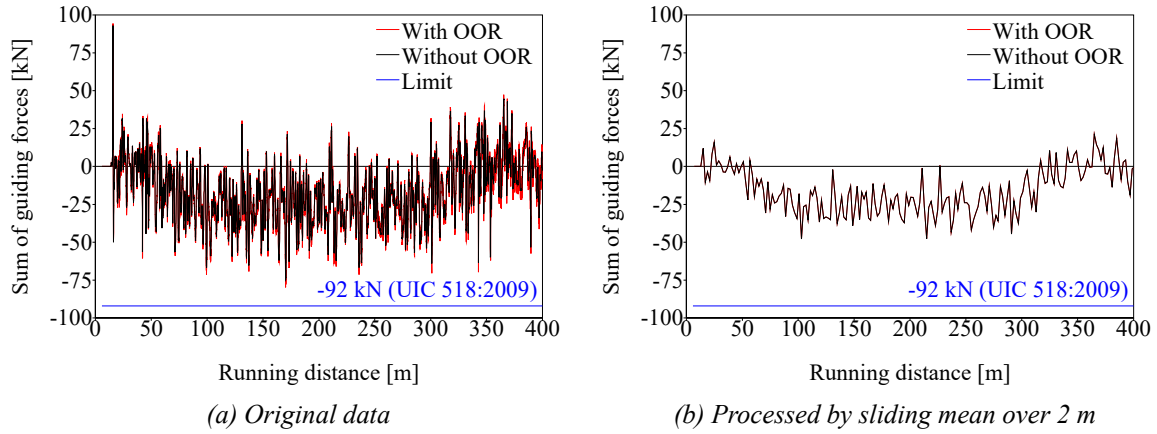


Figure 5-17 Sum of guiding forces with and without wheel OOR: (a) original data, (b) the data is processed by sliding mean over 2 m of track

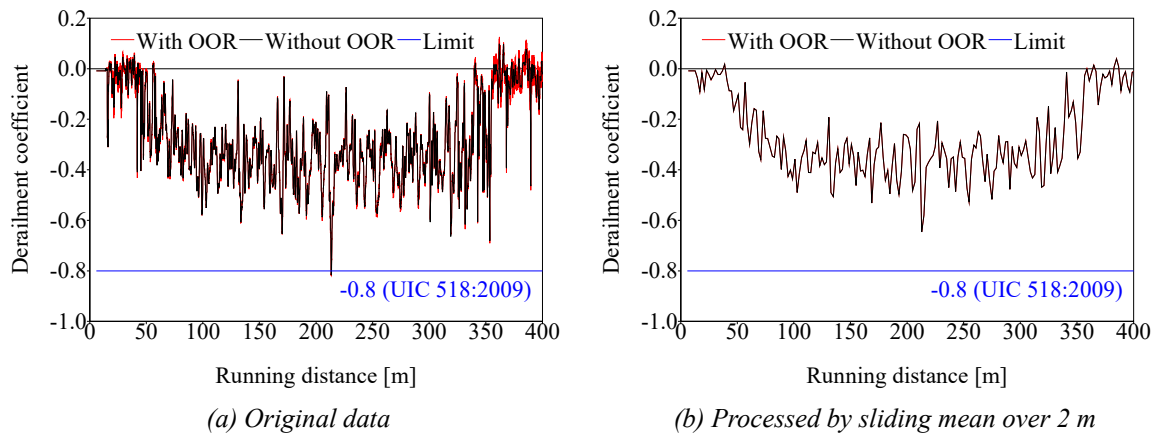


Figure 5-18 Derailment coefficient of the left wheel (outer side) with and without wheel OOR: (a) original data, (b) the data is processed by sliding mean over 2 m of track

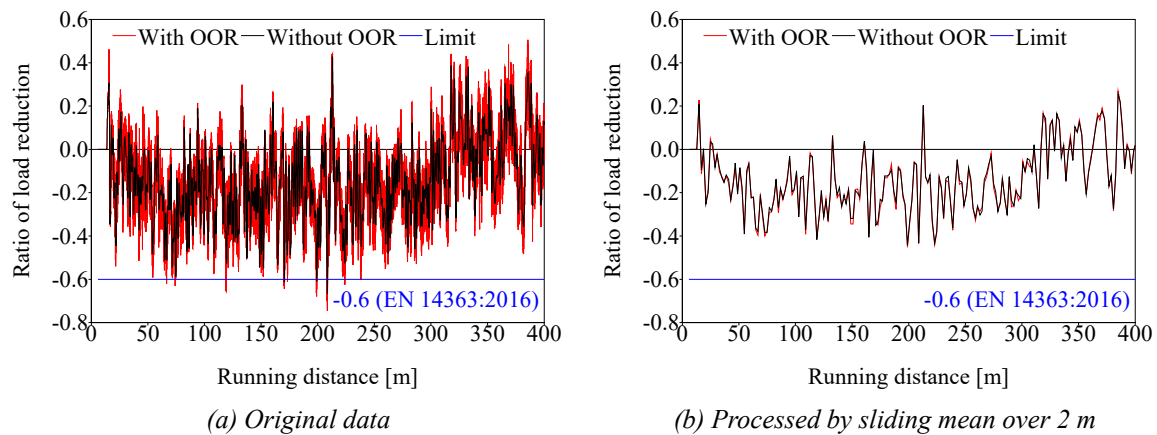


Figure 5-19 Ratio of load reduction of the right wheel (inner side) with and without wheel OOR: (a) original data, (b) the data is processed by sliding mean over 2 m of track

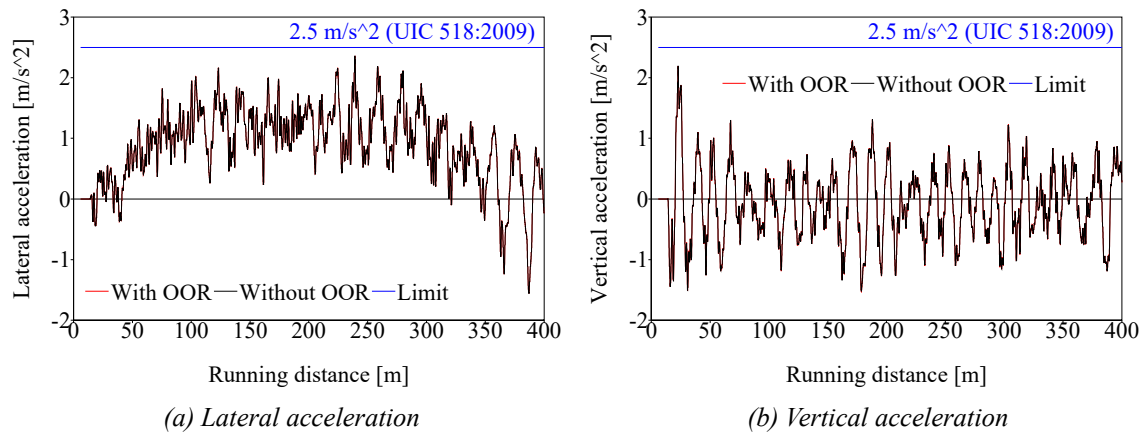


Figure 5-20 Acceleration of the seat bottom on the front driver cab with and without wheel OOR: (a) Lateral acceleration, (b) vertical acceleration

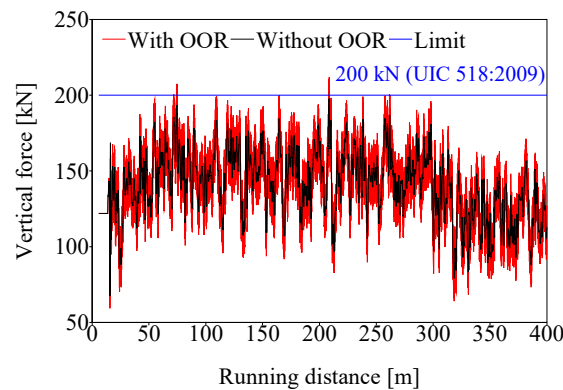


Figure 5-21 Vertical force of the left wheel (outer side) with and without wheel OOR

As can be seen from Figure 5-17 to Figure 5-19 regarding the aspect of safety, the original data of the sum of guiding forces, the derailment coefficient, and the rate of load reduction can be influenced by the wheel OOR but in a limited sense, with the rate of load reduction being influenced the most significantly. But if the data are processed using a sliding mean over 2 m according to UIC 518:2009, no difference can be observed with and without OOR, with all indices within the limits. This implies that the wheel OOR has a negligible influence on the safety of the vehicle-track system in this case where the wheel radius run-out is even at the limit value.

With respect to the running behaviour represented by the acceleration of driver cab, as shown in Figure 5-20, the wheel OOR presents imperceptible impact in both lateral and vertical directions. However, this simulation result could be unreliable as it is much different from the site experiment where the driver cab can be influenced by the wheel OOR significantly. This is because the flexibility of the carbody as well as other components (e.g. bogie frame) are not considered in the simulation model, which might underestimate the transmission of vibration from the wheel-rail interface to the driver cab. In addition, a more accurate modelling of the suspensions might also be needed, e.g. by considering the frequency-dependent characteristic of the springs.

The most affected index is the vertical wheel-rail force, as shown in Figure 5-21. The maximum of the vertical wheel-rail force is used as an index for assessing the track fatigue in UIC 518:2009 where the limitation is 200

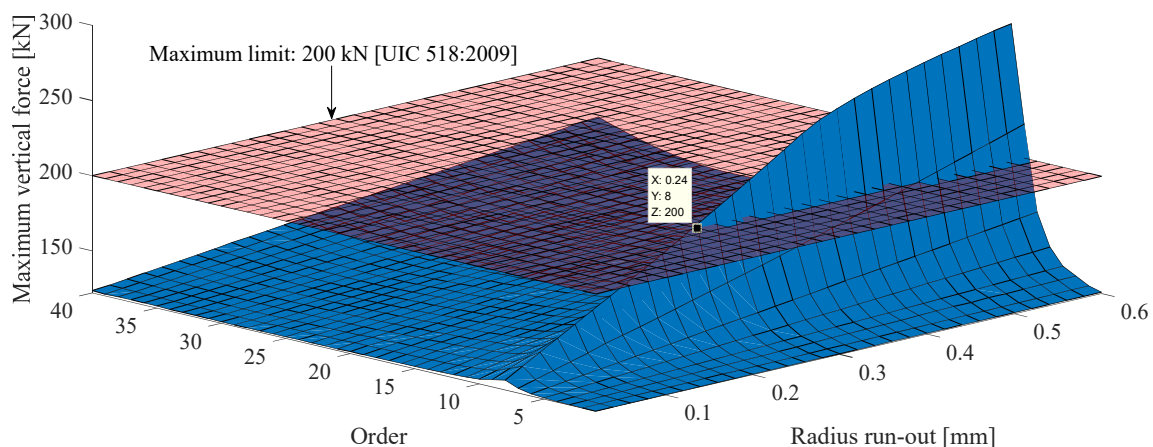
kN for a locomotive whose maximum speed is below 160 km/h. The wheel OOR can increase the vertical wheel-rail force severely, leading to increased possibilities of the vertical wheel-rail force to exceed the limitation. In most literature investigating the tolerable limitation of wheel OOR, the limitation of the vertical wheel-rail force specified in UIC 518:2009 is used as the judging reference. For example, for high-speed trains, the maximum vertical wheel-rail force caused by wheel OOR should be smaller than 170 kN.

5.4.4 Parametric analysis of the effects of wheel OOR

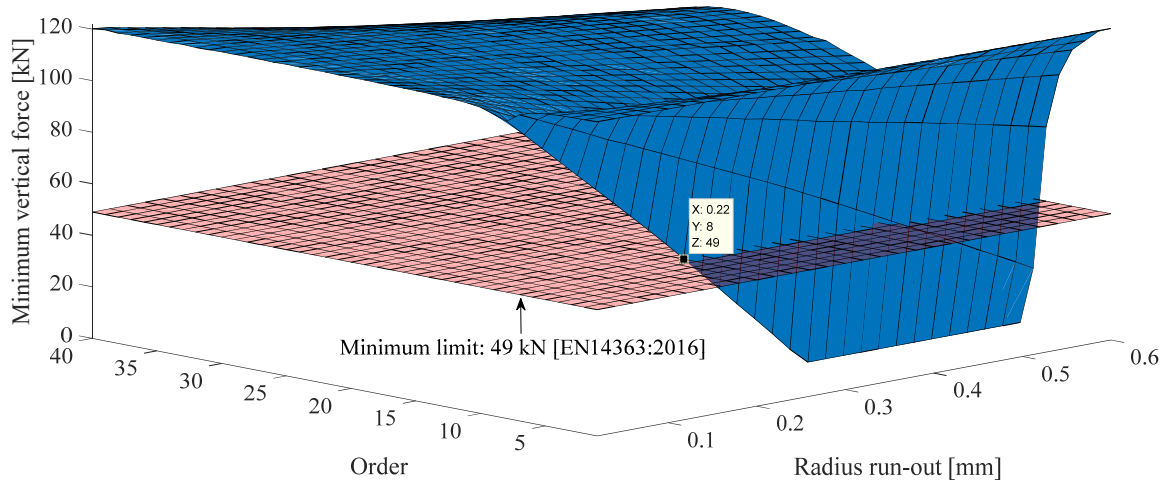
During rolling, the wheel OOR produces periodic excitation at the wheel-rail interface causing forced vibration of the vehicle-track dynamic system. At a given speed, for a sinusoidal wheel OOR, the excitation frequency of the forced vibration is determined according to Equation (5-4). The forced vibration caused by wheel OOR can lead to increased wheel-rail force and component accelerations. To quantitatively assess the effect of wheel OOR on the vehicle-track dynamic system, a parametric analysis is carried out with the OOR order and the wheel radius run-out as two individual variables to be investigated. Here the radius run-out is 2 times of the OOR amplitude for the case of sinusoidal OOR, which is also the difference value between the maximum and the minimum of the wheel radius. The following describes the simulation scenario:

- The locomotive, described in Section 5.4.1, is running on a straight track at a constant speed of 70 km/h.
- No track irregularity is considered to avoid interference.
- Wheelset flexibility is not considered.

The vertical wheel-rail force is the primary concern as the wheel OOR imposes a direct vertical excitation to the wheel-rail interface exacerbating the vertical force of the wheel-rail contact. The maximum and minimum vertical wheel-rail force of wheel 1L against the wheel OOR order (1-40) and the wheel radius run-out (0-0.6 mm) is presented in Figure 5-22.



(a) Maximum vertical wheel-rail force



(b) Minimum vertical wheel-rail force

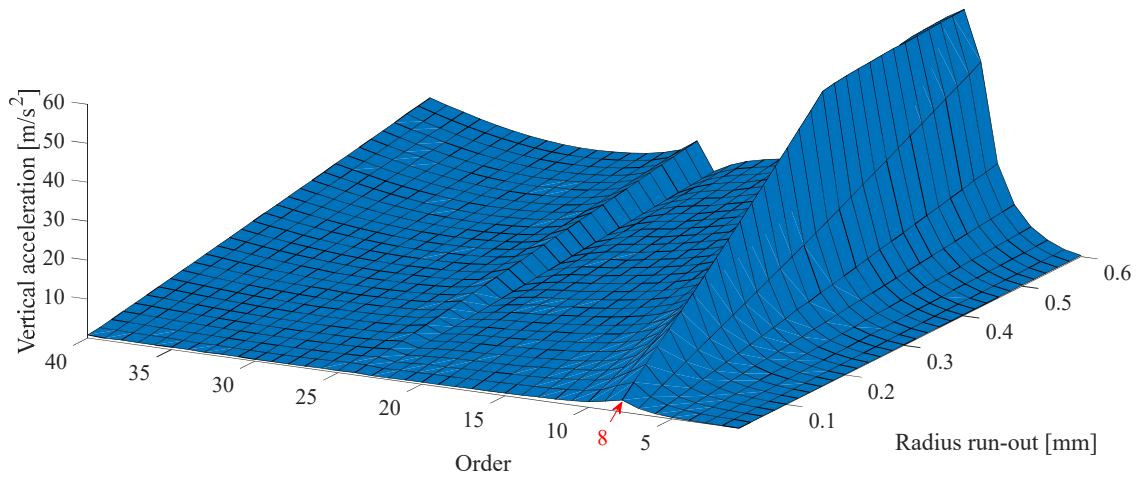
Figure 5-22 Vertical wheel-rail force against the OOR order and the wheel radius run-out (70 km/h): (a) Maximum vertical force, (b) Minimum vertical force

To better judge the severity of the wheel OOR, some existing standards are adopted to set the reference limit. According to UIC 518:2009, the limit of the maximum vertical wheel-rail force is 200 kN for a locomotive whose maximum speed is below 160 km/h. According to EN 14363:2016 [93], the limit of the ratio of load reduction is 0.6 so that the limit of the minimum vertical wheel-rail force can be estimated by $122 \times (1 - 0.6) \approx 49$ kN, where 122 is the static load. These two limits are displayed in Figure 5-22 as references to assess the effect of wheel OOR. For the upper sub-graph, if the maximum vertical force (blue surface) is above 200 kN (pink plane), the vibration is not acceptable. For the lower sub-graph, if the minimum vertical force (blue surface) is below 49 kN (pink plane), the safety is threatened.

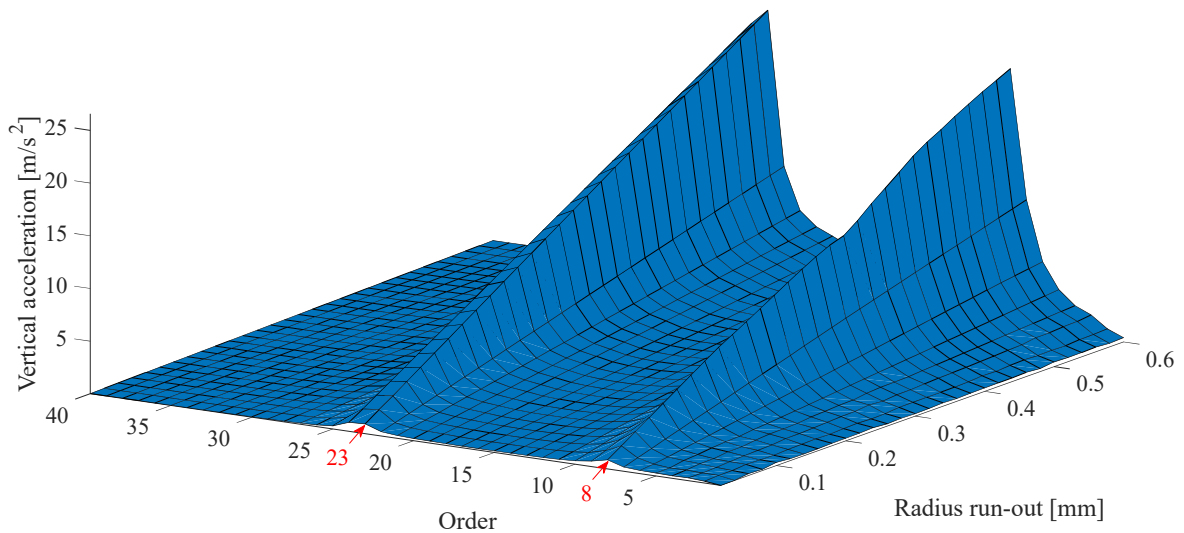
As can be seen from Figure 5-22, larger run-out can always lead to higher maximum vertical force and lower minimum vertical force, which is reasonable. While for the wheel OOR order, the 8th order presents a more dominant influence than other OOR orders. For all OOR orders, except the 8th order, the maximum and minimum vertical forces are within limits. For the 8th order, if the radius run-out is greater than 0.24 mm the maximum vertical force will exceed the maximum limit of 200 kN (see Figure 5-22 (a)), and if the radius run-out is bigger than 0.16, the minimum vertical force will be below the minimum limit of 49 kN (see Figure 5-22 (b)). This is because the excitation frequency of the 8th OOR order at the speed of 70 km/h is matching the P2 resonance frequency. The P2 resonance frequency is determined by the unsprung mass and the sleeper mass as well as the vertical track stiffness [94], which is around 40 Hz in this case. The excitation frequency of the 8th order at the speed of 70 km/h can be calculated according to Equation (5-4), which is $(70/3.6)/(3.925/8) = 39.6$ Hz. When the excitation frequency of the wheel OOR happens to be the P2 resonance frequency, the vertical wheel-rail force will fluctuate significantly due to the resonance. In this situation, the wheel-rail force can be very sensitive to the radius run-out. As can be seen in Figure 5-22 (b), if the radius run-out is approaching 0.3 mm for the 8th order, the minimum vertical wheel-rail force can reduce to 0 indicating wheel-rail contact separation.

In addition, the threshold of radius run-out for wheel re-profiling can also be estimated through this parameter analysis. In terms of the maximum vertical wheel-rail force, the threshold should be lower than 0.24 mm (see Figure 5-22 (a)), while in terms of the minimum vertical wheel-rail force, the threshold should be lower than 0.16 mm (see Figure 5-22 (b)). However, the limit of existing standards is only employed as alternative references. As mentioned above, the threshold of the wheel radius run-out should be established based on the local experience. For this locomotive, the threshold is 0.2 mm specified by the local locomotive depot.

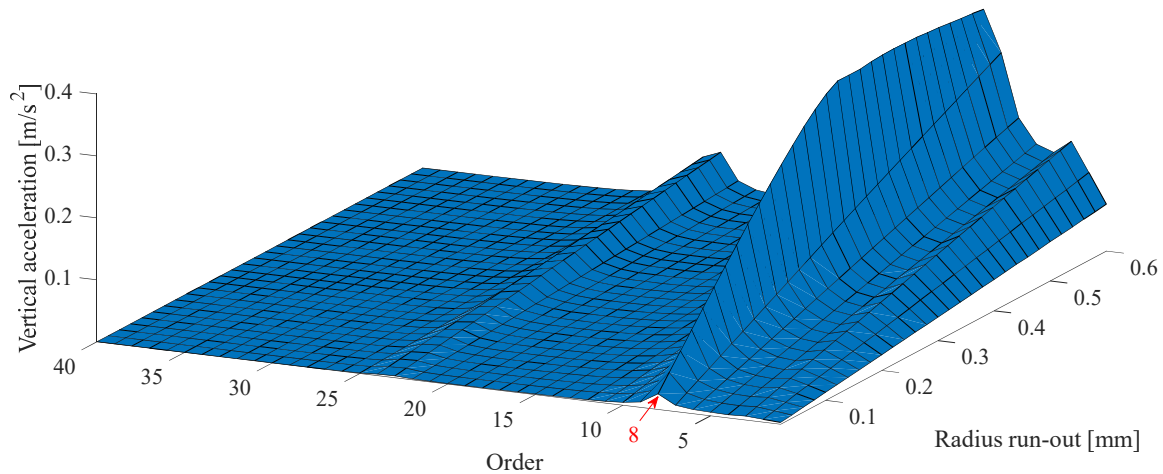
In addition to the vertical wheel-rail force, the vertical accelerations of some key components are also investigated. The maximum vertical accelerations of axle box, bogie frame, driver cab, and motor against the OOR order and the wheel radius run-out are presented in Figure 5-23.



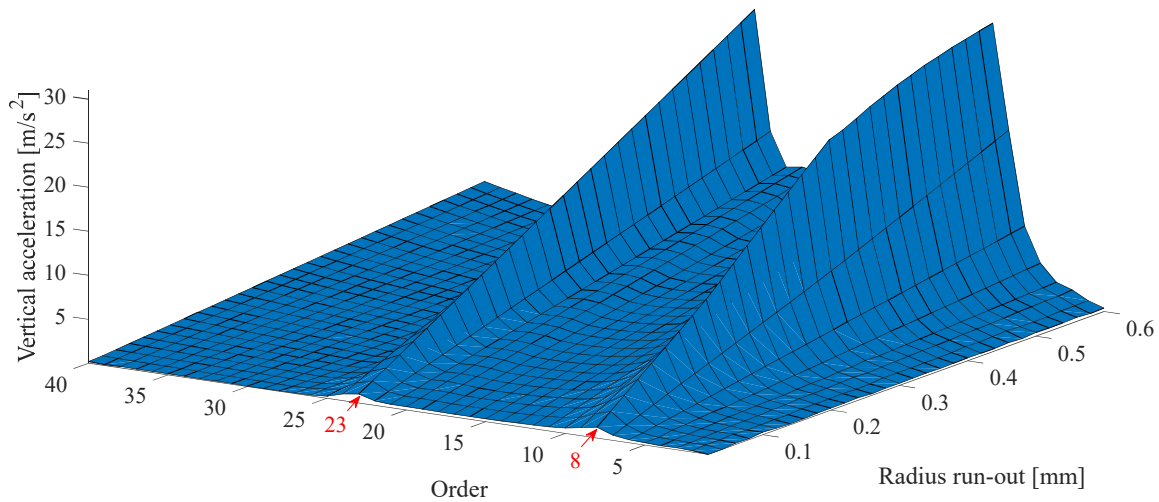
(a) Axle box



(b) Bogie frame



(c) Driver cab

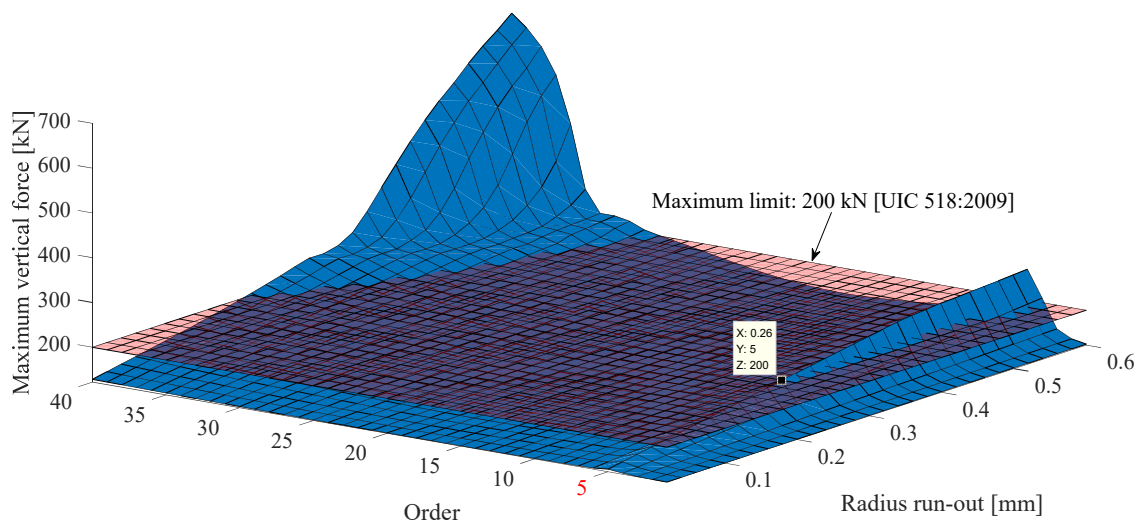


(d) Motor

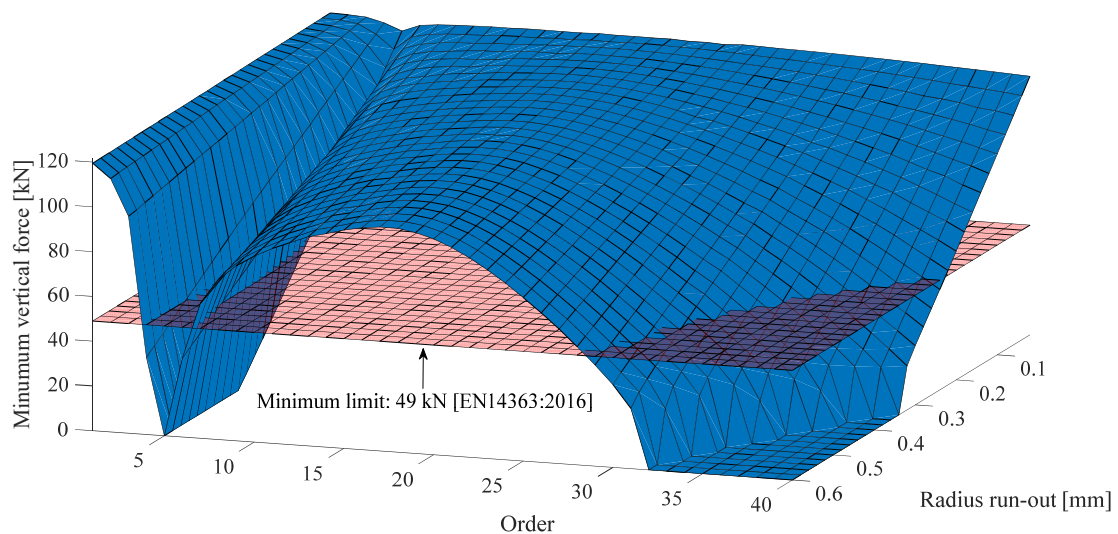
Figure 5-23 Maximum vertical acceleration of (a) Axle box, (b) Bogie frame, (c) Driver cab, and (d) Motor

As can be seen in Figure 5-23, the 8th order is always the most influential order that can affect the vertical acceleration of all the components. Note that the 8th order of wheel OOR at the speed of 70 km/h can lead to resonance in the P2 force. This implies that the resonant vibration caused by the wheel OOR with the order matching the P2 resonance frequency can be transmitted to all the components in the vertical direction, although the vibration amplitude will be reduced by the two-level suspension system. Besides, the 23rd order is also found to have a notable influence on the vertical acceleration of all components, especially for the bogie frame and the motor. The excitation frequency of the 23rd order at the speed of 70 km/h is $(70/3.6)/(3.925/23)=114$ Hz. And the modal frequency of the vertical vibration mode of the bogie frame is 116 Hz according to the Eigenvalue analysis in Simpack. It is naturally believed that the vertical vibration mode of the bogie frame is excited by the 23rd order of wheel OOR as the excitation frequency 114 matches the modal frequency 116 Hz. The resonance of this bogie frame mode can significantly amplify the vertical motion of the bogie frame and motor but have less influence on the axle box and the driver cab.

The vehicle speed is another important factor determining the excitation frequency of the wheel OOR. Further simulation is carried out by changing the speed to 120 km/h. The maximum and minimum vertical wheel-rail force at the speed of 120 km/h are presented in Figure 5-24. Note that the lower sub-graph is turned around to facilitate the observation of the minimum vertical wheel-rail force. Compared to Figure 5-22 where the speed is 70 km/h, in Figure 5-24 the vertical wheel-rail force fluctuates dramatically for higher OOR order and radius run-out, leading to rapidly increased maximum force and decreased minimum force. This is because higher speed will produce higher energy of vibration than lower speed for the same OOR order and radius run-out. As a result, the wheel OOR can have a more severe impact at a higher speed than at a lower speed. Besides, another important aspect is that the most influential order is shifted from 8 to 5 when the speed is changed from 70 km/h to 120 km/h. This is because that the OOR order corresponding to the P2 frequency will change with the speed according to Equation (5-4).



(a) Maximum vertical wheel-rail force



(b) Minimum vertical wheel-rail force

Figure 5-24 Vertical wheel-rail force against the OOR order and the wheel radius run-out (120 km/h): (a) Maximum vertical wheel-rail force, (b) Minimum vertical wheel-rail force

5.5 Summary

In this chapter, after introducing the OOR data analysis, a tracking test for a locomotive was presented in terms of the measurement of wheel OOR evolution and the vibration test in the presence of wheel OOR. Afterwards, a comparison was carried out between the simulation and the measurement. Based on the results from the simulation model, the effect of wheel OOR on curve negotiation was studied, and parameter analysis was performed to check the influence of OOR order and radius run-out on the dynamic performance of the vehicle quantitatively. Some main points are concluded as follows:

- (1) The wheel OOR introduces periodic excitation to the wheel-rail interface causing forced periodic vertical vibration to the whole vehicle-track dynamic system. To guarantee the safety and comfort of the vehicle, the maintenance period of wheels has to be reduced significantly in the presence of excessive OOR, resulting in higher maintenance cost.
- (2) The wheel OOR does not influence curve negotiation significantly.
- (3) Bigger wheel radius run-out will always produce more severe vibration. The limit threshold of the radius run-out for wheel re-profiling is currently based on the local experience. Normally, the limit value of the maximum vertical wheel-rail force specified in UIC 518 is adopted to judge the limit threshold of the wheel radius run-out.
- (4) The OOR order corresponding to the P2 frequency at a given speed was found to be the most influential order affecting the vehicle-track dynamic system. This order will vary with the vehicle speed in line with Equation (5-4). For some vehicle components (e.g. bogie frame or motor), if certain modes (e.g. the vertical vibration mode of bogie frame) can be excited effectively by the wheel OOR, the OOR order corresponding to this modal frequency at a given speed can also lead to a significant contribution to the vibration.
- (5) For optimal maintenance and wheelset life, appropriate limits for wheel radius run-out (based on geometric measurement) should therefore consider the amplitude of the run-out, the predominant OOR order measured, the operating speed, and fundamental resonant frequencies of the vehicle and track system.
- (6) In addition, when comparing the vehicle vibration between simulation and experiment in the presence of wheel OOR, the discrepancy can be large for the vehicle components that are far from the wheel-rail interface, e.g. the driver cab. The flexibility of the carbody and the bogie frame, as well as the frequency-dependent characteristic of the suspension spring, may have to be included to obtain more accurate simulation results that can match the reality. This is a future work.

Chapter 6 Influence of wheelset flexibility on railway wheel polygonization

6.1 Introduction

Among previous studies regarding the mechanism of railway wheel polygonization, a popular view is that the wheelset flexibility presents an important influence on the development of wheel polygonization. Specifically, the first bending mode of the wheelset has been argued to be the root cause for some orders of polygonization developed dominantly in particular vehicles (e.g. 18th order for a locomotive [29], 9th order for a metro train [5]). This hypothesis is supported by experiments finding that the natural frequency of the first bending mode of the wheelset is approximately corresponding to the passing frequency of the dominant orders of the wheel polygonization [5,29]. The lateral mode (the second bending mode) of the wheelset is also suspected of driving the development of the 24th order of wheel polygonization in a Chinese locomotive, which however has not been verified [29]. In addition, the torsional mode was found theoretically and experimentally to be the reason for a 20th order polygon of an electric locomotive in South Africa [95]. Two potential torsional vibration excitation mechanisms were explored, namely self-excited stick-slip vibration under saturated adhesion and forced excitation by the harmonics and inter-harmonics from a VFD (Variable Frequency Drive) driven AC (Alternating Current) traction motor [95].

Wheelset flexibility has also been argued as an essential factor for the wheel/rail interface issues in the mid-frequency range (50 Hz - 500 Hz) [96,97], with wheel polygonization being a typical one. In terms of the influence of wheelset flexibility on the wheel/rail forces, Fermer and Nielsen found that flexible wheels can considerably reduce the contact force [98]. Chaar and Berg found that the wheelset flexibility increases the lateral track forces significantly, which is in a good agreement with measurements [99]. However, Guiral simulated reduced vibration of tangential and normal forces when taking into account the structural deformation of the wheelset by using a self-developed program that can deal with curve negotiation [100]. The difference could be due to different methods and cases. Baeza indicated that the rigid and non-rotating elastic wheelset model might misinterpret the wavelength fixation mechanism in corrugation calculation relative to rotating elastic wheelset [101]. Torstensson compared wheel-rail contact forces using rigid, non-rotating flexible, and rotating flexible wheelsets, and suggested to use the rotating flexible wheelset for load cases leading to a significant magnitude of contact force components in the high-frequency range (above 1.5 kHz) [102].

This chapter is carrying out a fundamental investigation through simulation to check whether wheelset flexibility can influence the development of railway wheel polygonization in a general sense. To this end, a comprehensive comparison is implemented between a flexible wheelset and a rigid wheelset in three aspects: the frequency response function, the contact responses, and the development of wheel polygonization.

6.2 Modelling of the flexible wheelset

A simple wheelset instead of a full vehicle is deliberately adopted here to minimise interfering factors, as the major influencing factor of interest in this chapter is the wheelset flexibility. A simple co-running sleeper following the wheelset is used to simply represent the track flexibility. Guidance forces with linear stiffness and damping in 3 axes are applied at both sides of the wheelset axle, representing the dynamic coupling effect from the bogie frame. A wheelset of a Chinese locomotive with axle load (23 Tonne) is adopted as the research object. The wheel profile is JM3 [64], and the rail profile is CN60 [65]. The main parameters of the model are listed in Table 6-1.

Table 6-1 Main model parameters

Main parameters	Value	Unit
Wheelset mass	4560	kg
Radius	0.625	m
Wheelset Ixx	2822	kg·m ²
Wheelset Iyy	737	kg·m ²
Wheelset Izz	2822	kg·m ²
Longitudinal stiffness of primary suspension	3.6e7	N/m
Lateral stiffness of primary suspension	4.8e6	N/m
Vertical stiffness of primary suspension	2.9e6	N/m
Vertical damping of primary suspension	4e4	Nm/s
Vertical stiffness of ballast	1.5e8	N/m
Vertical damping of ballast	1.9e5	Ns/m

The geometry of the wheelset is simplified by equally distributing the mass of the attachments (gear, gearbox and motor suspension tube) on the wheelset to avoid a big initial imbalance introduced by the attachments that can interfere with the observation of the influence of the wheelset flexibility. After successively using SolidWorks for geometry modelling, Hypermesh for meshing, and Abaqus for generating the FE substructure, the flexible wheelset was imported into Simpack through the ‘Craig-Bampton’ method [103], which is a method for reducing the size (degrees of freedom) of the FE model to integrate the flexible model (known as a superelement) into the MBS software. Figure 6-1 shows the meshing and the selection of the master nodes of the wheelset. Table 6-2 lists the flexible modes with a comparison between the modal frequencies and substructure frequencies, showing the reduced accuracy due to the selection of master nodes. It is worthy of mentioning that the wheelset flexible frequencies in the simulation are not accurate compared to those in reality due to the simplification of the geometry. However, the intention is not to faithfully replicate the modal response of a specific wheelset, but to have plausible characteristics to work with. The specific value of the flexible frequencies is not expected to affect this fundamental research that is focusing on whether some flexible modes can be effectively excited to initiate the wheel polygonization.

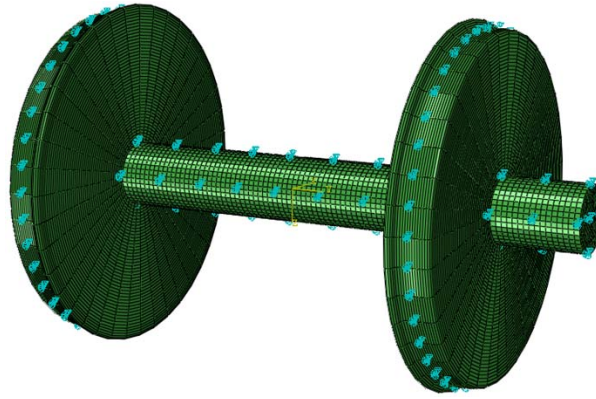
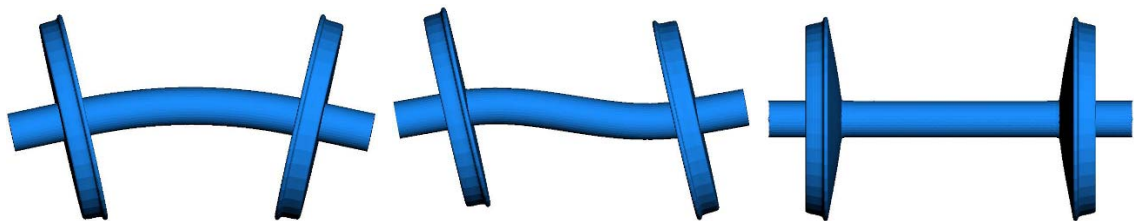


Figure 6-1 Meshing and selection of master nodes of the wheelset

Table 6-2 Wheelset flexible modes

Modes	Modal frequency [Hz]	Substructure frequency [Hz]	Discrepancy [%]	Remarks
1	50.03	50.05	0.04%	Torsional mode
2	71.18	71.30	0.17%	1 st bending mode
3	135.33	136.00	0.50%	2 nd bending mode
4	278.65	288.07	3.38%	Umbrella mode

Knowing that the operational speed of the locomotive being investigated is relative slow (normally below 80km/h), the first 4 modes with frequencies below 300 Hz are chosen for this investigation. The modal shapes of the 1st bending mode, the 2nd bending mode and the umbrella mode are illustrated in Figure 6-2. As a symmetrical rotating body, the bending modes have two orthogonal identical shapes that will co-occur in the global Cartesian coordinate system, which can lead to frequency bifurcation for high-speed rotation. In addition, a tiny wheelset imbalance is unavoidably introduced to Simpack along with the transfer of the flexible wheelset body due to the FE meshing. This imbalance cannot be eliminated, but can only be minimised by refining the FE mesh. In order to get comparable results, the rigid wheelset, used for comparison, is configured with the same initial imbalance.



(a) the 1st bending mode (71 Hz) (b) the 2nd bending mode (136 Hz) (c) umbrella mode (288 Hz)

Figure 6-2 Flexible mode shapes of the wheelset

6.3 Frequency response analysis

The FRF analysis of the flexible wheelset is important as it can show whether the flexible modes can be easily excited within a given frequency range. To obtain an informative FRF of the wheelset for the issue of polygonal wear occurring at the wheel/rail interface, two particular aspects need to be pointed out in terms of the

input/output configuration. Firstly, the input of the wheelset FRF should be the track irregularity which is a displacement input, because it is the only external excitation in reality if the motor vibration is not accounted for. The normal force at the contact point should not be taken as the input, but one of the outputs. Secondly, the output point is also at the wheel/rail contact position for the interest is focused on the contact responses that determine the wheel/rail wear. However, the contact patch is a moving patch around the wheel circumference. As a result, the rotating effect of the wheelset should be taken into consideration. To carry out such FRF analysis of the wheelset, two circumstances are investigated, namely the free wheelset and the on-track wheelset.

6.3.1 Free wheelset

The configuration for the free wheelset FRF analysis is shown in Figure 6-3. A dummy ground is configured with a moving vertical joint driven by a vertical displacement excitation dz as the input. The contact between the wheelset and the dummy ground is established by adding a pair of special moved contact markers to the respective bodies. The two corresponding contact markers can locate the potential contact point 'online' during the simulation. The flexible deformation of the wheelset is automatically taken into account for the contact search, which allows a realistic simulation even the wheelset is rotating. A linear vertical spring is applied between the corresponding contact markers to approximately represent the normal force at the wheel/rail interface.

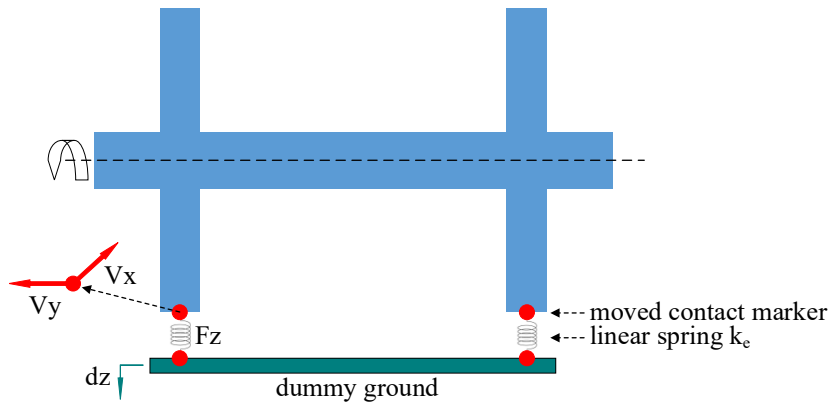


Figure 6-3 Configuration of FRF analysis for a free wheelset

The linear spring stiffness is estimated according to the non-linear Hertz normal force Equation (6-1) referring to [104].

$$p(t) = \left[\frac{1}{G} \delta Z(t) \right]^{3/2} \quad (6-1)$$

where: $p(t)$ is the normal force (N), $\delta Z(t)$ is the elastic penetration (m). So that the non-linear Hertz contact stiffness K can be written as:

$$K = \frac{1}{G} p^{1/3}(t) \quad (6-2)$$

where: $G = 3.86 R^{-0.115} \times 10^{-8}$ ($m / N^{2/3}$) for a worn profile tread [104], R is the wheel radius (m).

Admittedly, the contact stiffness is varied with the normal force. However, to carry out a FRF analysis that can only be done for a linear system, the approximation has to be made. Given the preload normal force P_n (112.364 kN), an equivalent linear normal stiffness K_e is estimated as below.

$$K_e = \frac{1}{G} p_n = 112364 / (3.86 \times 0.625^{-0.115} \times 10^{-8}) \approx 1.2e9 \quad (N/m) \quad (6-3)$$

The wheelset can rotate with an initial angular velocity without stopping as no friction is applied against the rotation. The normal force F_z , the lateral velocity V_y and the longitudinal velocity V_x of the contact marker on the wheels are set as the outputs to investigate the contact responses in 3 directions. The velocity rather than the displacement of the contact point is adopted as the output because the creepage is of more interest as an important factor in determining the wheel wear, although the FRF shape of the displacement and velocity are similar (but still different). The FRF is analyzed with a comparison between the rigid wheelset, non-rotating flexible wheelset, rotating flexible wheelset (120 km/h), and rotating flexible wheelset (350 km/h), so that the influence of the wheelset flexibility, as well as the rotating effect, can be identified. The FRF analysis results are shown in Figure 6-4.

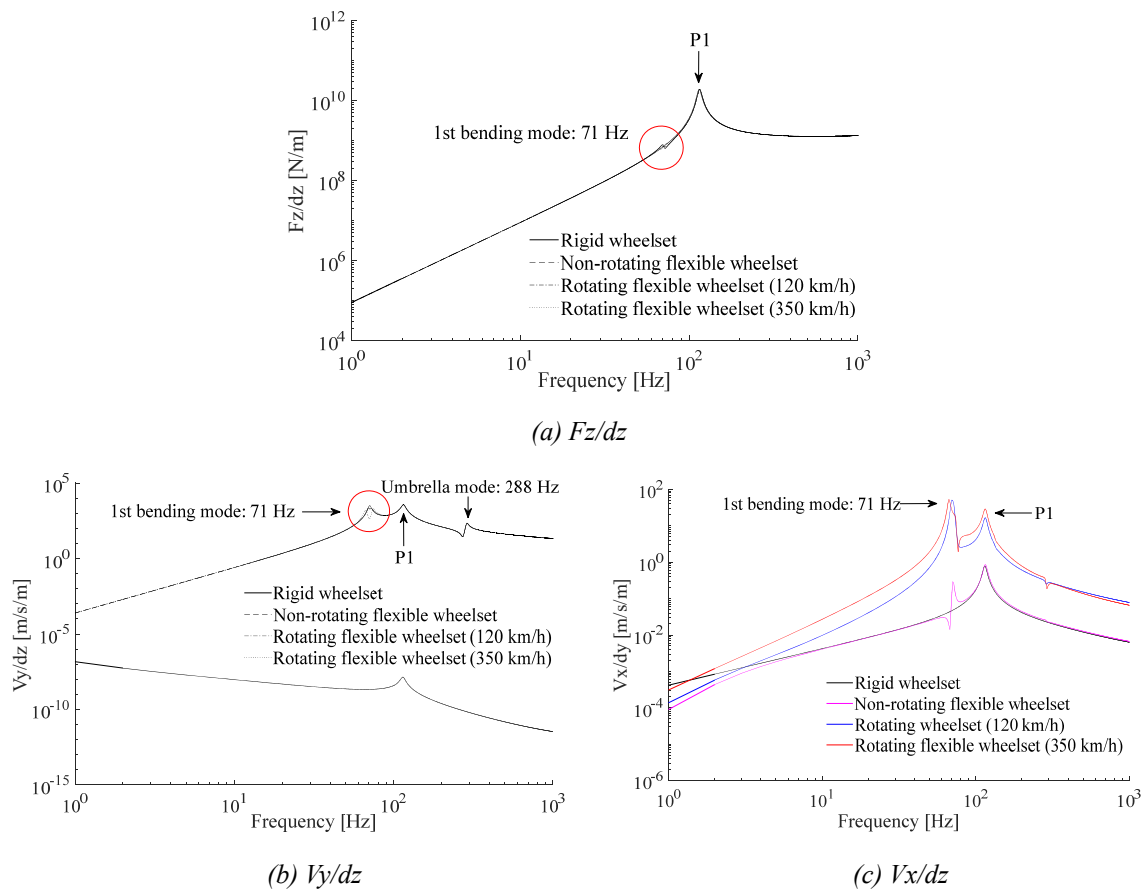


Figure 6-4 FRFs of the contact responses for a **free** wheelset with comparison between rigid wheelset, non-rotating flexible wheelset, rotating flexible wheelset (120 km/h), and rotating flexible wheelset (350 km/h): (a) the normal force F_z over the vertical displacement dz , (b) the lateral velocity V_y over the vertical displacement dz , and (c) the longitudinal velocity V_x over the vertical displacement dz

For the FRF of the normal force (see Figure 6-4 (a)), the wheelset flexibility does not show a noticeable effect, with only a slight difference observed at the position of the 1st bending modal frequency (see the red circle in Figure 6-4 (a)). However, the FRF of the lateral velocity of the contact point can be significantly affected by the wheelset flexibility (see Figure 6-4 (b)). Firstly, for the rigid wheelset, a vertical displacement excitation at

the contact position can hardly lead to a lateral displacement of the contact point. So the FRF of the rigid wheelset is at a very low level and consequently not comparable with that of the flexible wheelsets. Secondly, for the flexible wheelsets, two distinct peaks appear at the position of the 1st bending mode (71 Hz) and the umbrella mode (288 Hz). This is because these two modal shapes allow a lateral deformation at the contact point. Thirdly, the rotation effect is observed at the position of the 1st bending mode (see the red circle in Figure 6-4 (b)). In terms of the FRF of the longitudinal velocity (see Figure 6-4 (c)), the 1st bending modal frequency is also found appearing in the FRF for the flexible wheelsets. The rotation will further amplify the FRF amplitude, and the peak at the 1st bending frequency becomes predominant. In addition, there is a dominant peak at around 116 Hz in all the FRFs, which is so-called P1 resonance. The frequency of P1 force is determined by the un-sprung mass (wheel and associated axle mass, bearings and brake gear) and the Hertzian stiffness at the contact patch [94]. But this P1 frequency will be shifted to a high frequency (around 672 Hz) when the track flexibility is considered, which can be seen in the following section. Actually, this P1 frequency will be even higher in reality than in simulation, and it will be filtered as the interested frequency range is below 300 Hz.

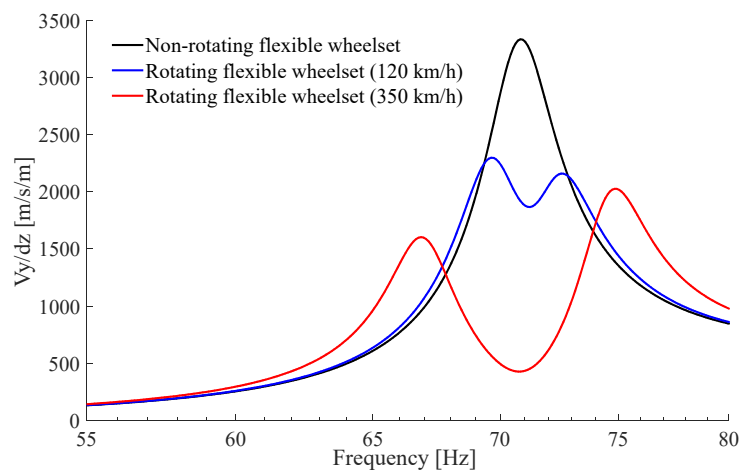


Figure 6-5 The rotation effect for the 1st bending mode of the wheelset

Figure 6-5 shows the detail of the rotation effect for the 1st bending mode. For a rotating flexible component, there will be a divergence effect for the flexible modes that have two orthogonal shapes (e.g. the 1st bending mode of the wheelset). Due to the rotation, eigenmodes of multiplicity two will split into backward and forward whirl modes which diverge in frequency with increasing rotational speed [102]. As can be seen in Figure 6-5, the divergence phenomena are not evident for a rotating speed of 120 km/h, which is the maximal operating speed of the locomotive wheelset investigated in this chapter. However, if the rotating speed is increased to 350 km/h, the divergence phenomena become apparent. This implies that the necessity of considering the rotation effect mainly depends on the train speed. For a low-speed locomotive, the rotation effect is negligible.

6.3.2 On-track wheelset

An alternative way to investigate the frequency response of the contact is to run the wheelset on an actual track. This is allowed in Simpack by assigning local excitations to the rails, by which the contact responses against the track irregularity in the frequency domain can be obtained directly. The local excitation is a type of distance

frequency domain excitation and will be automatically converted into the time-frequency domain with the vehicle speed. This method facilitates the investigation of the FRF of the contact responses in a more realistic situation where the non-linear wheel/rail contact, the primary suspension, and the co-running sleeper can be accounted for. Note that the non-linear wheel/rail contact will be automatically linearized in this method. The comparison is implemented between rigid and flexible wheelsets running at 70 km/h. The higher speed is not considered in this case as the rotation effect is not obvious below 120 km/h. With the vertical track irregularity as the input, the contact FRF analysis results are shown in Figure 6-6.

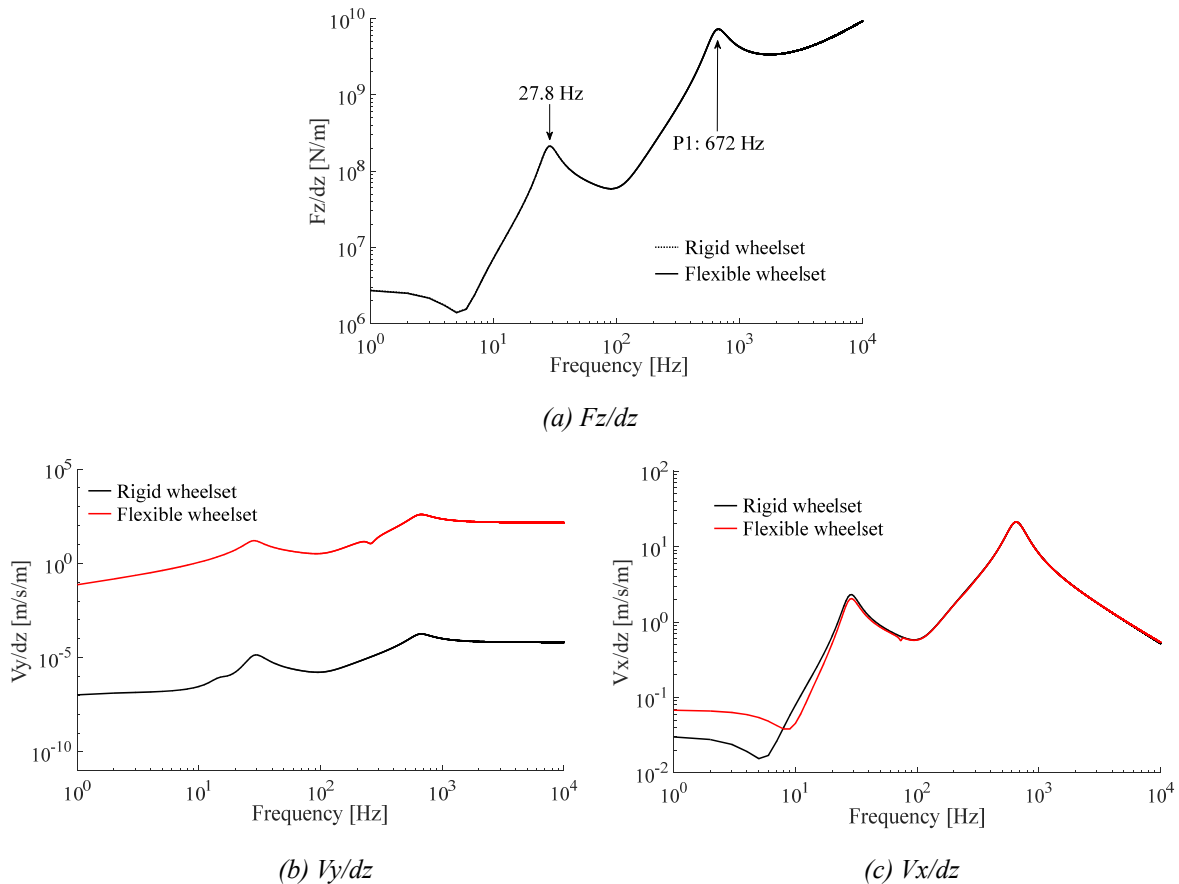


Figure 6-6 FRFs of the contact responses for an **on-track** wheelset with a comparison between rigid and flexible wheelsets: (a) Normal force Fz over vertical track irregularity dz , (b) Lateral relative velocity Vy over vertical track irregularity dz , and (c) Longitudinal relative velocity Vx over vertical track irregularity dz

First, there are two dominant peaks in all the FRFs. The peak at 27.8 Hz is a rigid modal frequency of the wheelset & sleeper with respect to the ground, which is determined by the mass of wheelset & sleeper and the vertical stiffness of the sleeper. The peak at 672 Hz is the P1 resonance that is increased compared to the free wheelset due to the track flexibility considered here. Despite this, the important aspect is that the wheelset flexibility does not demonstrate an obvious influence on the frequency components of the FRFs, except that the FRF amplitude of the lateral relative velocity is shifted to a higher level. In other words, no peaks corresponding to the wheelset flexible frequencies are found in the FRFs in any of the three directions. This implies that the flexible wheelset modes cannot easily be excited in an MBS simulation, which is further

confirmed in the following sections. This is not consistent with the free wheelset where the FRFs of the lateral and longitudinal velocity is found to be significantly influenced by the wheelset flexibility (see Figure 6-4 (b) and (c)). The reasons for this are not clear, but suspicion is put on the normal contact model. It is found that if the normal contact stiffness is significantly increased (e.g. 100 times the normal value), the flexible wheelset modes can be successfully excited in the case of on-track wheelset where the Hertz normal contact model is used. Although this is only a hypothetical test that is not realistic, it might draw attention to the normal contact model which is associated with the material and the elastic contact modelling, and implies that accurate contact stiffness value is critical to a realistic simulation of flexible wheelsets.

6.4 Influence of wheelset flexibility on contact responses

The Archard & FASTSIM wear model, which is also known as the KTH (Royal Institute of Technology) wear model [73], is employed to calculate the circumferential wear depth with nine contact parameters as the inputs: normal force; creepages (longitudinal, lateral, and spin); contact patch size (semi-axis a and b); and Kalker coefficient (C_{11} , C_{22} , and C_{23}). Note that the contact patch size and Kalker coefficients are dependent on the normal force. As a result, only the normal force and the creepages (Spin is not shown below) are in the scope of the investigation. The instantaneous Archard wear depth is also included in the comparison. White noise with a flat-PSD (Power Spectrum Density with a constant value) is used as the excitation of track irregularity. The upper frequency is 300 Hz, and the amplitude is around 0.01 mm. A large number of simulations under different circumstances (e.g. straight and curved tracks, vertical and lateral excitation, and traction) have been carried out to check whether, and in what conditions, the flexible wheelset modes can be effectively excited to influence the contact parameters in both time and frequency domain. Only representative results of two scenarios are presented: straight track and curved track with a small radius.

6.4.1 Straight track

At a speed of 70km/h, with vertical track irregularity of white noise as the excitation, the wheelset is run on a straight track for 50 revolutions. The contact responses of the normal force, longitudinal creepage, lateral creepage and the Archard wear depth for both rigid and flexible wheelsets are shown in Figure 6-7.

Comparing the flexible wheelset with the rigid wheelset in the time domain, the normal force is slightly attenuated; the longitudinal creepage remains the same; however, the lateral creepage is significantly increased. When comparing in the frequency domain, the normal force, as well as the longitudinal creepage, present the negligible difference between rigid and flexible wheelsets, but the lateral creepage is largely increased due to the wheelset flexibility, as can be seen clearly in Figure 6-7 (c). When checking the wheel wear, it is found that the Archard wear depth is slightly decreased due to the wheelset flexibility in the time domain, while remains similar in the frequency domain between rigid and flexible wheelsets. Note that in the case of a straight track, the lateral creepage is at a low level. So even a largely increased lateral creepage has less weight than a slightly reduced normal force in determining the Archard wear depth. In addition, there are 2 obvious peaks in the frequency spectrum of contact responses and wheel wear. The peak at 5 Hz is due to the initial wheelset imbalance introduced by the FE meshing (see Section 6.2), which is also the rolling frequency (in this case:

70/3.6/3.925 \approx 5 Hz). The peak at 27.8 Hz is due to the vertical rigid body mode of the wheelset & sleeper with respect to the ground, which is determined by the mass of wheelset & sleeper and the vertical stiffness of the sleeper. Other than these, there are no resonant peaks found for the wheelset flexible modal frequencies in the frequency spectrum for all 3 directions, which however is consistent with the FRFs of the on-track wheelset.

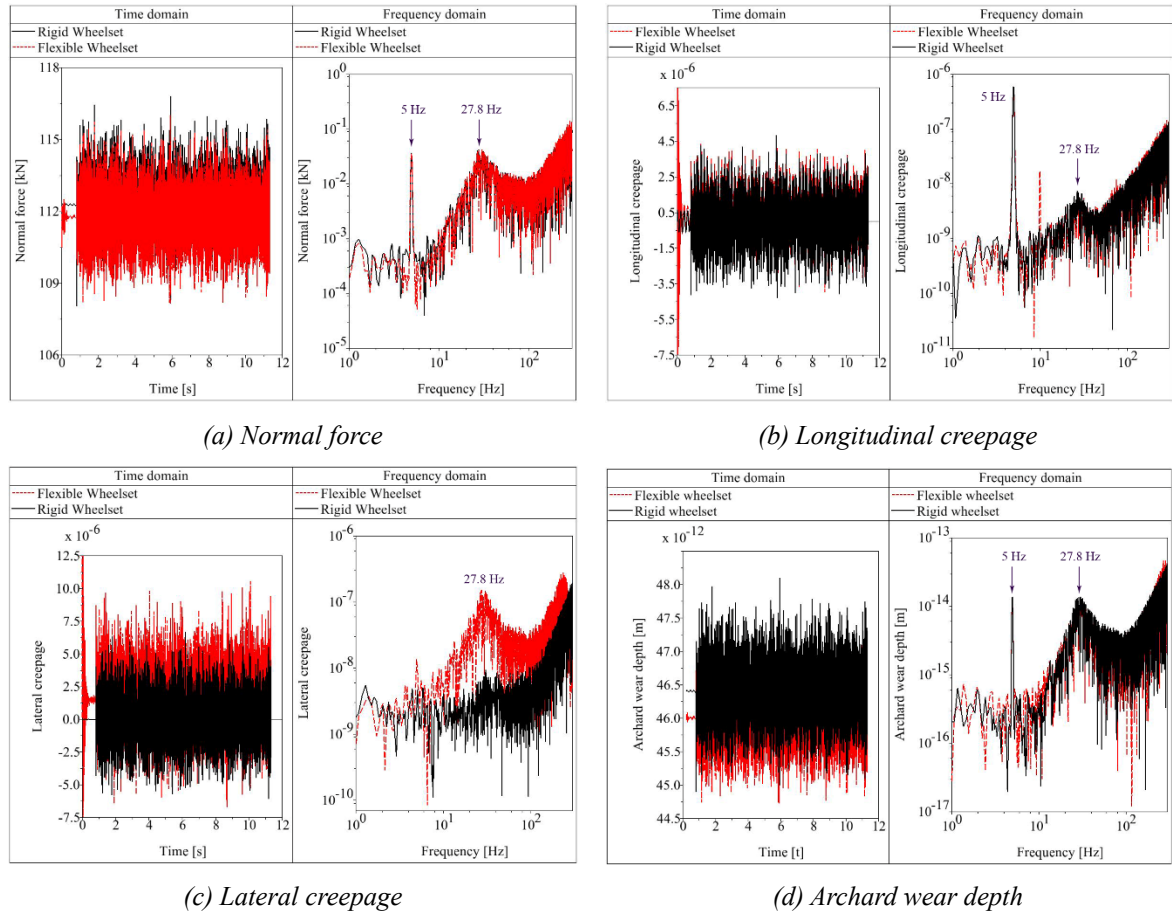


Figure 6-7 Contact responses excited by vertical track irregularity (white noise) on a **straight** track with a comparison between rigid and flexible wheelsets: (a) Normal force, (b) Longitudinal creepage, (c) Lateral creepage, and (d) Archard wear depth

6.4.2 Curved track with a small radius

A case of a curved track with a very small radius of 100 m is presented here. At a speed of 50km/h, with vertical track irregularity of white noise as the excitation, the wheelset is run on a curve of radius 100 m for 50 revolutions. The respective results are shown in Figure 6-8. As can be seen, the peak normal force of the flexible wheelset is slightly lower than that of the rigid wheelset. However, the frequency spectrums for both longitudinal creepage and lateral creepage present an obvious discrepancy between rigid and flexible wheelsets. From around 40 to 300 Hz, the frequency spectrum amplitude of the flexible wheelset is bigger than that of the rigid wheelset. Most importantly, there appears a distinct peak at around 50 Hz in the frequency spectrum of both longitudinal creepage and lateral creepage. It can be seen from Table 6-2 that, 50 Hz corresponds to the torsional modal frequency of the flexible wheelset, and the first 6 modal frequencies are just within the range

from 40 to 300 Hz. Consequently, it is believed that the torsional mode of the flexible wheelset is effectively excited to fluctuate the contact parameters in this case, which contributes to the resonant peak at 50 Hz. The first 6 modes of the flexible wheelset are also excited contributing, more or less, to the discrepancy in the frequency spectrum from around 40 to 300 Hz. As expected, there appears an obvious resonant peak in the frequency spectrum of the Archard wear depth at the wheelset torsional modal frequency. Given this result, a natural question arises: why can the torsional mode be effectively excited to dominate the contact responses in the case of a small radius curve, while it cannot be for a straight track? To answer this question, further investigation is carried out on the adhesion state of the contact, which is shown in Figure 6-9.

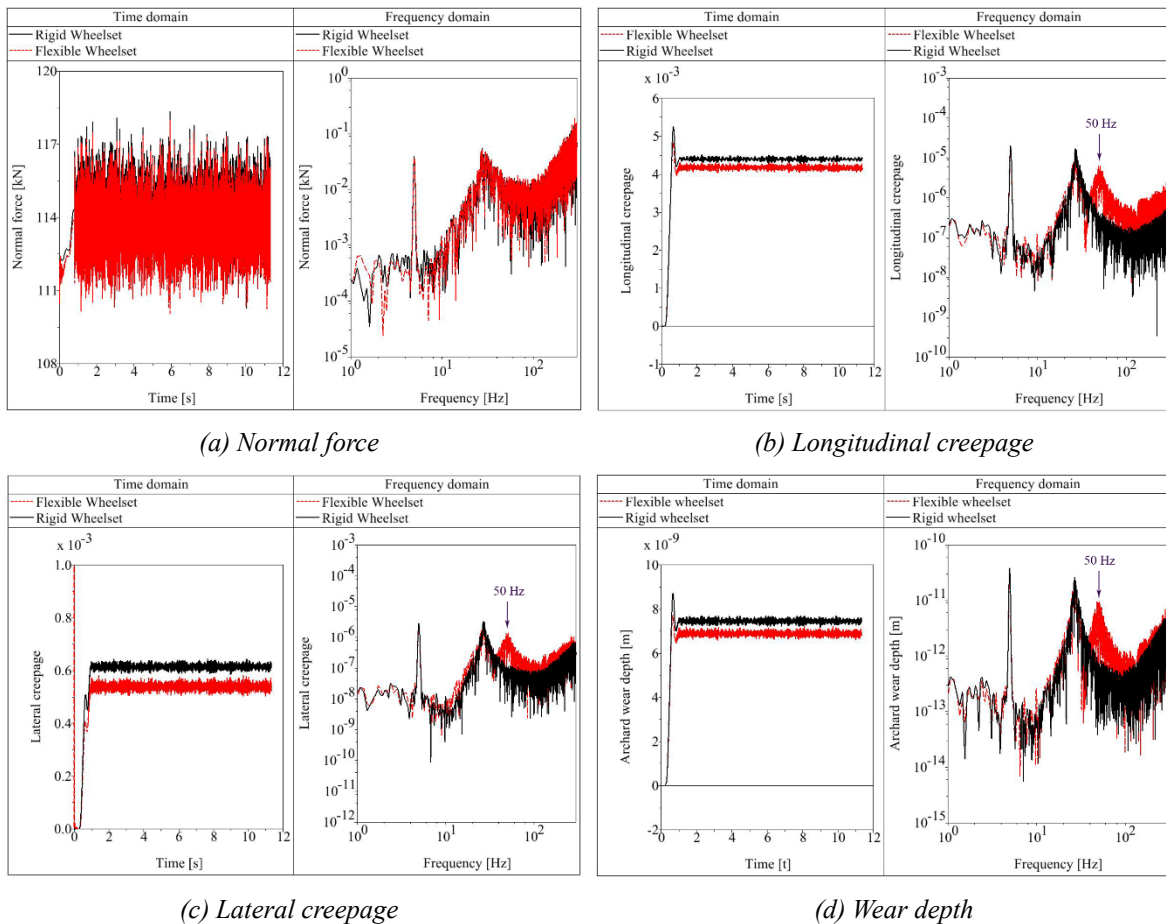


Figure 6-8 Response of contact parameters excited by vertical track irregularity (white noise) on a curve (radius 100 m): (a) Normal force, (b) Longitudinal creepage, (c) Lateral creepage, (d) Archard wear depth

As can be seen in Figure 6-9, during the curve negotiation, the adhesion coefficient has reached 0.3, which is the adhesion limit in this case. The saturation of adhesion is another indicator. The value of 1 means that no further creep forces can be transmitted. It is clear that the contact patch experiences a stick-slip vibration in a nearly saturated adhesion state. This stick-slip vibration at the contact patch can effectively excite the wheelset torsional mode to fluctuate the contact parameters (especially the creepages) at the wheelset torsional modal frequency, which will finally result in the oscillation of the contact wear at the same frequency.

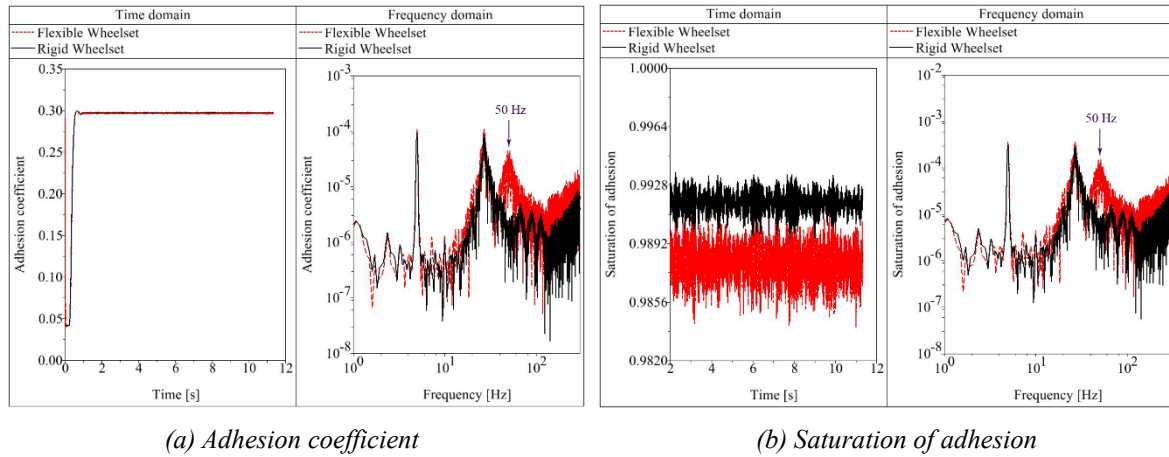


Figure 6-9 Adhesion state of the contact on a curve (radius 100 m)

Apart from the situation of small curve negotiation, high traction torque can also lead to a state of saturated adhesion. It has been found through more simulation that for a powered wheelset with high traction torque, if the contact adhesion limit is reached, the wheelset torsional mode will also be excited by the stick-slip vibration. The excited torsional vibration can also fluctuate the contact responses, and thereby initiate polygonal wear at the wheelset torsional modal frequency. This finding is in accordance with reports by Frohling, who found that the wheel polygonization occurring in an electric locomotive in South Africa was caused by the torsional vibration of the wheelset shaft [95]. However, the situation of high traction torque is more complicated as it is related to the adhesion control.

6.5 Influence of wheelset flexibility on railway wheel polygonization

6.5.1 Prediction of the evolution of wheel polygonization

The evolution of wheel polygonization is simulated using the prediction program described in Chapter 3. It was found that, a continuous excitation with a fixed frequency (track irregularity or sleeper passing frequency, etc.) that can fluctuate the contact parameters (normal force, creepages, etc.) in the same frequency, will cause a corresponding order of the wheel polygonization to develop, according to Equation (6-4).

$$\text{Order} = \frac{\text{Perimeter}}{\text{Wavelength}} = \frac{\text{Frequency}}{\text{Speed}} \times \text{Perimeter} \quad (6-4)$$

As an example, assigning a vertical track irregularity with a single sinusoidal wavelength of 1/10 wheel perimeter, the corresponding developed order of the wheel polygonization will be exactly 10. Figure 6-10 shows the resulting development of wheel polygonization for a wheelset running on a straight track. The main simulation parameters for this example are speed 70 km/h, wavelength 0.3925 m (perimeter/10), excitation amplitude 0.1mm, simulation iterations 10, amplification coefficient 1e6, and total running distance 39,250 km.

This is the fundamental relationship between the excitation frequency and the developed order of the wheel polygonization. It can be extended to the situation of multiple excitation frequencies, which means fluctuation

with multiple frequency components occurring in contact parameters can lead to multiple corresponding orders to develop. The prime interest of this paper lies in whether the wheelset flexibility plays an important role in the formation and the growth rate of the wheel polygonization. The idea is that, under the excitation of white noise that has a wide range of frequency components, if some flexible wheelset modes can be successfully excited to fluctuate the contact parameters at the wheelset flexible modal frequencies, and further the circumferential wheel wear at the same modal frequencies, these wheelset flexible modes will result in the development of the corresponding orders of the wheel polygonization. By comparing the evolution of wheel polygonization between rigid and flexible wheelsets, the influence of the wheelset flexibility can be identified.

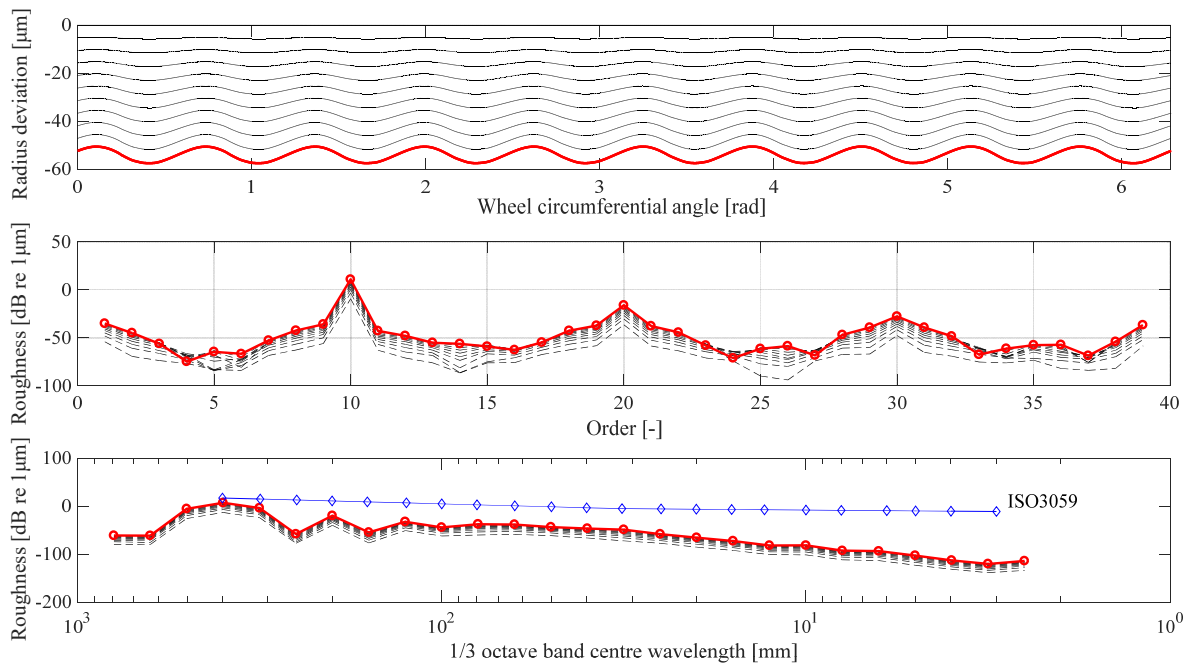


Figure 6-10 Development of wheel polygonization excited by a vertical track irregularity with a single sinusoidal wavelength of 1/10 wheel perimeter

6.5.2 Case studies

The comparisons were carried out for a straight track and 4 curved tracks with radii of 1200 m, 900 m, 600 m, and 300 m respectively. The running speed of 70 km/h and the running distance of 39,250 km are set for all scenarios. But one exception is that, for the curved track of radius 300 m, only 27,475 km is run, as the wheel-rail contact detachment will occur for further running due to large wheel OOR developed. Higher frequencies above 300 Hz of the circumferential wheel wear is filtered as the investigated flexible mode frequencies are below 300 Hz.

White noise with a flat-PSD, which is used as the input for investigating the contact responses, is no longer suitable for checking the development of wheel polygonization. Because given the same amplitude, a sinusoidal excitation with higher frequency has more energy than that with lower frequency, so that the higher orders excited by high-frequency excitations are easier to develop faster than the lower orders excited by low-

frequency excitations if a flat-PSD is used as the excitation. Consequently, the flat-PSD has to be modified to obtain a meaningful result when comparing the growth rate of different orders of wheel polygonization. The principle is that the energy should be equally distributed in the frequency domain, which can be guaranteed by Equation (6-5).

$$P(f) \times f^2 = \text{constant} \quad (6-5)$$

where: f is the distance frequency, $P(f)$ is the PSD amplitude at frequency f . Assuming: $P(1) \times 1^2 = 1$, Equation (6-5) can be written as:

$$P(f) = 1/f^2 \quad (6-6)$$

Then a random signal in the distance domain can be generated by $P(f)$, but should be scaled to adapt for a reasonable track irregularity. In this case, a coefficient of $1e-12$ is used. The resulting vertical track irregularity is shown in Figure 6-11. Note that the signal shown has been transformed to the time and frequency domain with a speed of 70 km/h. With this kind of vertical track irregularity as the excitation, the simulation results are shown in Figure 6-12. By comparing all scenarios in Figure 6-12, the influence of wheelset flexibility can be interpreted in two aspects: the growth rate and the developed orders.

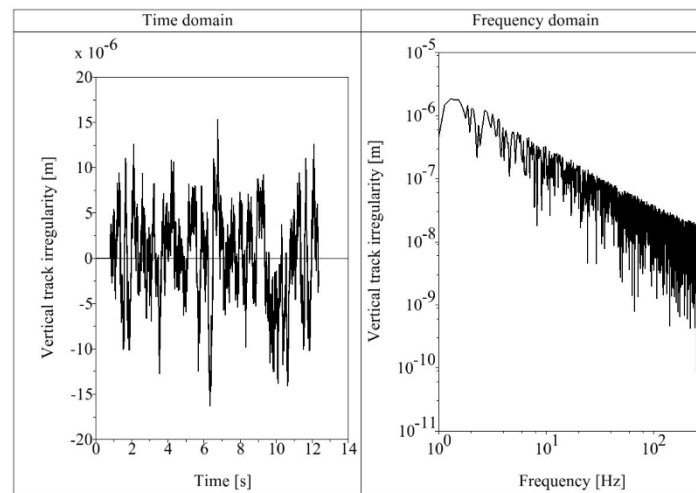


Figure 6-11 Vertical track irregularity generated by white noise with equally-distributed energy

In terms of the growth rate of the wheel polygonization, firstly, there is a general trend that, the smaller the curve radius is, the faster the development of the wheel polygonization will be, and the more obvious that the wheelset flexibility can influence the wear. Secondly, for curved tracks, the wheelset flexibility has a distinct effect on accelerating the growth rate for most orders above the 9th. Note that the flexible modal frequency of the wheelset starts from 50.05 Hz (see Table 6-2), and the corresponding frequency of the 9th order at the speed of 70 km/h is 44.6 Hz, according to Equation 6. It is naturally believed that the flexible modes of the wheelset are attributable to the accelerated growth of orders above 9th.

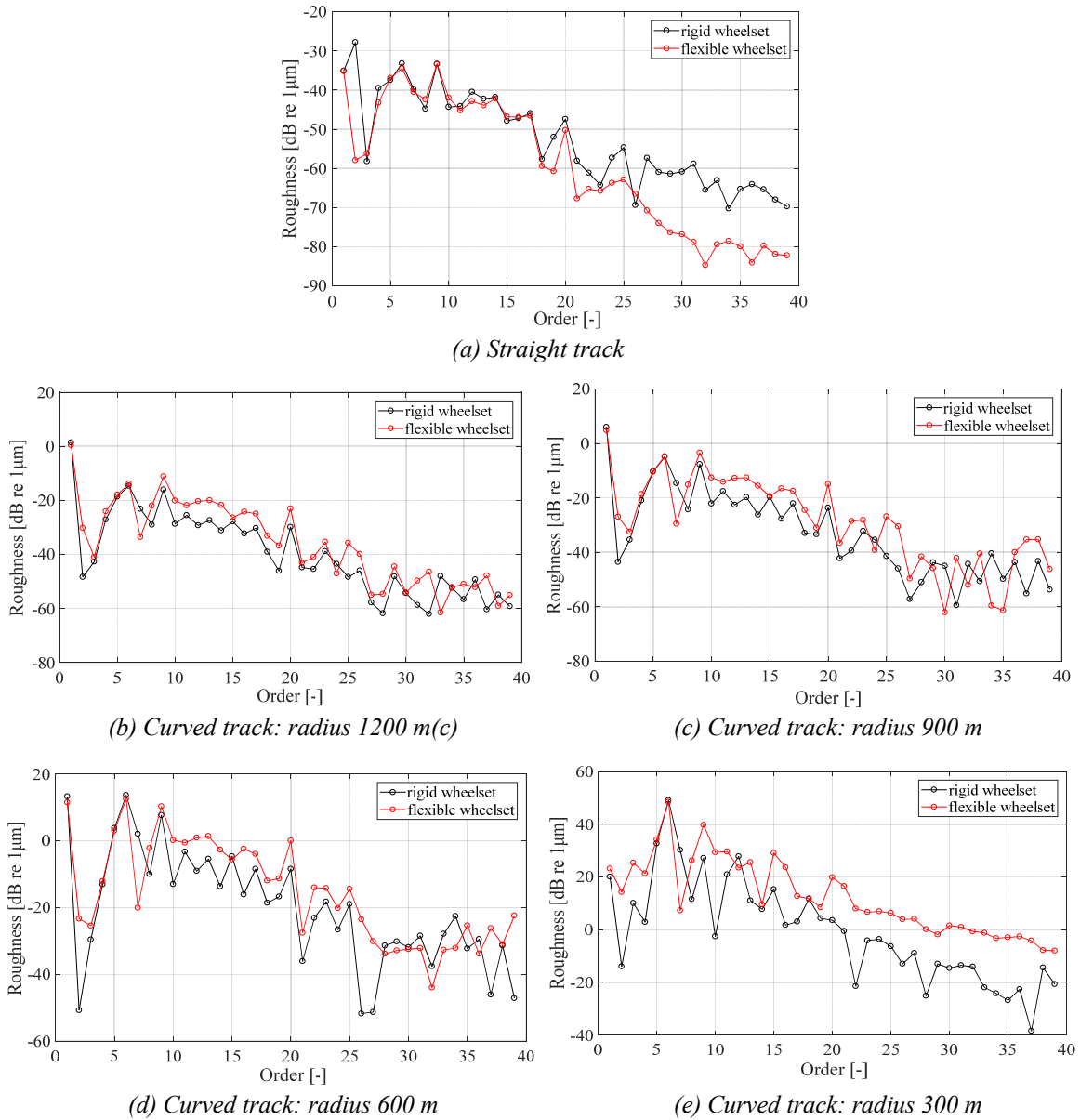


Figure 6-12 Development of wheel polygonization excited by vertical track irregularity (white noise with equally-distributed energy), with running distance of 39,250 km on (a) straight track, (b) curved track (radius 1200 m), (c) curved track (radius 900 m), (d) curved track (radius 600 m), and with running distance of 27,475 km on (e) curved track (radius 300 m)

With respect to the developed orders, firstly, there is always a development in the 1st order because of the wheelset imbalance introduced from the FE modelling of the wheelset (see Section 6.2). This is an artefact of the modelling method. However, it is still reasonable as the wheelsets will always have an imbalance in reality. Secondly, the developed order of 6 appearing in all the scenarios (for Figure 6-12 (a) to (e)) is due to the vertical rigid body mode of the wheelset & sleeper with respect to the ground. The frequency of this mode is 27.8 Hz, determined by the mass of wheelset & sleeper and the vertical stiffness of the sleeper. The corresponding order of 27.8 Hz at the speed of 70 km/h is 5.62. As 5.62 is closer to integer 6 than integer 5, the order 6 is developed dominantly followed by the order 5 that is slightly smaller. This dominant order will change with the speed

correspondingly, according to Equation (6-4). In addition, it should be noted that the 6th order is always the most dominant for all scenarios. This is because the vertical rigid mode of wheelset & sleeper is most readily excited by a vertical excitation as in this case. Of course, the wheelset flexibility is not responsible for the development of the 6th order, as it is due to a rigid mode in this case.

Thirdly, another development in the 9th order apparent in all the scenarios is rather confusing. Because on the one hand, this particular order is also dominant indicating there must be a significant driver, however, on the other hand, this order will not change correspondingly with speed, meaning that it cannot be explained by the fixed-frequency mechanism, as Equation (6-4) is not satisfied any more. The reason for the development of this order is not apparent.

Finally, the primary focus of the work presented here is to check whether any flexible modes of the wheelset can be significantly excited to cause some orders to grow. Knowing that the first 3 flexible modal frequencies are 50.05 Hz, 71.305 Hz, and 136 Hz, the corresponding orders at a speed of 70 km/h are 10.1, 14.4, and 27.5 respectively. However, there are no obvious peaks that can be found at the position of these orders, meaning that the wheelset flexibility does not contribute to the wheel polygonization in these scenarios in Figure 6-12. However, in the case of a curved track with a small radius (100 m) illustrated in Section 6.4.2, the torsional mode of the wheelset is found to be effectively excited. Based on this finding, further simulation is carried out to check the effect of the torsional mode on the development of wheel polygonization. The speed is set to 50 km/h, and the running distance is set to only 2,355 km to avoid contact detachment in the simulation due to extensive wear. The result is shown in Figure 6-13 below.

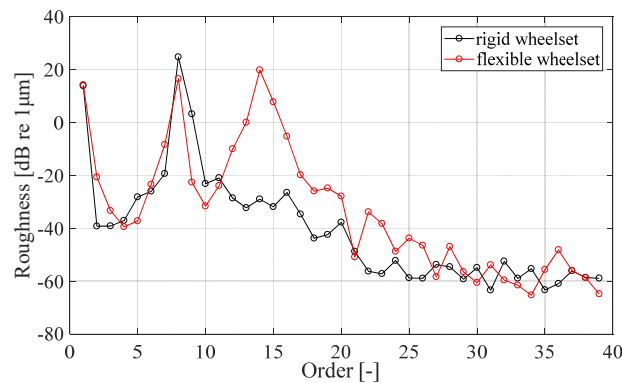


Figure 6-13 Development of wheel polygonization excited by vertical track irregularity (white noise with equally-distributed energy) with a running distance of 2,355 km on a curved track (radius 100 m)

The order that is expected to develop due to the torsional mode frequency 50.05 Hz at a speed of 50 km/h is $50.05/(50/3.6)/(2 \times \pi \times 0.625) \approx 14$. In Figure 6-13, it can be clearly seen that the 14th order of the wheel polygonization is dominantly developed in the presence of wheelset flexibility, compared to the rigid wheelset. More simulation shows that Equation (6-4) is satisfied when the speed changes. So it is confirmed that the torsional mode of the wheelset is the reason for the formation of the 14th order in this case of an extremely small curve radius. In addition, the development of the 8th order persists because of the vertical rigid mode of wheelset & sleeper, which has been explained before (noting that the speed is 50 km/h for this time).

6.6 Summary

This chapter reports on research investigating the influence of wheelset flexibility on polygonal wear of railway wheels. Although the results presented here are from a locomotive wheelset, simulation has also been carried out for the wheelset of a high-speed train (350 km/h) using the same method. It turns out that the underlying phenomena are similar but with differences being in the maximum frequencies considered and more flexible modes (the 3rd and 4th bending mode, in-phase umbrella mode, etc) involved. In addition, another finding of less importance is that the 2nd wheelset flexible mode is able to be excited by lateral rail irregularity which can drive fluctuating lateral creepage, but the excited mode has limited influence on the polygonal wear. Based on all the results obtained, some general conclusions can be drawn as follows:

- (1) The influence of wheelset flexibility on the development of railway wheel polygonization is complicated because the results strongly depend on specific conditions. All the investigated wheelset flexible modes (the torsional mode, the 1st bending mode, the 2nd bending mode and the umbrella mode) are found to influence the contact responses in very different ways and have different effects on the wheel wear. By further considering that in reality the attachment constrains (gearbox, motor suspension tube, or brake equipment) would more or less prevent the wheelset flexibility from being excited, it is believed that the wheelset flexibility cannot dominate the railway wheel polygonization in a general sense, unless some prerequisites are fulfilled to provide a suitable environment for the wheelset flexibility to be effectively and continually excited to fluctuate the contact responses, and thereby initiate wheel polygonization.
- (2) The wheelset flexibility tends to attenuate the normal force slightly, but can always increase the lateral creepage significantly. The normal force is not easy to be influenced by any flexible wheelset modes in the frequency domain. The lateral creepage is sensitive to the 1st bending mode and the umbrella mode under vertical excitation and sensitive to the 2nd bending mode under lateral excitation. The longitudinal creepage is mainly sensitive to the torsional mode, although it can also be affected by other flexible modes but not so apparently.
- (3) When the contact adhesion is nearly saturated, which can happen on track with small curve radii or due to large traction torque, the stick-slip vibration occurring at the contact patch can effectively excite the wheelset torsional mode to fluctuate the contact parameters and therefore the wheel wear. If this situation persists for a long time, the development of the wheel polygonization can be expected. The excited order will be exactly determined by the wheelset torsional modal frequency and vehicle speed.

Chapter 7 Influence of track flexibility on railway wheel polygonization

7.1 Introduction

Track flexibility is an essential factor influencing the wheel-rail contact responses and therefore the wheel/rail wear. Consequently, track flexibility is always a necessary element to be included in the MBS model for the issue of wheel/rail wear. Research can be found to take the track flexibility into account when investigating the transverse wheel wear [105] and the rail roughness [106]. Few reports can be found to associate the track flexibility to the problem of railway wheel polygonization. However, in recent years, some researchers proposed that the bending modes of the rail section between two adjacent wheelsets of the same bogie (local rail bending modes) could be the cause for the high-order wheel polygonization of high-speed trains in China. Specifically, the third local rail bending mode was suspected to be excited significantly, leading to a corresponding high-order OOR of the high-speed train [35]. This is an innovative perspective to explain the mechanism of the railway wheel polygonization. To verify this hypothesis, both simulation and experiment are being carried out.

To realize the track flexibility in simulation, a variety of different types of flexible track can be found in the literature. The methods of modelling flexible track depend on whether the MBS model is established with a self-developed program or commercial software. For the self-developed program, the rail is usually built as beam (Euler beam or Timoshenko Beam) supported by several layers (generally up to 3 levels) of track suspensions, for example, see the work of Zhai and Ling [104,107]. The sleepers are normally built as rigid masses discretely distributed beneath the flexible rail. The self-developed flexible track is controllable, but the complexity is limited by the requirements for the coding as well as computational resources and performance. If the MBS is built by commercial software, the modelling of the flexible track can be more versatile via the integration between the FE model and the MBS environment. Any components of the track can be built as a flexible body with arbitrary complexity in many MBS software. Nevertheless, the accuracy is depending on the internal algorithm of the commercial software.

This chapter evaluates how the track flexibility influences the railway wheel polygonization, especially whether the local rail bending modes can be excited successfully to dominate the wheel-rail contact responses and therefore the wheel polygonization. After introducing the methods for modelling flexible track in Simpack, the vehicle/flexible track MBS model is built based on the Simpack FTR (Flexible Track Reference) method. Afterwards, a comparison is conducted between three kinds of flexible track with differing complexity. Finally, simulations are carried out to check the influence of the track flexibility on polygonal wear of wheels, with some preliminary conclusions obtained.

7.2 Methods for modelling flexible track in Simpack

In Simpack, the track flexibility can be realized with a co-running sleeper following the wheelset or a section of flexible track mounted on the ground. Using a co-running sleeper is a simple way to simulate track flexibility, which is highly efficient in computing time. However, to simulate the track flexibility more accurately, the flexible track mounted on the ground has to be employed, which is more realistic. Especially as in this chapter, an important objective is to check whether the local rail bending modes can be excited successfully to dominate the wheel OOR, which can only be investigated with the mounted flexible track.

7.2.1 Direct and indirect methods

Generally, the mounted flexible track can be built directly with the FlexTrack module provided by Simpack, using the FTR (Flexible Track Reference) file (ASCII format) to configure the flexible track. This is the default direct method to build the mounted flexible track in Simpack. To facilitate the following description, it is called the ‘FTR method’. However, some other indirect methods were also proposed by researchers. For example, the so-called ‘dummy method’ was proposed by Gonzalez and Blanco [108,109] who use some auxiliary elements (kinematic constraint, moved markers and dummy rail) to couple the wheel and the flexible track. In [17] the flexible track was realized via the SIMAT (Simpack-Matlab) exchanging data between Simpack and Simulink where the flexible track is built as a self-developed model, which can be simply abbreviated as ‘SIMAT method’. The example of the direct FTR method and two indirect methods (namely dummy method and SIMAT method) found in the literature are shown in Figure 7-1, Figure 7-2 and Figure 7-3, respectively.

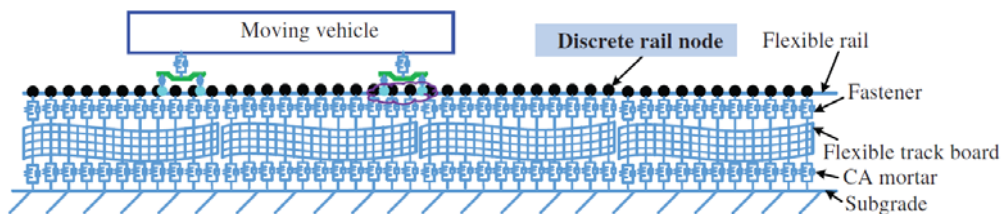


Figure 7-1 An example of the FTR method [110]

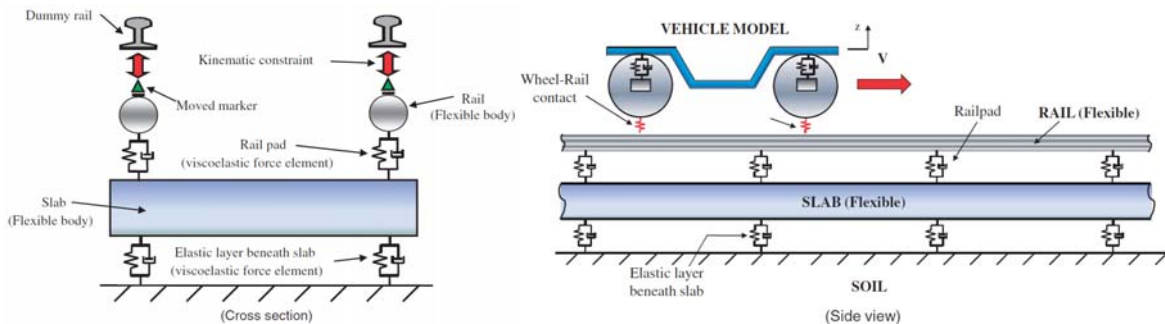


Figure 7-2 An example of the dummy method [109]

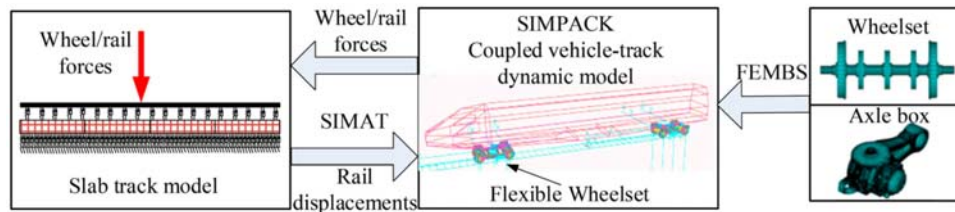


Figure 7-3 An example of the SIMAT method [17]

Both the FTR method and the dummy method have been realized by the author with Simpack scripts used to complete the building process automatically. It was found that it is unavoidable to produce some unrealistic problems with the dummy method due to the auxiliary elements added artificially. For example, the constraint type at both ends of a rail has a significant influence on the calculation results, which was also discussed by Ji [110]. In addition, the SIMAT method is relatively complicated. After all, the indirect methods proposed by researchers are not provided by Simpack directly, and the verification of these indirect methods is a critical issue. Consequently, this chapter only introduces the default FTR method on which the conclusions are based.

7.2.2 The FTR method

The FTR method [48] enables users to model finite element-based flexible track foundations for railway vehicles. The user can set up Flexible Bodies of a special FlexTrack type, which are automatically connected to the rails of a railway vehicle model when the vehicle passes the Track section in which the Flexible Body is located. The flexible section is fixed in space, without movement with the vehicle. It may follow a curved and superelevated track with vertical slopes. The track flexibility is represented by a modal reduction contained in one or multiple Flexible Body Input (.fbi) files. In Simpack, by means of a configuration file (FTR file), the user may connect different parts coming from multiple .fbi files and add local springs and dampers, which are integrated into the flexible representation. Additionally, the user may connect Force Elements and other Modelling Elements to any master node of the Flexible Body.

The workflow for the integration of flexible track based on FTR method is illustrated in Figure 7-4. The flexible components (e.g. the rail) of the track are built in FE software. After defining the master nodes and generating the substructure, the fbi file is prepared by Simpack FBI generation. The FTR file is responsible for connecting the fbi files to the FlexTrack body created in Simpack rail, which is the key in this workflow to integrate the FE model to the MBS environment. The FTR file is written in ASCII format following the script grammar defined in Simpack. It contains all the information required for the integration of flexible track, including the specified fbi files, the position and orientation of the flexible track section(s) in space, the positions of the coupling nodes, the position of additional extrapolation nodes, the modal (Rayleigh) damping values that will be applied to the flexible section(s), additional spring and damper elements at arbitrary nodes, plot elements, and other supplementary configuration.

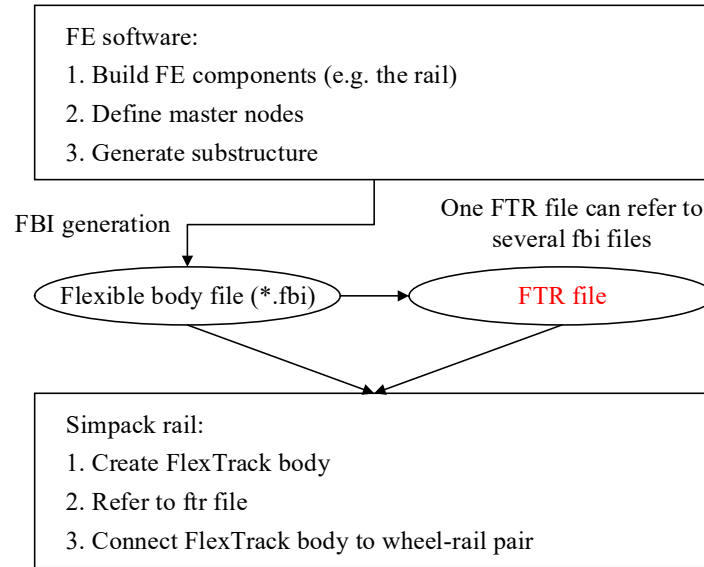


Figure 7-4 Integration of flexible track based on FTR method

7.3 Modelling of flexible track based on the FTR method

In this chapter, only the ballasted track is considered. The sketch map of the ballasted flexible track is presented in Figure 7-5. The flexible rail is prepared in Abaqus. It could be modelled as a beam or 3D rail. The sleepers are considered as rigid bodies. There are two layers of discrete suspensions: the rail pad suspension between the flexible rail and the rigid sleepers, and the ballast suspension between the rigid sleepers and the fixed ground. The two layers of suspension are built with bushing elements which have stiffness and damping for all 6 degree-of-freedom (DOF). However, only the suspension parameters in the lateral and vertical directions have a significant influence on the results here. The entire flexible track can be built in Abaqus and then imported to Simpack as a whole, or alternatively, only the flexible rail is built in Abaqus while leaving all other components to be built in Simpack directly. The latter method is adopted here because it is more efficient to use a Simpack script to model the repeated elements. The flexible rail is configured as a FlexTrack body via the FTR file. The FlexTrack body is then connected to the wheels in wheel-rail pairs. It is worth noting that all wheels must be in the same hierarchy of the vehicle MBS model so that all wheels can run on the same flexible track simultaneously.

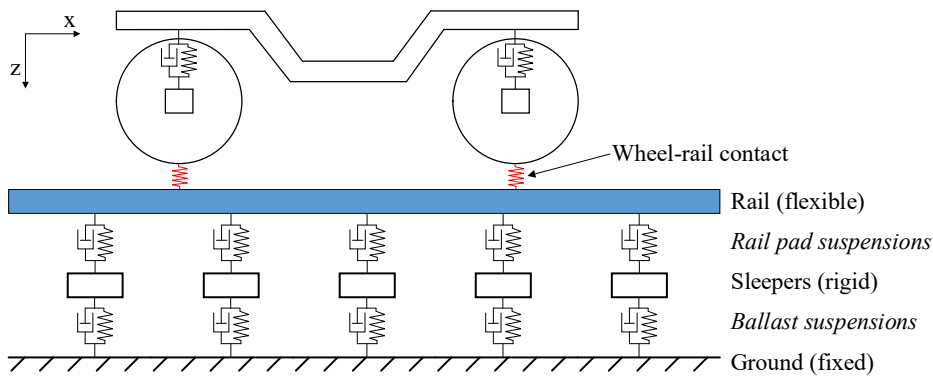


Figure 7-5 Sketch map of the ballasted flexible track

The workflow of building the flexible track based on the FTR method involves several steps (as shown in Figure 7-4): preparation of the FE model, FBI generation, the configuration of the FTR file, and connection of the vehicle to the FlexTrack. It is not practical to execute all the steps by hand operation, as it is time-consuming and not convenient for parametric analysis. As a result, several scripts are coded to make the process as automatic as possible, including Abaqus script, Simpack script, and Matlab script. However, the feasibility of automatic modelling with scripts can be determined by the complexity of the model. Depending on whether the rail is modelled as a beam or 3D rail, the scripts must be adjusted accordingly. If the rail is built as a beam, the modelling process is fully automatic with the script. If the rail is built as a 3D rail, some hand operations are inevitable.

Figure 7-6 shows the automatic modelling of a flexible track (beam rail) with scripts. There are three main steps: 1 prepare the flexible rail in FE, 2 configure the FTR file, and 3 configure the MBS model, with three scripts coded to realize the automatic modelling of the flexible track (beam rail) correspondingly. Note that in each script, only the main modelling process are listed. These three steps will be elaborated on one by one in the following sections.

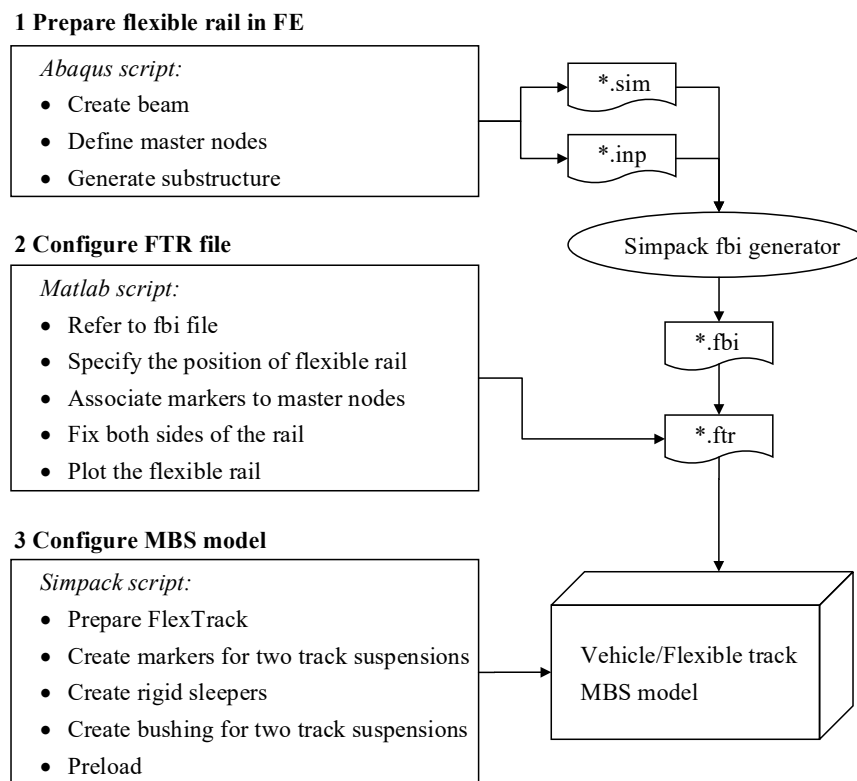


Figure 7-6 Automatic modelling of a flexible track (beam rail) with scripts

7.3.1 Preparation of the flexible rail in FE

If the flexible rail is modelled as a beam (Timoshenko beam), the modelling can be fully realized by the Abaqus script (written in Python code), so that it is easy to adjust all the parameters, such as beam length, the property of cross-section, meshing precision, and so on. If the flexible rail is modelled as a 3D rail, the modelling is

more complicated. The 3D geometry is built in SolidWorks, the meshing is implemented in Hypermesh to guarantee good meshing quality, and the substructure generation is finally conducted in Abaqus. With this procedure, different lengths of 3D rail have to be prepared separately.

After establishing the FE model of the flexible rail, the following task is to specify the master nodes used for generating the substructure that is the reduced FE model to be imported into Simpack. The master nodes of a flexible body are the interface nodes connecting other components in Simpack. The selection of master nodes for 3D rail is shown in Figure 7-7. Note that in the case of the 3D rail, the FE nodes cannot be selected as the master nodes directly. The solution is to define a reference node coupled with adjacent FE nodes (see the purple nodes in Figure 7-7), and then select the reference node as the master node, so that the deformation of the reference node can influence the adjacent FE nodes as a whole, which is more realistic.

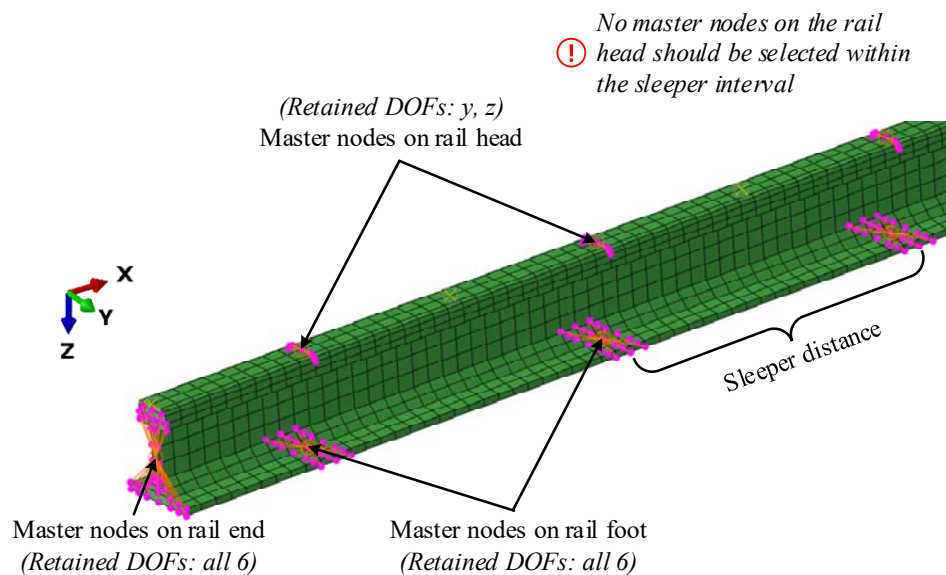


Figure 7-7 Selection of master nodes for 3D rail

For the rail end, the master node is specified for the fixation at both ends of the rail. For the rail foot, master nodes must be selected at the positions of sleepers, as they will be used to connect to the sleepers through suspensions. The master nodes on the railhead, which are used to interpolate with the wheel positions during the vehicle passing by, should be specified corresponding to those on the rail foot. No more master nodes on the railhead should be selected within the sleeper interval because it is found that if more master nodes are defined between two adjacent sleepers, the multiple frequencies of the sleeper passing frequency will become predominant. For example, assuming f as the sleeper passing frequency, if one more master is specified within the sleeper distance, $2f$ becomes more dominant than f . In a similar fashion, if two more masters are added within the sleeper interval, $3f$ becomes the most dominant one. This phenomenon is obviously not realistic, which is probably due to the algorithm of interpolation between the wheel positions and the flexible rail. This issue found in Simpack was also found in VI/Rail. The common solution for handling this issue is not selecting any master nodes within the sleeper interval, which is also applicable to the beam rail. The selection of master nodes for the beam rail is shown in Figure 7-8, which is much simpler than that for the 3D rail.

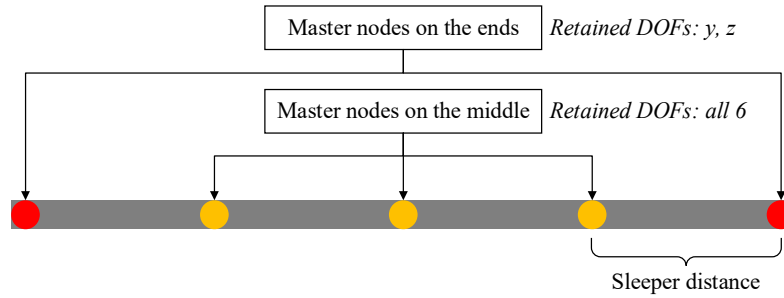


Figure 7-8 Selection of master nodes for beam rail

The retained DOFs of the master nodes is sensitive to the type of flexible rail. For the 3D rail, the retained DOFs of the master nodes on the railhead are y and z , and those on the rail foot and rail ends are all six DOFs. While for the beam rail, the retained DOFs of the master nodes on the ends are y and z , and those on the middle are all six DOFs. After configuring the master nodes, the FE model of the flexible rail is solved for modal analysis and substructure analysis in sequence. For the mode analysis, all retained DOFs are specified as the constrained DOFs so that the constrained modes of the flexible rail can be extracted for the next step of substructure generation. The substructure generation adopts the ‘Craig-Bampton’ method [103] which is a method for reducing the size (degrees of freedom) of the FE model to integrate the flexible model (known as a superelement) into the MBS software. The generated files are *.sim and *.inp, both of which are then used to generate the Flexible Body Input file (*.fbi) via Simpack fbi generator. The prepared fbi file of the flexible rail is then ready to be imported to Simpack by configuring the FTR file.

7.3.2 Configuration of the FTR file

The FTR file is in ASCII format and can be edited by any text processor. The configuration of the FTR file is here fully controlled by a Matlab script following the FTR grammar. The main tasks are to configure the flexible rail to the correct position in Simpack and to associate the master nodes of the FE model to the markers in Simpack. In addition to the master nodes, several additional extrapolation nodes are needed outside of the actual flexible rail to ensure that the reference markers of the rail profile extrapolate properly before and after the movement on the flexible section. In addition, both ends of the flexible rail are fixed with forces of very high stiffness. An example of the FTR file for a 3D rail is illustrated in Figure 7-9, with the comments in blue demonstrating some main keywords.

FTR file

```

se, Rail60_3D_21m.fbi, 0.0010, 0.0050, 20.0000, ... ! Refer to fbi file
n, 10001, 20.3000, -0.7530, 0.0000                ! Associate master nodes on rail head
n, 11001, 20.3000, -0.7530, 0.1760                ! Associate master nodes on rail foot
n, 12001, 20.0000, -0.7530, 0.0950                ! Associate master nodes on rail ends
n, 19001, 19.7000, -0.7530, 0.0000                ! Extrapolation nodes
k0,12001, , 1.0e+10, 1.0e+10, ...                 ! Fix rail end
pe,10001, 10002                                   ! Plot
.....

```

Figure 7-9 An example of FTR file

7.3.3 Configuration of the MBS model

The railway vehicle MBS model is generally built in a hierarchy of sub-models, to avoid repeated modelling of some components (e.g. wheelsets and bogie). However, in this case, to make sure that all the wheels are running on the same flexible track, the wheelsets must be built in the top level of the hierarchy where the flexible track is built. The solution is to build four dummy wheelsets to connect the flexible track at the top level and fix these dummy wheelsets to the actual wheelsets in the lowest level of the hierarchy, respectively. This solution is effective and efficient with minimal modification to the original structure of the vehicle MBS model. Afterwards, a FlexTrack body is built referring to the FTR file prepared above. Based on the FlexTrack body, the discrete rigid sleepers and the two layers of suspensions are built automatically with a Simpack script. As mentioned above, the modelling of sleepers and track suspensions are intentionally built in Simpack instead in Abaqus, as it is convenient to carry out parameter analysis on the track suspension properties in Simpack. Now the vehicle/flexible track MBS model is finished and ready for time integration or parameter analysis. The vehicle/flexible track MBS model with a section of a flexible 3D rail of length 21 m is presented in Figure 7-10. The purple nodes are the master nodes of the flexible rails serving as the interface nodes connecting the vehicle and the sleepers.

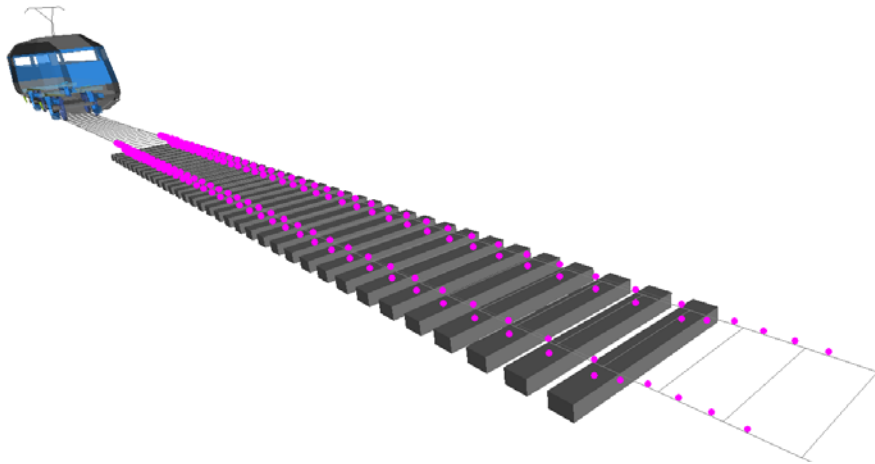


Figure 7-10 Vehicle/Flexible track MBS model

7.4 Comparison of tracks

As mentioned in Section 7.2, track flexibility can be realized in different ways in Simpack. To obtain the understanding of the essential feature of the flexible track, comparison is carried out between rigid track, co-running sleeper (Co-Sleeper), flexible track of beam rail based on FTR method (FlexTrack_Beam), and flexible track of 3D rail based on FTR method (FlexTrack_3DRail), to identify the difference between them. The test scenario is:

- The vehicle is the locomotive described in Section 5.4.1.
- The wheelset is built as a rigid body without considering the wheel OOR.
- The vehicle speed is 70 km/h running on a straight track.
- The simulation time is 2.5 s, and the sampling rate is 4000 Hz.
- The contact responses of wheel 1L are investigated.

For FlexTrack_Beam and FlexTrack_3DRail, the flexible section is 21 m long starting at 20 m in front of the locomotive centre, as shown in Figure 7-10. The property of the FlexTrack is listed in Table 7-1. The beam rail has the same rail cross-section property with the 3D rail. The suspension parameters of the Co-Sleeper are listed in Table 7-2. Note that these parameter values are estimated via parametric analysis to equivalently match the FlexTrack mounted on the ground. The vertical equal-energy-distributed white noise shown in Figure 6-11 is adopted as the track excitation to check the frequency response of the tracks. The normal force and the lateral creepage are observed as the indicators for they are the most influential contact responses influencing the instantaneous wear depth. The comparative results of the normal force and the lateral creepage for different tracks are presented in Figure 7-11 and Figure 7-12, respectively, in both the time domain and frequency domain.

Table 7-1 FlexTrack properties

Track properties	Value	Unit
Rail density	7850	kg/m ³
Young modulus	2.1e11	Pa
Shear modulus	8.1e10	Pa
Poisson's ratio	0.3	-
Sleeper: mass	308	kg
Sleeper: moment of inertia I _{xx}	128	kg·m ²
Sleeper: moment of inertia I _{yy}	10	kg·m ²
Sleeper: moment of inertia I _{zz}	128	kg·m ²
Sleeper distance	0.6	m
Rail cross section: area	7.84e-3	m ²
Rail cross-section: moment of inertia I _{zz}	5.34e-6	kg·m ²
Rail cross-section: moment of inertia I _{yy}	3.31e-5	kg·m ²
Rail cross section: torsional constant	3.85e-5	kg·m ²
Rail pad stiffness: vertical	120	MN/m
Rail pad stiffness: lateral	30	MN/m
Rail pad damping: vertical	75	kN·s/m
Rail pad damping: lateral	60	kN·s/m
Ballast stiffness: vertical	150	MN/m
Ballast damping: vertical	58.8	kN·s/m

Table 7-2 Estimated suspension parameters for Co-running sleeper

Parameters	Value	Unit
Vertical stiffness	350	MN/m
Lateral stiffness	30	MN/m
Rolling stiffness	350×0.75^2	MN·m/rad
Vertical damping	150	kN·s/m
Lateral damping	120	kN·s/m
Rolling damping	150×0.75^2	kN·m·s/rad

As can be seen in Figure 7-11, firstly, the result of the rigid track is very different from those of the flexible track. When considering the track flexibility, the normal force is attenuated significantly, and the P1 frequency is transferred to higher frequency from 189 Hz to 726 Hz that is more conformable to the reality. Secondly, the

result of the FlexTrack_Beam is nearly identical to that of the FlexTrack_3DRail by comparing the red curve with the green curve. This indicates that the simple rail beam can be used to replace the complicated 3D rail without loss of accuracy if the same rail cross-section property is guaranteed. Thirdly, the Co-Sleeper presents a good consistency of results with the FlexTrack_Beam by comparing the blue curve with the red curve, although there is still some difference in terms of the P1 and P2 amplitude. This implies that the Co-Sleeper can be adopted as an effective alternative to the FlexTrack in some cases, which can significantly reduce the complexity of the MBS model if the Co-Sleeper parameters can be estimated correctly. However, for some special issues, the Co-Sleeper will not be competent, for instance, if the uneven stiffness along the track should be involved. For the lateral creepage shown in Figure 7-12, the phenomena are similar to the normal force.

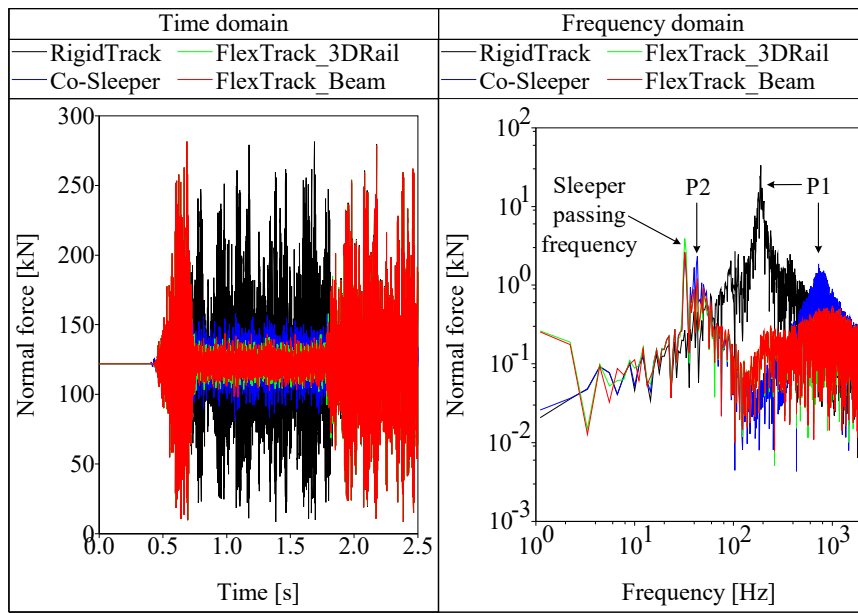


Figure 7-11 Comparison of the **normal force** for different tracks (Excitation: vertical equal-energy-distributed white noise)

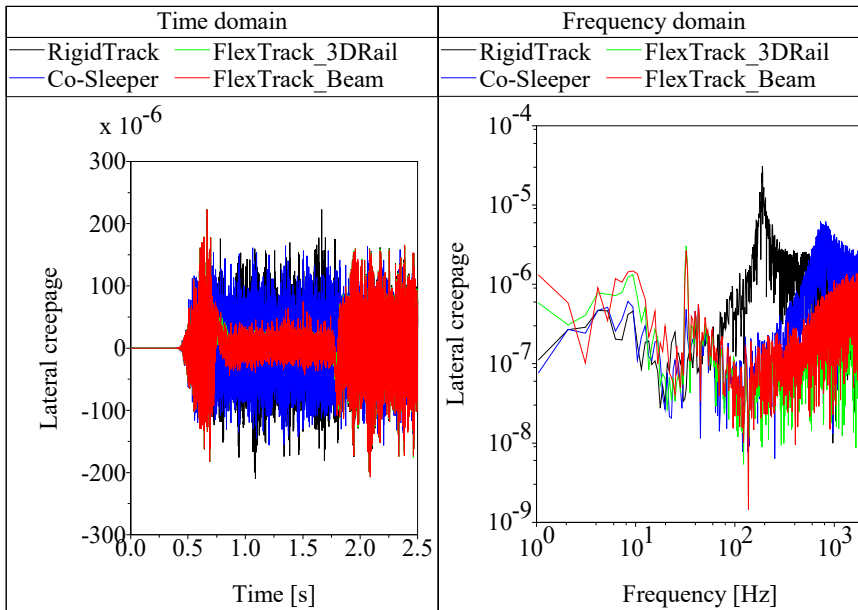


Figure 7-12 Comparison of the **lateral creepage** for different tracks (Excitation: vertical equal-energy-distributed white noise)

The computing time is also compared among the tracks, which is listed in Table 7-3. If using the FlexTrack_Beam as the reference, the computing time of the Co-Running sleeper is only 19% of that of FlexTrack_Beam, and the computation effort of the FlexTrack_3DRail can be triple to that of the FlexTrack_Beam. By comprehensively considering the accuracy between tracks, the FlexTrack_Beam is the best compromise that will be employed for the following analysis.

Table 7-3 Comparison of computing time for different tracks

Track type	CPU time (h:m:s)	Ratio
Rigid track	0:03:26	10%
Co-running sleeper	0:06:13	19%
FlexTrack: beam rail	0:33:35	Reference
FlexTrack: 3D rail	1:44:23	310%

7.5 Influence of track flexibility on polygonal wear

Following the idea in Chapter 6, if some modes of the track flexibility can be excited significantly to influence the wheel-rail contact in the frequency domain, the development of wheel OOR can be expected. The equal-energy-distributed white noise is adopted as the vertical excitation to investigate the frequency response of contact parameters in a wide range of frequencies. The scenario is the same as that described in the above Section 7.4 (Comparison of tracks). The white noise is the same as that described in Section 6.5.2. The flexible rail is built as a beam. The flexible track section is 60 m long starting at the position of 20 m in front of the vehicle centre. The simulation of the vehicle/flexible track system is shown in Figure 7-13. Note that the deformation of the master nodes of the flexible rail is amplified by 1000 times for clarity. The contact responses (normal force, longitudinal creepage, lateral creepage, and spin creepage) and the instantaneous wear depth for four wheelsets excited by the vertical equal-energy-distributed white noise are presented in Figure 7-14 and Figure 7-15 respectively, in both time and frequency domain. Note that the drastic fluctuation of all results in the time domain is due to the transition entering and leaving the flexible track. Only the results for the flexible track are involved in the calculation of the frequency spectrum.

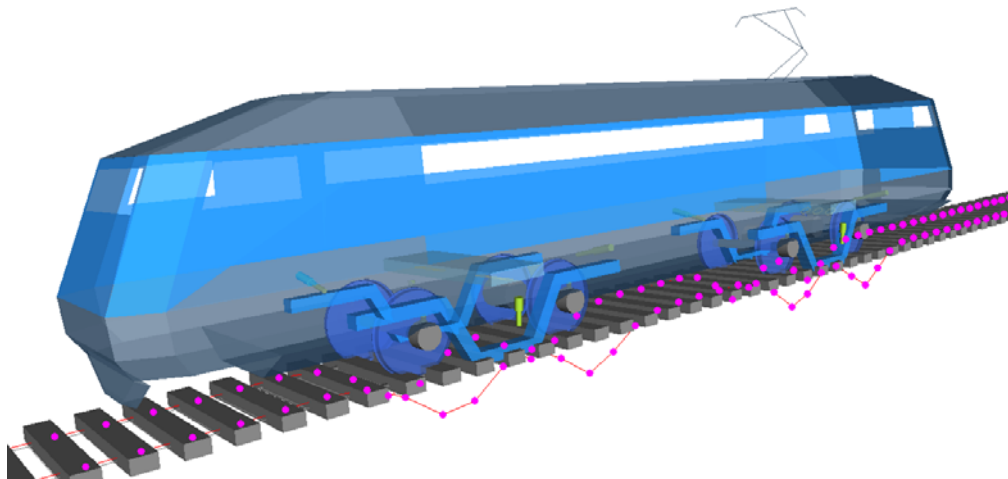


Figure 7-13 Simulation of vehicle/flexible track

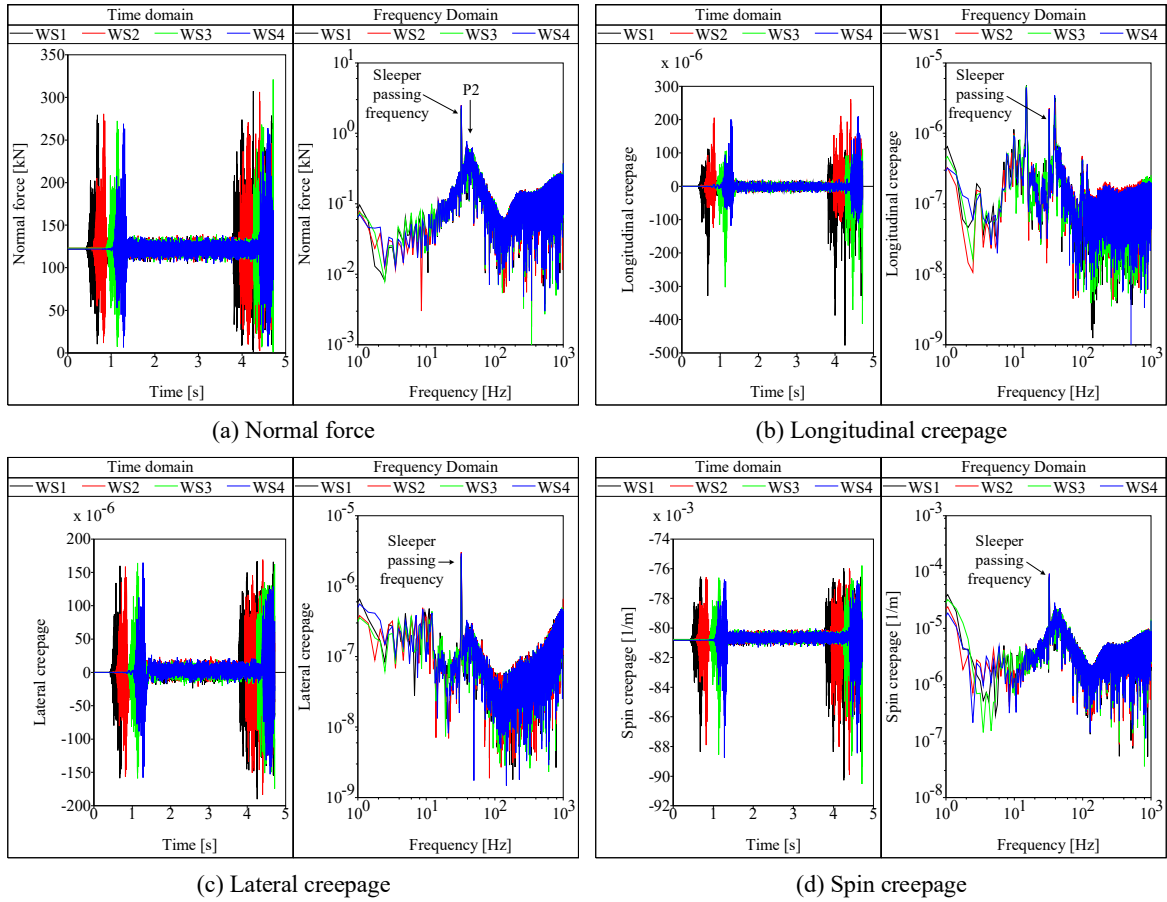


Figure 7-14 Contact responses of four wheelsets excited by vertical equal-energy-distributed white noise: (a) Normal force, (b) Longitudinal creepage, (c) Lateral creepage, and (d) Spin creepage

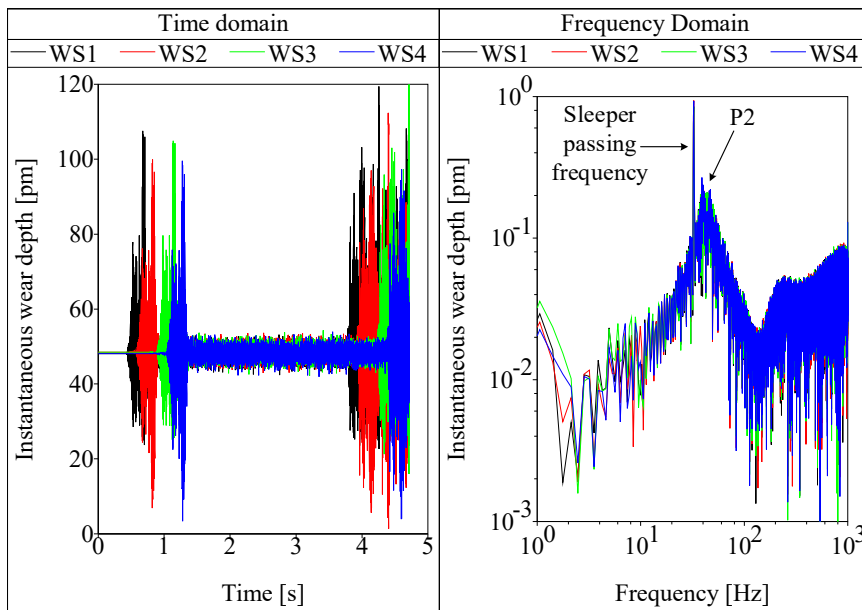


Figure 7-15 Instantaneous wear depth of four wheelsets excited by vertical equal-energy-distributed white noise

As can be seen in Figure 7-14, although different wheelsets have a time lag between each other, the frequency spectra are very similar. The most predominant feature of all the contact parameters in the frequency domain is that there is a constant sleeper passing frequency that is the same for all the wheelsets. This sleeper passing frequency is determined by the vehicle speed and the sleeper distance, which is 32.4 Hz in this case. The P2 frequency is also notable for all contact parameters, which is around 40 Hz in this case. Note that the frequency spectrum of the longitudinal creepage is slightly different from that of other metrics.

As the sleeper passing frequency and the P2 frequency are the dominant frequencies for all contact parameters, it is natural that these two frequencies will occur dominantly in the frequency spectrum of the instantaneous wear depth, just as Figure 7-15 shows. However, as only these two frequencies are found to be evident in all the frequency spectrum, the local rail bending modes are not excited successfully. Many attempts were conducted to excite the local rail bending modes by changing the simulation scenario (e.g. vehicle speed, track suspensions, excitation type, and so on), but none of them were successful. Another high-speed train running at 300 km/h was also tested, but the phenomena were still similar. It has to be concluded that the local rail bending modes cannot influence the railway wheel polygonization, at least with the simulation method described in this chapter, as the local rail bending modes themselves cannot be excited.

According to the simulation results obtained above, the main influences of track flexibility on the polygonal wheel wear are the sleeper passing frequency and the P2 resonance. No local rail bending modes are found to be excited. The development of wheel OOR can be expected with the prediction program described in Chapter 3. As has been discussed in Section 3.3.4.1 (The case of harmonic excitation), the sleeper passing oscillation will not produce visible OOR development if the vehicle has run for a long enough mileage, while the P2 resonance is able to contribute a corresponding OOR order to develop.

However, as has also been discussed in Section 3.3.4.2 (The case of random excitation), for the case of random excitation, the running distance must be long enough to obtain a convergent result for the prediction of wheel OOR development. As shown in Figure 3-10, the number of wheel turns necessary for a convergent result could be 1000 corresponding to a running distance of 3925 m. This raises an awkward issue regarding the computational effort in the presence of a mounted flexible track. The computing time is increased exponentially with the length of the mounted flexible track. For a 3925 m flexible track, the computing time could be dozens of days depending on the model complexity and the hardware. Moreover, the prediction of wheel OOR requires a number of iterations. If there are 10 iterations for a 3925 m flexible track, the total running distance is near 40 km, with which the computational effort is impractical for normal computers. To make the wheel OOR prediction to be feasible, the Co-Sleeper has to be adopted as the alternative. Actually, the Co-Sleeper can also represent the essential characteristics (sleeper passing frequency and P2 resonance) of the track flexibility compared to the flexible track mounted on the ground, which has been discussed in Section 7.4 (Comparison of tracks). As the OOR prediction using Co-Sleepers has already been discussed in Chapter 3, no more simulation is presented in this chapter.

7.6 Summary

This chapter reports on an investigation of the influence of track flexibility on railway wheel polygonization. After introducing the methods for modelling flexible track in Simpack, the vehicle/flexible track MBS model was built based on the Simpack FTR method. Afterwards, a comparison is conducted between three types of flexible track with different complexity. Finally, the simulation was carried out to investigate the influence of the track flexibility on polygonal wear of wheels. It turns out that the sleeper passing frequency and the P2 frequency are the two dominant frequencies coming from the track flexibility. The local rail bending modes are not found to be able to influence the wheel OOR significantly. Although the sleeper passing frequency is the most dominant frequency coming from the flexible track, it will not produce visible development of wheel OOR. However, the P2 resonance is an important factor contributing to the development of wheel OOR.

However, the modelling of the track flexibility is a complicated issue on itself, as well as its verification. It seems that the results can depend on the modelling method directly. It is believed that an accurate modelling method for the flexible track is the key to understand the influence of track flexibility on the railway wheel polygonization. Little research has been done on this topic. The conclusion obtained in this chapter is only preliminary. To obtain robust conclusions, the simulation model of the flexible track has to match reality. Especially whether the local rail bending modes can be excited effectively is a controversial issue. If more evidence can be obtained, this innovative perspective could be valuable.

Chapter 8 Conclusions and future work

8.1 Conclusions

Railway wheel polygonization has been a severe issue worldwide for decades. However, there has not been a universal explanation that can cover all circumstances, possibly because the railway wheel polygonization is a multi-factor problem, and for different scenarios (e.g. vehicle type, track type, speed range) the wheel polygonization may be attributed to different combination of those potential factors, which makes the problem hard to explain. To improve the understanding of railway wheel polygonization, fundamental research was carried out in several aspects. Some meaningful conclusions are summarized as follows:

- (1) The phase between the instantaneous wear and the excitation was found to be the key indicator determining the OOR evolution direction (to grow or to diminish). The evolution tendency curve obtained from the instantaneous wear FRF was proposed as a useful tool to predict the OOR evolution, especially for predicting the OOR order that would grow dominantly at a given speed. If one or more structural modes can dominate the evolution tendency curve, and the energy distribution of track excitation allows the structural mode(s) to be excited effectively, corresponding OOR orders can develop dominantly.
- (2) The general conditions for wheel OOR to evolve are:
 - The wheel is running at a constant speed for a long time to provide a stable environment for wheel OOR to develop gradually.
 - One or more structural modes can be significantly excited leading to a persisting vibration with fixed frequency to the wheel/rail interface for a long time.
 - The energy distribution of the track excitation allows some structural mode(s) to be excited dominantly.
 - The OOR order that would grow the most dominantly at a given speed can be identified by the evolution tendency curve obtained from the instantaneous wear FRF.
- (3) Four representative wear models, developed by BRR, KTH, USFD, and Professor Zobory, were found to present similar ability to reflect the fluctuation of the instantaneous wear under various circumstances. There is a perfect consistency of trend for all local wear models to simulate the evolved polygonal wear. However, the global method is not suitable for simulating the polygonal wear of railway wheels as some unjustifiable sharp points might be generated by the absolute operation for the global WI (Wear Index). As all the wear models in the comparison share the same converted expression, the selection from among these wear models does not matter significantly, but the wear coefficient adopted is the key to obtain a meaningful result that can match the reality.
- (4) It was found that the wheel OOR does not influence the curve negotiation significantly, but can always exacerbate wheel-rail forces, causing harmful periodic vibration to the vehicle components and the track,

by which the maintenance period must be reduced significantly (potentially by more than half). Bigger wheel radius run-out will always produce more severe vibration. However, for the OOR order, those corresponding to the resonant frequencies of the vehicle/track dynamic system are the most dangerous ones. Typically, the OOR order corresponding to the P2 frequency at a given speed is always the most influential one affecting the vehicle-track dynamic system.

- (5) The wheelset flexibility cannot dominate the railway wheel polygonization in a general sense, unless some prerequisites are fulfilled to provide a suitable environment for the wheelset flexibility to be effectively and continually excited, so as to in turn fluctuate the contact responses, and thereby initiate wheel polygonization. The wheelset flexibility tends to attenuate the normal force slightly, but can always increase the lateral creepage significantly. When the contact adhesion is nearly saturated, which can happen on track with small curve radii or due to large traction torque, the stick-slip vibration occurring at the contact patch can effectively excite the wheelset torsional mode to fluctuate the contact parameters and therefore the wheel wear. If this situation persists for a long time, the development of the wheel polygonization can be expected. The excited order will be exactly determined by the wheelset torsional modal frequency and vehicle speed.
- (6) The sleeper passing frequency and the P2 frequency were found to be the two dominant frequencies coming from the track flexibility. Although the sleeper passing frequency is the most dominant frequency coming from the flexible track, it will not produce visible development of wheel OOR. The P2 resonance is an important factor contributing to the development of wheel OOR. The local rail bending modes are not found to influence the wheel OOR based on the Simpack FTR method.

8.2 Main contributions of this dissertation

- (1) A common workflow for prediction of railway wheel polygonization was developed. Based on this workflow, some fundamental rules for the evolution of polygonal wear were proposed providing innovative perspectives to understand the initiation mechanism of wheel OOR. The general conditions for railway wheel polygonal wear to evolve were then established.
- (2) For the first time, the 'evolution tendency curve' obtained from the instantaneous wear FRF was proposed as a useful tool to predict the wheel OOR evolution, especially for predicting the OOR order that would grow dominantly at a given speed. This innovative perspective emphasized the importance of the phase between the instantaneous wear and the excitation, which is the key factor determining the OOR evolution direction (to grow or to diminish).
- (3) An improved understanding was obtained regarding the applicability of existing popular wear models for simulation of railway wheel polygonization. This work revealed that four widely used wear models developed by BRR, KTH, USFD, and Professor Zobory respectively, present the same nature for prediction of railway wheel polygonization, which is verified by a uniform expression analytically derived for all wear

models. Additionally, it was found that only the local wear model is suitable for simulating the polygonal wear of wheels, but not the global wear model.

8.3 Future work

Compared to the wheel transverse wear prediction that has been used successfully in commercial applications, the prediction of wheel circumferential wear (wheel OOR) is to date far less mature. The railway wheel polygonization is related to not only the material wear itself but also the complicated interaction between the vehicle and the track. Multiple factors can contribute to the initiation of wheel OOR, which makes this problem difficult to interpret. Despite these challenges, based on the work achieved in this dissertation, some future work are recommended below.

- (1) The instantaneous wear FRF is crucial for identifying the potential OOR orders that would develop dominantly. Especially the phase spectrum of the instantaneous wear FRF is the key to judging the 'growing orders' and 'diminishing orders'. However, the phase between the instantaneous wear and excitation is rather hard to interpret. There are two phase-relationships: one is the phase between the excitation and the contact responses, the other is the phase between the contact responses and the instantaneous wear. Both of them present as a complicated issue, which has to be related to the modelling method. It seems that different modelling methods will directly lead to different results, which implies that at least some models may not be sufficiently realistic to predict the OOR evolution faithfully. However, this does not detract from the fundamental observations made in this dissertation. If the modelling method in terms of the two phase-relationships can be improved to match the reality, the evolution tendency curve obtained from the instantaneous wear FRF could be more robust as guidance.
- (2) All the current wear models in wheel/rail application were originally developed for assessing the wheel wear in cross-section. The original wear coefficient is meaningful to calculate the averaged wear after a long-distance of running. However, for the issue of wheel OOR, only the fluctuation of the instantaneous wear is of interest, not the averaged wear. Whether the original wear coefficient, which is suitable for assessing the averaged wear, is still applicable to assess the fluctuation of wear is a question yet to be addressed. A new wear model might have to be developed for predicting wheel OOR. The equation of this new model could be very different from the existing ones, as well as the wear coefficients. Of course, this has to be validated through site measurement or laboratory test.
- (3) In this dissertation, the nominal wheel radius is assumed not to change. However, as the wheel radius is an important factor that can determine the number of OOR orders, the gradual decrease of the wheel radius should be considered in the future. If so, the mean value of the instantaneous wear depth should be considered, as it will determine the reduction speed of the wheel radius. In addition, the wheel transverse profile is also assumed not to change. Although this limitation could be broken through with the more complex program, it is believed that the change of transverse profile might have less importance on the wheel polygonization, but of course, it should be confirmed in the future.
- (4) When comparing the vehicle

vibration between simulation and experiment in the presence of wheel OOR, the discrepancy can be huge for the vehicle components that are far from the wheel-rail interface, e.g. the driver cab. The flexibility of the carbody and the bogie frame, as well as the frequency-dependent characteristic of the suspension spring, may have to be included to obtain more accurate simulation results that can match the reality. With a more accurate MBS model, the parametric analysis of the effect of wheel OOR could be more convincing.

- (5) There is no existing standard judging when the wheel should be re-profiled in the presence of OOR. The practical solution is depending on the vibration level of vehicle components (e.g. axle box). As the OOR order and the radius run-out can both determine the vibration level, a more rational strategy could be established by taking both of them into consideration comprehensively. Nevertheless, this could still be scenario-dependent.
- (6) The modelling of the track flexibility is a complicated issue in itself, as well as its verification. It seems that the results can depend on the modelling method directly. It is believed that an accurate modelling method of the flexible track is the key to understand the influence of track flexibility on the railway wheel polygonization. Little research has been done on this topic. To obtain robust conclusions, the simulation model of the flexible track has to reflect the reality. Especially, whether the local rail bending modes can be excited effectively is a controversial issue. If more evidence can be obtained, this innovative perspective could be valuable.
- (7) It was reported that the wheel tread hardness is an important factor affecting the formation and development of wheel polygonization, especially if the hardness is unevenly distributed around the wheel circumference [60]. Attention should be paid to the wheel hardness in the prediction program for wheel OOR development.

References

- [1] Kalousek J, Johnson KL. An Investigation of Short Pitch Wheel and Rail Corrugations on the Vancouver Mass Transit System. *Proceedings of the Institution of Mechanical Engineers, Part F: Journal of Rail and Rapid Transit*. 1992 July 1, 1992;206(2):127-135.
- [2] Kaper HP. Wheel corrugation on Netherlands railways (NS): Origin and effects of “polygonization” in particular. *Journal of Sound and Vibration*. 1988 1988/01/22/;120(2):267-274.
- [3] Morys B. Enlargement of out-of-round wheel profiles on high speed trains. *Journal of Sound and Vibration*. 1999 1999/11/11;227(5):965-978.
- [4] Johansson A, Nielsen JCO. Out-of-round railway wheels - Wheel-rail contact forces and track response derived from field tests and numerical simulations. *Proceedings of the Institution of Mechanical Engineers, Part F: Journal of Rail and Rapid Transit*. 2003;217(2):135-145.
- [5] Jin X, Wu L, Fang J, et al. An investigation into the mechanism of the polygonal wear of metro train wheels and its effect on the dynamic behaviour of a wheel/rail system. *Vehicle System Dynamics*. 2012;50(12):1817-1834.
- [6] Tao G, Wang L, Wen Z, et al. Measurement and assessment of out-of-round electric locomotive wheels. *Proceedings of the Institution of Mechanical Engineers, Part F: Journal of Rail and Rapid Transit*. 2016.
- [7] Wu Y, Du X, Zhang H-j, et al. Experimental analysis of the mechanism of high-order polygonal wear of wheels of a high-speed train. *Journal of Zhejiang University-SCIENCE A*. 2017 August 01;18(8):579-592.
- [8] Langemann D. Numerical analysis of the polygonalization of railway wheels. *ZAMM - Journal of Applied Mathematics and Mechanics / Zeitschrift für Angewandte Mathematik und Mechanik*. 2001;81(S3):619-620.
- [9] Meywerk M. Polygonalization of railway wheels. *Archive of Applied Mechanics*. 1999;69(2):105-120.
- [10] Meinke P, Meinke S. Polygonalization of wheel treads caused by static and dynamic imbalances. *Journal of Sound and Vibration*. 1999 1999/11/11;227(5):979-986.
- [11] Morys B KHB. Simulation analysis and active compensation of the out-of-round phenomena at wheels of high speed trains. *Proceedings of World Congress on Railway Research; November 16-19; Florence, Italy 1997*. p. 95-105.
- [12] Brommundt E. A simple mechanism for the polygonalization of railway wheels by wear. *Mechanics Research Communications*. 1997;24(4):435-442.
- [13] Johansson A. Out-of-round railway wheels—assessment of wheel tread irregularities in train traffic. *Journal of Sound and Vibration*. 2006 2006/06/13/;293(3):795-806.
- [14] Johansson A, Andersson C. Out-of-round railway wheels—a study of wheel polygonalization through simulation of three-dimensional wheel-rail interaction and wear. *Vehicle System Dynamics*. 2005;43(8):539-559.
- [15] Company CZEL. Report of the wheel polygonalization analysis for HX locomotives. 2017.
- [16] Barke DW, Chiu WK. A Review of the Effects of Out-Of-Round Wheels on Track and Vehicle Components. *Proceedings of the Institution of Mechanical Engineers, Part F: Journal of Rail and Rapid Transit*. 2005;219(3):151-175.
- [17] Wu X, Rakheja S, Qu S, et al. Dynamic responses of a high-speed railway car due to wheel polygonalisation. *Vehicle System Dynamics*. 2018;56(12):1817-1837.
- [18] Nielsen JCO, Johansson A. Out-of-round railway wheels—a literature survey. *Proceedings of the Institution of Mechanical Engineers, Part F: Journal of Rail and Rapid Transit*. 2000;214(2):79-91.
- [19] Lewis R, Olofsson U. *Wheel-rail interface handbook*. CRC; 2009.
- [20] Enblom R. *On Simulation of Uniform Wear and Profile Evolution in the Wheel-Rail Contact [PhD thesis]: Royal Institute of Technology (KTH); 2006*.
- [21] Nielsen JCO, Lundn R, Johansson A, et al. Train-Track Interaction and Mechanisms of Irregular Wear on Wheel and Rail Surfaces. *Vehicle System Dynamics*. 2003;40(1-3):3-54.
- [22] Tao G. *Investigation into the formation mechanism of the polygonal wear of HXD electric locomotive wheels [PhD thesis]: Southwest Jiaotong University; 2018*.
- [23] Bayer RG. *Wear analysis for engineers*. New York: HNB Pub; 2002. (Book, Whole).
- [24] Lewis R, Dwyer-Joyce RS. Wear mechanisms and transitions in railway wheel steels. *Proceedings of the Institution of Mechanical Engineers, Part J: Journal of Engineering Tribology*. 2004;218(6):467-478.
- [25] Bolton P, Clayton P. Rolling—sliding wear damage in rail and tyre steels. *Wear*. 1984;93(2):145-165.
- [26] Rode W, Muller D, Villman J, editors. Results of DB AG Investigations “Out-of-Round Wheels”. *Proceedings of Corrugation Symposium-Extended Abstracts, IFV Bahntechnik, Technische University at Berlin, Germany; 1997*.
- [27] Cui D, An B, Allen P, et al. Effect of the turning characteristics of underfloor wheel lathes on the

- evolution of wheel polygonisation. *Proceedings of the Institution of Mechanical Engineers, Part F: Journal of Rail and Rapid Transit*. 2019;233(5):479-488.
- [28] Wei L, Zong L, Luo S, et al. Research into the problem of wear creating a polygon-shaped wheel on metro trains. *Proceedings of the Institution of Mechanical Engineers, Part F: Journal of Rail and Rapid Transit*. 2016;230(1):43-55.
- [29] Tao G, Wang L, Wen Z, et al. Experimental investigation into the mechanism of the polygonal wear of electric locomotive wheels. *Vehicle System Dynamics*. 2017;56(6):883-899.
- [30] Tao G, Wang L, Wen Z, et al. Measurement and assessment of out-of-round electric locomotive wheels. *Proceedings of the Institution of Mechanical Engineers, Part F: Journal of Rail and Rapid Transit*. 2016;232(1):275-287.
- [31] Fröhling R, Spangenberg U, Reitmann E. Root cause analysis of locomotive wheel tread polygonisation. *Wear*. 2019 2019/08/15;432-433:102911.
- [32] Tao G, Wen Z, Liang X, et al. An investigation into the mechanism of the out-of-round wheels of metro train and its mitigation measures. *Vehicle System Dynamics*. 2018;57(1):1-16.
- [33] Cai W, Chi M, Tao G, et al. Experimental and Numerical Investigation into Formation of Metro Wheel Polygonalization. *Shock and Vibration*. 2019;2019.
- [34] Dadi L. Mechanism study of wheel polygonization based on modal analysis of rail: Southwest Jiaotong University; 2017.
- [35] Wu X, Rakheja S, Cai W, et al. A study of formation of high order wheel polygonalization. *Wear*. 2019;424:1-14.
- [36] Guangxiong C, Xiaolu C, Ke W. Generation Mechanism for Polygonalization of Wheel Treads of High-Speed Trains. *Journal of Southwest Jiaotong University*. 2016;51(2-3):244-250.
- [37] Zhao X, Chen G, Lv J, et al. Study on the mechanism for the wheel polygonal wear of high-speed trains in terms of the frictional self-excited vibration theory. *Wear*. 2019;426:1820-1827.
- [38] Ziqiang X, Shihui L, Xiaoqing D, et al. Study on longitudinal vibration of wheel/rail contact and its implications for wheel polygonization. *Journal of Advances in Vehicle Engineering*. 2017;3(1).
- [39] Dings PC, Dittrich MG. Roughness on dutch railway wheels and rails. *Journal of Sound and Vibration*. 1996 1996/05/30;193(1):103-112.
- [40] Morys B, editor Investigation on vibration in ICE-wheelsets caused by unbalanced masses at high speeds. *Proceedings of 1st ADAMS/Rail Users' Meeting*. Utrecht:[sn]; 1996.
- [41] Ye Y, Shi D, Krause P, et al. Wheel flat can cause or exacerbate wheel polygonization. *Vehicle System Dynamics*. 2019:1-30.
- [42] Fermér M, Nielsen JCO. Vertical Interaction between Train and Track with Soft and Stiff Railpads—Full-Scale Experiments and Theory. *Proceedings of the Institution of Mechanical Engineers, Part F: Journal of Rail and Rapid Transit*. 1995 January 1, 1995;209(1):39-47.
- [43] Ma W, Song R, Luo S. Study on the mechanism of the formation of polygon-shaped wheels on subway vehicles. *Proceedings of the Institution of Mechanical Engineers, Part F: Journal of Rail and Rapid Transit*. 2016;230(1):129-137.
- [44] Dianmai Z, Jiyou Y, Bin X. Analysis of EMU wheel polygonization mechanism. *China Metros*. 2017;20(2):25-27.
- [45] Pan R, Zhao X, Liu P, et al. Micro-mechanism of polygonization wear on railroad wheels. *Wear*. 2017 2017/12/15;392-393(Supplement C):213-220.
- [46] Wu X, Rakheja S, Wu H, et al. A study of polygonal wheel wear through a field test programme. *Vehicle System Dynamics*. 2019;57(6):914-934.
- [47] Shi H, Wang J, Wu P, et al. Field measurements of the evolution of wheel wear and vehicle dynamics for high-speed trains. *Vehicle System Dynamics*. 2018;56(8):1187-1206.
- [48] Simpack help documentation. 2019.
- [49] Xiao Q, Luo Z, Xu X, et al. Research on influence of harmonic wear wheel on wheel/rail contact geometry of high-speed train. *Journal of Mechanical Science and Technology*. 2019;33(2):537-544.
- [50] Wu H, Wu P, Li F, et al. Fatigue analysis of the gearbox housing in high-speed trains under wheel polygonization using a multibody dynamics algorithm. *Engineering Failure Analysis*. 2019;100:351-364.
- [51] Wang Z, Cheng Y, Mei G, et al. Torsional vibration analysis of the gear transmission system of high-speed trains with wheel defects. *Proceedings of the Institution of Mechanical Engineers, Part F: Journal of Rail and Rapid Transit*. 2019:0954409719833791.
- [52] Wang Z, Allen P, Mei G, et al. Influence of wheel-polygonal wear on the dynamic forces within the axle-box bearing of a high-speed train. *Vehicle System Dynamics*. 2019:1-22.
- [53] Wang Z, Mei G, Zhang W, et al. Effects of polygonal wear of wheels on the dynamic performance of the gearbox housing of a high-speed train. *Proceedings of the Institution of Mechanical Engineers, Part F: Journal of Rail and Rapid Transit*. 2018;232(6):1852-1863.
- [54] Lan Q, Dhanasekar M, Handoko YA. Wear damage of out-of-round wheels in rail wagons under braking.

- Engineering Failure Analysis. 2019;102:170-186.
- [55] Chen M, Sun Y, Guo Y, et al. Study on effect of wheel polygonal wear on high-speed vehicle-track-subgrade vertical interactions. *Wear*. 2019 2019/08/15/;432-433:102914.
- [56] Wu X, Chi M, Wu P. Influence of polygonal wear of railway wheels on the wheel set axle stress. *Vehicle System Dynamics*. 2015 2015/11/02;53(11):1535-1554.
- [57] Liu X, Zhai W. Analysis of vertical dynamic wheel/rail interaction caused by polygonal wheels on high-speed trains. *Wear*. 2014;314(1-2):282-290.
- [58] Zhang J, Han G-x, Xiao X-b, et al. Influence of wheel polygonal wear on interior noise of high-speed trains. *Journal of Zhejiang University SCIENCE A*. 2014;15(12):1002-1018.
- [59] LI W, LI Y, Zhang X. Mechanism of the polygonal wear of metro train wheels. *Journal of Mechanical Engineering*. 2013;49(18):17-22.
- [60] Shen W, Song C, Li G, et al. Research for high-speed EMU wheel hardness and polygon-form relationships with solutions. *Railway Locomotive & Car*. 2018;38(4):18-23.
- [61] Spangenberg U. Variable frequency drive harmonics and interharmonics exciting axle torsional vibration resulting in railway wheel polygonisation. *Vehicle System Dynamics*. 2019:1-21.
- [62] Fu B, Bruni S, Luo S. Numerical simulation for polygonal wear of railway wheels. 11th international conference on contact mechanics and wear of rail/wheel systems (CM2018); Delft, The Netherlands 2018.
- [63] Archard JF. Contact and Rubbing of Flat Surfaces. *Journal of Applied Physics*. 1953;24(8):981.
- [64] TB/T449-2016. TB/T449-2016. Wheel profile for locomotive and car. Chinese state railway administration.
- [65] GB2585-2007. GB2585-2007. Hot-rolled steel rails for railway. Chinese standardization administration.
- [66] Liu X, Zhai W. Analysis of vertical dynamic wheel/rail interaction caused by polygonal wheels on high-speed trains. *Wear*. 2014 2014/06/15/;314(1):282-290.
- [67] Garg VK, Dukkipati RV. *Dynamics of railway vehicle systems*. Toronto, Ont: Academic Press; 1984.
- [68] Peng B, Iwnicki S, Shackleton P, et al. The influence of wheelset flexibility on polygonal wear of locomotive wheels. *Wear*. 2019;432-433:102917.
- [69] Peng B, Iwnicki S, Shackleton P, et al. A practical method for simulating the evolution of railway wheel polygonalization. 25th international symposium on dynamics of vehicles on roads and tracks; Rockhampton, Australia 2017. p. 753-758.
- [70] Pearce TG, Sherratt ND. Prediction of wheel profile wear. *Wear*. 1991 1991/04/20;144(1):343-351.
- [71] Zobory I. Prediction of Wheel/Rail Profile Wear. *Vehicle System Dynamics*. 1997;28(2):221-259.
- [72] Neilsen J. Evolution of rail corrugation predicted with a non-linear wear model. *Journal of Sound and Vibration*. 1999;227(5):915-933.
- [73] Jendel T, Berg M. Prediction of Wheel Profile Wear. *Vehicle System Dynamics*. 2002;37(sup1):502-513.
- [74] Vuong TT, Meehan PA, Eadie DT, et al. Investigation of a transitional wear model for wear and wear-type rail corrugation prediction. *Wear*. 2011 2011/05/18/;271(1):287-298.
- [75] De Arizon J, Verlinden O, Dehombreux P. Prediction of wheel wear in urban railway transport: comparison of existing models. *Vehicle System Dynamics*. 2007;45(9):849-874.
- [76] Enblom R, Berg M. Simulation of railway wheel profile development due to wear—influence of disc braking and contact environment. *Wear*. 2005 2005/03/01/;258(7):1055-1063.
- [77] Pombo J, Ambrósio J, Pereira M, et al. Development of a wear prediction tool for steel railway wheels using three alternative wear functions. *Wear*. 2011;271(1):238-245.
- [78] Ding J, Li F, Huang Y. Analysis of the wheel wear model based on the creep mechanism. *Zhongguo Tiedao Kexue*. 2010;31(5):66-72.
- [79] Braghin F, Lewis R, Dwyer-Joyce RS, et al. A mathematical model to predict railway wheel profile evolution due to wear. *Wear*. 2006;261(11):1253-1264.
- [80] Johansson A. *Out-of-Round Railway Wheels - Causes and Consequences [PhD thesis]*. Gothenberg, Sweden: Chalmers University of Technology; 2005.
- [81] Kalker JJ. A Fast Algorithm for the Simplified Theory of Rolling Contact. *Vehicle System Dynamics*. 1982 1982/02/01;11(1):1-13.
- [82] Tao G, Du X, Zhang H, et al. Development and validation of a model for predicting wheel wear in high-speed trains. *Journal of Zhejiang University-SCIENCE A*. 2017 August 01;18(8):603-616.
- [83] Ding J, Li F, Huang Y, et al. Application of the semi-Hertzian method to the prediction of wheel wear in heavy haul freight car. *Wear*. 2014 2014/06/15/;314(1):104-110.
- [84] Enblom R, Stichel S, Skolan för t, et al. Industrial implementation of novel procedures for the prediction of railway wheel surface deterioration. *Wear*. 2011;271(1):203-209.
- [85] Olofsson U, Telliskivi T. Wear, plastic deformation and friction of two rail steels—a full-scale test and a laboratory study. *Wear*. 2003 2003/01/01/;254(1):80-93.
- [86] Jendel T. Prediction of wheel profile wear—comparisons with field measurements. *Wear*. 2002;253(1–

- 2):89-99.
- [87] Bevan A, Allen P, editors. Application of a wear prediction method to the analysis of a new UK wheel profile. Proceedings of the 7th Contact Mechanics and Wear of Rail/Wheel Systems Conference; 2006; Brisbane, Australia.
- [88] EN15610:2019. Railway applications - Acoustics - Rail and wheel roughness measurement related to noise generation. European committee for standardization.
- [89] BS EN ISO 3095:2013: Acoustics. Railway applications. Measurement of noise emitted by railbound vehicles. British Standards Institute; 2013.
- [90] BS EN ISO 15313:2010: Rail application. In-service wheelset operation requirements. In-service and off-vehicle wheelset maintenance. British Standards Institute; 2013.
- [91] Institute of rail vehicles SJU. XX electric locomotive dynamic analysis report. 2007.
- [92] UIC 518-2009. Testing and approval of railway vehicles from the point of view of their dynamic behaviour-Safety-Track fatigue-Running behaviour. International Union of Railways.
- [93] BS EN 14363:2016: Railway applications. Testing and Simulation for the acceptance of running characteristics of railway vehicles. Running Behaviour and stationary tests. British Standards Institute; 2016.
- [94] Iwnicki S. Simulation of wheel-rail contact forces. *Fatigue & fracture of engineering materials & structures*. 2003;26(10):887-900.
- [95] Robert Fröhling US, Eduard Reitmann. Locomotive wheel tread polygonisation caused by torsional axle shaft vibration. 11th international conference on contact mechanics and wear of rail/wheel systems (CM2018); 2018; Delft, the Netherlands 2018. p. 261-270.
- [96] Popp K, Kaiser I, Kruse H. System dynamics of railway vehicles and track [journal article]. *Archive of Applied Mechanics*. 2003 June 01;72(11):949-961.
- [97] Popp K, Kruse H, Kaiser I. Vehicle-Track Dynamics in the Mid-Frequency Range. *Vehicle System Dynamics*. 1999 1999/06/01;31(5-6):423-464.
- [98] Fermer M, Nielsen JCO. Wheel/Rail Contact Forces for Flexible versus Solid Wheels due to Tread Irregularities. *Vehicle System Dynamics*. 1994 1994/01/01;23(sup1):142-157.
- [99] Chaar N, Berg M, Skolan för t, et al. Vehicle-Track Dynamic Simulations of a Locomotive Considering Wheelset Structural Flexibility and Comparison with Measurements. Proceedings of the Institution of Mechanical Engineers, Part F: Journal of Rail and Rapid Transit. 2005;219(4):225-238.
- [100] Guiral A, Alonso A, Giménez JG. Vehicle - track interaction at high frequencies – Modelling of a flexible rotating wheelset in non-inertial reference frames. *Journal of Sound and Vibration*. 2015 2015/10/27;355:284-304.
- [101] Baeza L, Fayos J, Roda A, et al. High frequency railway vehicle-track dynamics through flexible rotating wheelsets. *Vehicle System Dynamics*. 2008;46(7):647-659.
- [102] Torstensson PT, Nielsen JCO, Baeza L, et al. Dynamic train-track interaction at high vehicle speeds—Modelling of wheelset dynamics and wheel rotation. *Journal of Sound and Vibration*. 2011;330(22):5309-5321.
- [103] Craig R, R, Bampton M, C C. Coupling of Substructures for Dynamic Analyses. *AIAA Journal*. 1968 1968;6(7):1313-1319.
- [104] Zhai W. *Vehicle-Track Coupling Dynamics*. Beijing China: Science Press; 2007.
- [105] Aceituno JF, Wang P, Wang L, et al. Influence of rail flexibility in a wheel/rail wear prediction model. Proceedings of the Institution of Mechanical Engineers, Part F: Journal of Rail and Rapid Transit. 2017;231(1):57-74.
- [106] Baeza L, Vila P, Xie G, et al. Prediction of rail corrugation using a rotating flexible wheelset coupled with a flexible track model and a non-Hertzian/non-steady contact model. *Journal of Sound and Vibration*. 2011 2011/08/29;330(18):4493-4507.
- [107] Ling L, Xiao X-b, Xiong J-y, et al. A 3D model for coupling dynamics analysis of high-speed train/track system. *Journal of Zhejiang University SCIENCE A*. 2014 December 01;15(12):964-983.
- [108] Gonzalez FJ, Suarez B, Paulin J, et al. Safety assessment of underground vehicles passing over highly resilient straight track in the presence of a broken rail. Proceedings of the Institution of Mechanical Engineers, Part F: Journal of Rail and Rapid Transit. 2008;222(1):69-84.
- [109] Blanco-Lorenzo J, Santamaria J, Vadillo EG, et al. Dynamic comparison of different types of slab track and ballasted track using a flexible track model. Proceedings of the Institution of Mechanical Engineers, Part F: Journal of Rail and Rapid Transit. 2011;225(6):574-592.
- [110] Ji Z, Yang G, Liu Y, et al. Analysis of vertical vibration characteristics of the vehicle-flexible track coupling system under wind load and track irregularity. Proceedings of the Institution of Mechanical Engineers, Part F: Journal of Rail and Rapid Transit. 2018;232(10):2444-2455.